RECONFIGURABLE SILICON PHOTONIC DEVICES FOR OPTICAL SIGNAL PROCESSING

A Dissertation
Presented to
The Academic Faculty

by

Amir H. Atabaki

In Partial Fulfillment
of the Requirements for the Degree
Doctor of Philosophy in
Electrical Engineering

School of Electrical and Computer Engineering
Georgia Institute of Technology
August 2011

RECONFIGURABLE SILICON PHOTONIC DEVICES FOR OPTICAL SIGNAL PROCESSING

Approved by:

Professor Ali Adibi, Advisor
School of Electrical and Computer Engineering
Georgia Institute of Technology

Professor Stephen Ralph
School of Electrical and Computer Engineering
Georgia Institute of Technology

Professor John A. Buck
School of Electrical and Computer Engineering
Georgia Institute of Technology

Professor David Anderson
School of Electrical and Computer Engineering
Georgia Institute of Technology

Professor Rick Trebibno
School of Physics
Georgia Institute of Technology

Date Approved: August 2011

To my Parents,

Maryam and Hossein.

ACKNOWLEDGEMENTS

First and foremost, I would like to thank my advisor, Professor Ali Adibi, for his guidance and endless support throughout my time at Georgia Tech. I could not appreciate more the confidence he had in me choosing my own research topic and allowing me to work in a relaxed environment. It was one of the greatest opportunities of my life to work with him and to learn a great deal from his experience and expertise. I appreciate that he always managed to dedicate some of his time to our discussions despite his very busy schedule.

The friendly, pleasant and scientific nature of Photonic Research Group made it a truly ideal working place for me. I had the privilege to work with outstanding and at the same time humble experts in photonics in this group. When I first joined this group, I really did not have much vision and experience in many areas of photonics. I truly gained a lot of insight through profound discussions and collaborations with my fellow friend at this group. In particular, I would like to acknowledge Dr. Babak Momeni, Dr. Mohammad Soltani, and Dr. Ehsan Shah Hosseini for mentoring me in different areas in my research. I owe a great deal of the achievements in my research to the fruitful discussions with these gentlemen. Specially Ehsan for teaching me micro-fabrication and for all of his supports both as a lab-mate and roommate. I was also lucky to work with Dr. Siva Yegnanarayanan and Reza Eftekhar for helping me to gain insight in the field of silicon photonics and guiding me in the research projects that finally resulted in my Ph.D. dissertation. Also, special thanks to Payam Alipour and Qing Li for all their help and great discussions. I had the privilege to work with them on a DARPA project where our teamwork resulted in many research achievements. I would also like to thank Maysam Chamanzar, Dr. Arash Karbaschi, Dr. Omid Momtahan, Dr. Saman Jafarpour, Dr. Saeed Mohammadi, Dr. Murtaza Askari, Farshid Ghasemi, Reza Pourabolghasem, Zhixuan Xia, Hossein Taheri, and Majid Sodagar for their friendship and support in the past six years.

I would like to acknowledge the staff of Microelectronics Research Center (MiRC) for

their dedication in keeping this place to run smoothly. In particular, I want to acknowledge Gary Spinner, Devin Brown, Viny Nguyen, and Eric Woods. Without their help in dire situations, I would have missed some of the very important conference and report deadlines.

Outside of workplace, I was lucky to build friendships that will remain with me forever. I want to express my warmest gratitude to Navid Pourshiravi and Ahmad Beirami for their unconditional friendship and help whenever I needed them. I also owe a lot of my memorable moments in Atlanta to Saba Mohammadi and Negar Mohammadi for their support. I truly have had a lot of enjoyable moments with all of my friends, but specifically I would like to thank Seena Ghalambor, Amirali Tavallaee, and Amirali Kani for their kindness and friendship.

Last but not least, I am grateful to my family for their love and support from the very moment I entered their lives. I could not be enjoying my life as much as I do today, if it was not for their support and sacrifices. Moreover, I would like to thank my brother, Amir Saeed, for his support and for all the great moments we have shared together.

TABLE OF CONTENTS

LIST OF TABLES

LIST OF FIGURES

SUMMARY

Optical signal processing is a powerful technique when the bandwidth limitations of electronics is reached. Today's fiber optics systems are empowered by many linear optical signal processing functions such as add-drop multiplexing, filtering, and dispersion compensation, and many nonlinear functions such as wavelength-conversion and signal regeneration. The capabilities of optical signal processing extends beyond fiber optics networks, and many signal processing functionalities such as analog-to-digital conversion and filtering that are conventionally handled using digital electronics, are managed easier in the optical domain at large bandwidths (tens to hundreds of GHz). Silicon has unique advantages as the material of choice for the implementation of photonics devices for optical signal processing applications. Low material cost and inexpensive and reliable manufacturing of silicon are two main advantages of silicon. Also, the high refractive index of silicon allows high-level integration of ultra-compact devices enabling the low-power operation. Reconfigurability is one of the major requirements for photonics devices, both for dynamic tuning of device operation, and for correcting the variations in the device parameters as a result of fabrication inaccuracies.

In this Ph.D. work, a low-power, low-loss, fast, and CMOS-compatible reconfiguration technology in developed for large-scale silicon photonic devices. Prior to this work, only a subset of these properties had been achieved because of the physical and design tradeoffs. The developed reconfiguration method is applied to novel photonic devices for on-chip nonlinear optical signal processing. Moreover, a novel device concept based on coupled-resonators is proposed and demonstrated that lifts many of the practical design challenges of simple traveling-wave resonators for nonlinear optics applications. The highlight of these devices is the possibility of post-fabrication tuning of the resonance frequency of individual resonance modes to maximize the efficiency of the nonlinear process. The performance of these devices are tested through the demonstration of wavelength conversion

through four-wave mixing in silicon-based resonators.

Large-scale integrated silicon photonic circuits require a low-power, low-loss, fast, and CMOS-compatible reconfiguration technology. Thermooptic effect is particularly suitable for this purpose as it is strong in silicon, intrinsically loss-less, and it can be easily implemented using CMOS-compatible processes. However, the major shortcoming of thermal reconfiguration methods is their slow response-time as a result of the slow heat transport through the SiO_2 substrate and over-cladding in the silicon-on-insulator platform. In Chapter 3, material and structural optimizations are carried out on the commonly used metallic microheaters to improve their reconfiguration speed. By appropriate pulse-excitation of these devices, sub-microsecond reconfiguration time is achieved. For the analysis of these devices, heat transport is modeled using finite-element method. Our numerical modeling results are in good agreement with our experimental results, suggesting that our modeling tool is reliable for extensive optimization purposes. We have also developed a system-level model that can describe the response of the microheater with very good accuracy. This model is a powerful tool for system-level studies of the microheater.

The detailed study of the heat transport in the microheater architecture reveals that the small thermal conductivity of the material separating the microheater from the silicon device is the source of slow heat propagation delay. Therefore, using conventional microheater architecture with SiO_2 cladding layer it is not possible to improve thermal reconfiguration time beyond one microsecond using pulsed-excitation. In Chapter 4, a new microheater architecture is proposed in which the microheater is directly fabricated over the silicon layer to utilize its high thermal conductivity for heat conduction. In this design, microheater is placed on the microdisk toward the center, and far from the optical mode. This device is fabricated on an silicon-on-insulator (SOI) wafer and the experimental results showed $\approx$80 ns heat propagation delay. With pulsed-excitation of these microheaters, sub-100-ns reconfiguration of the photonic device is demonstrated. The power consumption of this device with a 4 μm diameter microdisk is measured to be 1 mW per 2.4 nm resonance wavelength shift (or 265 GHz resonance frequency shift).

To the best of our knowledge, this is the fastest thermal reconfiguration speed reported to this date with this level of power consumption and insertion loss. A major challenge of pulsed-excitation scheme is that ultrafast reconfiguration can only be achieved in the heating cycle and not in the cooling cycle. A differential architecture is demonstrated to enable reconfiguration in opposite directions by appropriately heating of the two arms of this device.

The other major focus of this Ph.D. work, is on the design and demonstration of novel resonator-based reconfigurable photonic devices for nonlinear optics applications. Different types of traveling-wave resonators (TWRs) have been widely used for nonlinear optics on silicon platform to reduce the pump power requirement by a few orders of magnitude. However, a major challenge in using these resonators for nonlinear processes is the the lack of a practical method to engineer the resonance frequency of the resonance modes of interest with a good degree of freedom. This design challenge in tackled in this work through a new device concept based on coupled resonators. By controlling the mode splitting of the supermodes of these coupled-resonator structures through thermal tuning, several practical issues with these resonators are addressed. In Chapter 5, a temporal coupled-mode theory is developed for four-wave mixing (FWM) in TWRs to model the performance of the proposed devices for nonlinear optics experiments. Here, a quasi-phase-matching theory in microresonators is developed for the first time that is applicable to complicated coupled-resonator structures.

In Chapter 6, a coupled-resonator device consisting of two resonators that are coupled through a Mach-Zehnder interferometer is proposed and experimentally demonstrated. This device enables the tuning of the resonance-frequency spacing up to one whole free-spectra range. This is achieved by tuning of the mutual coupling of the resonators through the interferometer coupling the two resonators. To the best of our knowledge, this the first integrated device that enables this level of tuning of the resonance frequency spacing. This device is also designed for a FWM experiment and it is shown that the resonance condition for an efficient FWM process can be fine tuned using integrated microheaters over the interferometer.

In Chapter 7, a three-element coupled-resonator device is proposed and demonstrated for FWM in silicon. This device enables the design of the frequency detuning of the signal/idler modes from the pump mode through the mutual coupling of resonators and not their length. This allows us to utilize ultra-small microdisks with very large field enhancement for FWM application for the first time. Wavelength conversion is demonstrated in this device and the experimental results are in good agreement with the theoretical predictions of the developed coupled-mode theory in Chapter 5.

Another design issue in the resonator-based nonlinear optics devices is the different bandwidth requirements of the interacting waves. For instance, in a FWM-assisted wavelength conversion process in DWDM system, signal and idler bandwidths are in the order of a few tens of gigahertz and the pump is usually continuous wave (with a very small bandwidth). Conventional coupling scheme results in identical bandwidth for all the resonance modes, resulting in the loss of field enhancement and therefore the efficiency of the nonlinear process. In Chapter 8, a new interferometric coupling scheme is proposed and demonstrated that enables designing the optimum bandwidth (and coupling) condition for all the interacting waves. Microheaters are incorporated in this device to accurately adjust the coupling condition. To the best of our knowledge, this is the first design addressing this issue in resonator-based nonlinear optics on chip.

CHAPTER I

INTRODUCTION

1.1 Emergence of Silicon Photonics

Transmission of data over optical signals is becoming more imminent because of the fundamental limitations of electrical signals with data rates over 10 Gb/s. This limitation has been the main challenge in long-haul (i.e., hundreds of kilometer) data transmission and the main motivation in the emergence of fiber optics networks. With the increase in the demand for higher data rates, the usage of optical signals is becoming more essential for a wider range of applications such as metro-area networks, board-to-board, and chip-to-chip interconnects. The expected widespread usage of optical signals calls for a reliable and inexpensive technology for the implementation of necessary optical signal processing components such as, modulators, filters, and amplifiers. To this date, these components are usually built individually using different technologies such as, fiber-based, thin-film, and planar integrated circuit technology. As a result, the optical communications systems based on these individual components are usually bulky and expensive.

In the past two decades, there has been a lot of effort in the integration of different optical functionalities to reduce the size and cost of the optical signal processing systems. Integration of optical devices based on a planar lightwave circuit (PLC) platform is a promising approach for this purpose. One great motivation for using planar technology is their compatibility with already mature and available microelectronics fabrication and manufacturing facilities. However, a major challenge in this avenue is material limitations that do not allow the integration of all optical functionalities using a single material. For instance, optical gain and amplification are only available in materials with direct electronic bandgap such as III- V compound materials. However, III-V materials are usually expensive because of the high cost of the material growth. Thus, compromises should be taken into account for different applications.

In the past, different low-index-contrast (LIC) materials such as silicon dioxide (SiO_2) and polymers [1, 2, 3]; and different high-index-contrast (HIC) materials [4, 5, 6] such as Silicon (Si) and III-V compounds have been used for photonic component fabrication. In the early days of integrated photonics, because of the limitations in lithography resolution, most of the fabricated devices were large (tens to hundreds of micron) compared to the wavelength of operation. However, with the advancements in photo-lithography and electron-beam-lithography techniques, more efforts are devoted to the miniaturization of photonic components. Thus, HIC materials with high optical-field confinement potential have gained more attention recently. Soltani *et al.* [7] have shown one of the most compact and low-loss devices in integrated photonics in Si platform with a bending radius of 1.5 μm.

Among HIC material systems, unique technological advantages of Si, the most versatile material in microelectronics industry, has made it the material of choice for most of photonics applications. Low material cost and inexpensive and mature fabrication processes of Si are two main advantages of this material over other HIC materials for reliable and large-scale integration of photonic components. This field that is known as "silicon photonics [1]" has grown rapidly throughout the past few years and its impact in different areas of optics is highly anticipated in near future.

One particular advantage of Si among other HIC materials in the possibility of achieving low-loss devices. Loss in one of the most important parameters in optical devices that directly affect many performance characteristics of a device such as, insertion loss, dynamic range, sensitivity, and field enhancement. Theoretically, high index contrast between the core of the waveguide and its surrounding might cause strong scattering from surface roughnesses on the waveguide core [8]. However, one of the lowest reported propagation losses in integrated optical devices is achieved in Si platform thanks to the high quality dry-etching and post-processing techniques for Si[9, 5].

[1] Photonics is the area in optics dealing with the generation, modulation, signal processing, and detection and sensing of light mainly in the visible and near infrared spectrum of light. What differentiates photonics from optics is that photonics is referred to applications of light, which directly or indirectly depend on the quantum nature of light. For instance, all applications that are based on the light generated by lasers, their signal processing and detection using semiconductor detectors are considered photonics.

All the technological and material advantages of Si have initiated a series of works for the implementation of numerous photonic functionalities in this material. Many passive devices such as, low-loss waveguides [9, 10], high quality-factor (Q) resonators [5, 11], and filters [12], have been implemented is Si. In addition, active devices such as, high-speed modulators with 40 Gb/s data rates [13, 14], high-speed switched [15], high-speed detectors [16, 17]; and many reconfigurable devices such as reconfigurable adddrop multiplexers (ROADMs) [18, 19] have been successfully demonstrated in Si. Also, commercial products such as, variable optical attenuators and active cables, based on Si photonics technology, are now available in the market [20, 21].

1.2 Optical Signal Processing

The high propagation loss of electrical signals and the design challenges and the high cost of high-speed electronics are the two main bottlenecks of electronic signal processing at high frequencies ($\geq$ 10Gb/s). All these challenges have led to converting to optical domain at high frequencies, both for data communication and signal processing applications. Thus, many signal processing applications that are conventionally handled with digital electronics are performed with optical signal processing techniques. These applications can be categorized in two groups: 1) optical signal processing in optical networks and 2) optical signal processing of radio-frequency (RF) signals. The former encompasses a series of functionalities in optical networks such as add-drop multiplexing, filtering, dispersion compensating, and switching. One advantage of all-optical signal processing in optical networks is the transparency of the network to the signal data rate[2]. The latter, which lies under the field of "RF-photonics", is basically the implementation of RF signal processing applications such as, signal correlation and filtering using photonic devices. In this approach, the electrical signal is modulated over an optical carrier and different signal processing functions such as, filtering, correlation, and digital-to-analog conversion (DAC) are preformed using optical components. Finally, the optical signal is converted

[2]Optical networks whose signal processing is performed all-optically are independent of the signal data rate. This is known as the "transparency" of the network to data rate.

to electrical domain using photodetectors. Some of signaling processing functionalities that have been demonstrated in the past (mainly fiber-based) are filtering [12], high-speed digital-to-analog conversion (DAC) [22], and signal correlation [23].

The majority of optical signal processing functionalities are usually in the linear regime. However, certain functions such as wavelength conversion and amplification can only be obtained using nonlinear processes. As the optical nonlinearity is usually much weaker than the electrical nonlinearity, realization of such functions is difficult in the optical domain. However, the third-order nonlinearity of silica fibers and other semiconductors (e.g., Si and GaAs) has been utilized before for demonstrating wavelength conversion and amplification in fiber optics networks [24, 25, 26, 27, 28, 29, 30].

1.3 Reconfiguration of Si Photonic Devices

Most of today's optical signal processing applications in optical networks or RF-photonics require reconfiguration of the photonic components. For instance, in most of optical networks with a wavelength division multiplexing (WDM) scheme, reconfigurable filtering, reconfigurable add-drop multiplexing, switching, and in more advanced systems, reconfigurable wavelength conversion is required. The compact size and low cost of Si photonic devices, make them attractive for the implementation of these reconfigurable functionalities for different optical signal processing applications.

Reconfigurable filtering, switching, and multiplexing encompass a wide range of optical signal processing applications and they have been implemented using different technologies. Reconfigurable optical add-drop multiplexing (ROADM), which is a building block of all optical networks, has been implemented using fiber Bragg gratings (FBG) [31], integrated arrayed-waveguide gratings [32], and microring resonators [18, 19]. Switches have also been demonstrated using different approaches [33, 34, 35, 36, 37, 38]. Dispersion compensators (DCs), which correct for the signal dispersion caused by the propagation of signal over long lengths of fiber, are demonstrated using Si-based devices [39, 40]. Also, variable optical attenuators (VOAs) are demonstrated in Si platform and are commercially available in the market [21].

In addition to the operation of the components mentioned above, reconfiguration is needed to correct for the variations of device parameters as a result of inaccuracies in fabrication processes. It should be noted that one challenge of HIC materials such as Si, is the high sensitivity of the device to dimensional variation. In such devices, dimensional variations in the order of nanometers may considerably change the device operation. Hence, a tuning mechanism is needed to correct for these variations in the fabrication of these devices.

1.3.1 Reconfiguration Mechanisms

In the past, reconfiguration of Si photonic devices have been mainly based on three major physical effects, namely, free-carrier-plasma dispersion [41, 42], electrooptic [43] and thermooptic [44, 18, 19, 39, 40, 33, 34, 35, 36, 37, 38] effects. Si is a semiconductor and therefore its refractive index depends on the the applied electric field (electro-refraction effect) and also the concentration of free-carriers (free-carrier-plasma dispersion effect). Although the electro-recfraction effect in Si is weak ($\Delta n = 1.3 \times 10^{-5}$ for E = 10V/μm), free-carrier-plasma dispersion effect is pretty strong and with 10^{18} carriers/cm^3 a $\Delta n = \pm 1.5 \times 10^{-3}$ is observed [45]. Also, Si has a strong thermooptic effect with a thermoopic coefficient of $\Delta n = 1.8 \times 10^{-4} K^{-1}$ [46]. All these physical phenomena have unique properties and can be exploited for different applications.

Free-carrier-plasma dispersion effect enables a fast reconfiguration speed (typically $\leq$1 ns), and this effect has been widely used for ultrafast modulation [13, 14] and switching [15] applications. However, this fast reconfiguration comes at the cost of an inherent optical loss caused by the injection of free carriers. For many applications especially signal processing, the introduced loss can be problematic to the performance of the device. This effect is also not suited for wideband application as the concentration of free-carriers cannot be easily increased with moderate power levels.

Another method of reconfiguration is through hybrid Si-polymer devices based on electrooptic effect. As mentioned before, the electro-refraction effect in Si is weak and this material cannot be manipulated by directly applying an electric field across the device.

However, by coating Si with a polymer with strong electrooptic effect, its properties can be tuned by applying an electrical field. This method has the advantage of being low-loss and low power with relatively fast response time (typically, in the order of nanoseconds) [43]. However, these devices are technologically challenging as they require large drive voltages, and at the same time, they are not CMOS-compatible.

On the other hand, thermooptic effect in Si is strong ($\Delta n = 1.8 \times 10^{-4} K^{-1}$) and inherently lossless. Moreover, reconfigurable devices based in this effect are usually driven with moderate voltage levels (< 10V) and are CMOS-compatible; and therefore, these devices are very attractive for reconfiguration purposes. Thermally-reconfigurable devices have been use extensively for the implementation of reconfigurable filters [44], reconfigurable add-drop multiplexers (ROADMs) [18, 19], dispersion compensators [39, 40], and switches [33, 34, 35, 36, 37, 38]. Nevertheless, one shortcoming of thermally-reconfigured devices is their slow response time (milliseconds to a few microseconds) as a result of the slow heat diffusion process. Hence, in order to use this technology for ultrafast tuning applications, their reconfiguration speed should be enhanced considerably.

1.4 Conclusion

Low cost and reliable manufacturability of Si along with the possibility of achieving low-loss and ultra-compact components in Si, promises the large-scale integration of photonic functionalities with an unprecedented optical signal processing power. One necessary requirement for these applications is a low loss, high speed, large dynamic range, and CMOS-compatible reconfiguration technology. This reconfigurability enables many signal processing application with an unprecedented level of complexity and scalability.

The main focus of this work is to address two main issues in the field of reconfigurable Si photonics. First, the issue of low-power and ultrafast reconfiguration of Si photonic devices is approach by introducing a novel microheater structure that is directly integrated on the Si layer and enables sub-100-nanosecond reconfiguration. This device offers the most compact, lowest power consumption and fastest thermooptic device demonstrated to this date. Second, the challenges of efficient nonlinear optics experiments in Si are approached

by designing and implementing reconfigurable photonic devices for these applications. A Novel reconfigurable resonator is demonstrated in this work with the possibility of tuning the spacing of its resonant modes. This device can overcome many of the challenges of third-order nonlinear experiments in Si such as phase-matching condition.

Reconfigurable Silicon Photonics for All-Optical Signal Processing

Cost and manufacturability advantages of Si have turned it into the material of choice for optical networks and RF-photonics applications. At the same time, the possibility of the fabrication of low-loss and ultra-compact components in Si promises large-scale integration of photonic functionalities with an unprecedented optical signal processing power. One essential requirement for many signal processing applications is the reconfigurability of the photonic components. Hence, a low-power and fast tuning technology should be developed for Si photonic devices that is compatible with current CMOS fabrication processes and its associated electronics circuitry limitations (mainly, maximum allowed voltage).

With the compactness and low-loss capabilities of Si photonics devices, novel device designed for linear optical signal processing applications can further increase the capabilities of Si photonics. Also, the strong third-order nonlinearity in Si promises efficient nonlinear optical signal processing applications. However, there are several challenges that needs to be addressed to achieve such capabilities

The main focus of this work is to address two main issues in the field of Si photonics. First, the issue of low-power and ultra-fast reconfiguration of Si photonics devices is tackled by introducing a novel microheater structure that is directly integrated on small microdisk phase-shifters with sub-100-nanosecond reconfiguration time. These devices offer the most compact, most power-efficient and fastest thermooptic devices demonstrated to this date. Second, a series of reconfigurable resonator-based devices are proposed and demonstrated for nonlinear optical signal processing applications that lift many of the design challenges of conventional traveling-wave resonators. One of the challenges of resonators in nonlinear optics is that there is not an easy method to tune the frequency spacing of the resonance modes. This capability allows us to fine-tune the resonance

modes to the frequency of the interacting waves to enhance the efficiency of the nonlinear process. In this work, we propose two coupled-resonator structures for four-wave mixing in Si that enable the independent tunability of different resonance modes for efficient field enhancement inside this device. We also propose and demonstrate a new coupling scheme that enables the optimum design of the coupling coefficient (and bandwidth) of individual resonance modes independent of each other. The combination of these device concepts considerably improves the efficiency of nonlinear optics applications in Si.

CHAPTER II

THEORETICAL BACKGROUND

In this chapter, the basics of electromagnetic modal analysis of waveguides and traveling-wave resonators are discussed. Also, temporal coupled-mode theory as a basic tool for the analysis of photonic devices is introduced. Fundamentals of heat transport that are used for the analysis of heat diffusion in thermally-tuned devices are introduced in Section 2.3.

2.1 Electromagnetic Modal Analysis

The main building blocks of the many photonic circuits are waveguides and resonators. The modes of these devices, which are the solutions to the wave propagation equation, are of great importance as the energy propagating in any particular mode of these devices remains in the same mode in the absence of perturbation [1].

The propagation of the electromagnetic wave is governed by the Maxwell's equations. Maxwell's curl equations (i.e., Faraday's and Amper's laws) for waves with harmonic time dependence, $\exp(j\omega t)$, are express as

$$\nabla \times \mathbf{H} = \quad j\omega\epsilon_o\mathbf{E} + j\omega\mathbf{P}, \text{ (Amper's law)} \tag{1}$$

$$\nabla \times \mathbf{E} = -j\omega\mu_o\mathbf{H}, \text{ (Faraday's law)} \tag{2}$$

where μ_o and ϵ_o are the permeability and permittivity of the vacuum, respectively. Also, $\mathbf{E}$, $\mathbf{H}$, and $\mathbf{P}$ represent the electric, magnetic, and polarization fields, respectively. Polarization field inside a linear material can be express by

$$\mathbf{P} = \epsilon_o(n^2 - 1)\mathbf{E}, \tag{3}$$

where n is the refractive index of the material. By combining Eqs. 1, 2, and 3 the following

[1] Perturbation is referred to any change in the device physical properties such that the device symmetry is broken. For instance, any change introduced along the length of a translationally symmetric waveguide is called a perturbation

Helmholtz equations that govern the wave propagation of the magnetic and electric fields are derived:

$$\nabla \times (\frac{1}{n^2}\nabla \times \mathbf{H}) = \left(\frac{\omega}{c}\right)^2 \mathbf{H}, \text{ and} \tag{4}$$

$$\nabla \times \nabla \times \mathbf{E} = \left(\frac{\omega}{c}\right)^2 n^2 \mathbf{E}, \tag{5}$$

where $c = (\epsilon_o \mu_o)^{-\frac{1}{2}}$ is the speed of light in vacuum. Modes of different structures such as, waveguides and resonators can be obtained by solving Eqs. 4 and 5 with appropriate boundary conditions.

2.1.1 Waveguide Mode Analysis

The very basic structure in integrated optics is a waveguide. Conventionally, different types of waveguides have been used in different integrated platforms. Rib and ridge waveguides are the two most common waveguides in Si photonics because of their ease of fabrication, and Figs. 1(a) and 1(b) show the schematic of the lateral cross-section of these waveguides, respectively. These waveguides have translational symmetry in the z direction (normal to the cross-section plane of the waveguides).

Because of the translational symmetry of the structure of the waveguide in the z direction, electromagnetic field can be considered to have a $\exp(-j\beta z)$ dependence, and the fields can be expressed by

$$\mathbf{E} = \tilde{\mathbf{E}}(\mathbf{r}) \exp(-j\beta z) \tag{6}$$

$$\mathbf{H} = \tilde{\mathbf{H}}(\mathbf{r}) \exp(-j\beta z). \tag{7}$$

where β is the propagation constant of the mode in the z direction and $\mathbf{r}$ is the position vector in the xy plane. By substituting the Eq. 7 into Eq. 4, the wave propagation equation for the waveguide is obtained. As there is not a general theoretical solution to this wave equation problem [47], we rely on numerical modeling using finite-element method (FEM). For this purpose, we use the "RF module" of COMSOL software package. Figure 2 shows an examples of a finite-element mesh of a typical ridge waveguide with a height of 230 nm and width of 450 nm. Figures 3(a) and 3(b) show the profile of the Poynting vector in the

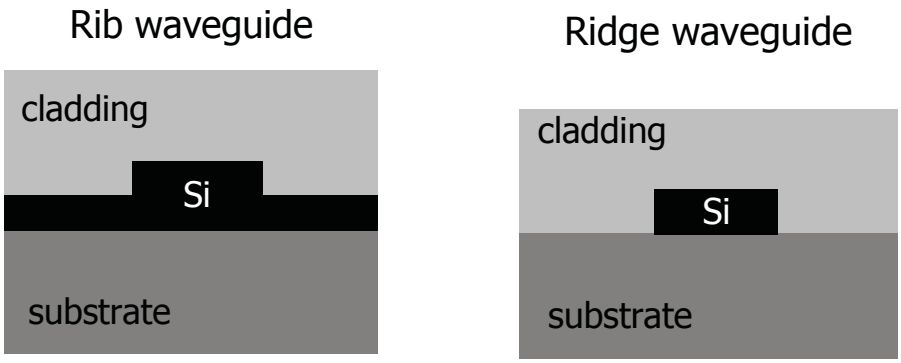

(a) (b)

Figure 1: (a) and (b) are the structures of the rib and ridge waveguides on an SOI platform.

direction of propagation (i.e., z) for the first two fundamental modes of this structure. It is observed that these modes are well confined in the guiding region as a result of the high index contrast of Si. The effective index, n_{eff}, of the waveguide is defined as

$$n_{eff} = \frac{\beta}{k_o}, \tag{8}$$

where k_o is the free-space wavenumber, $k_o = 2\pi/\lambda$. The effective index describes the propagation of a monotonic wave inside the waveguide. The effective indices of the modes in Figs., 3(a) and 3(b) are 2.39 and 1.81, respectively.

The relative power in each of the field components of these modes determines the polarization type of the mode. For example, the energy of the H_z component (i.e., magnetic field in the direction of propagation) of the mode shown in Fig. 3(a) is almost five times stronger than the energy of the E_z component. Hence,the electric field of this mode is mainly in the xy plane. Thus, this mode resembles a transverse electric (TE) mode and is called TE-like[2]. Similarly, it can be shown that the mode in 3(b) is TM[3]-like.

It should be noted that the higher order modes of this waveguide are leaky and thus this waveguide in single-mode[4]. As the dimensions of the waveguide are increased beyond the single-mode operation, more number of modes become guided. Single-mode

[2]For the ease of bookkeeping, we use the terms TE and TM for the TE-like and TM-like modes, respectively.
[3]Transverse magnetic.
[4]Although this waveguide has one TE-like and TM-like mode, through appropriate excitation, one mode can be dominantly excited. Thus, such a waveguide is called single-mode.

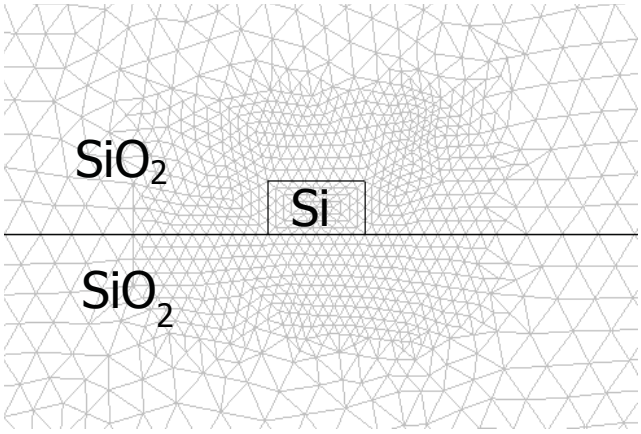

Figure 2: FEM mesh generated for a typical ridge waveguide in COMSOL software.

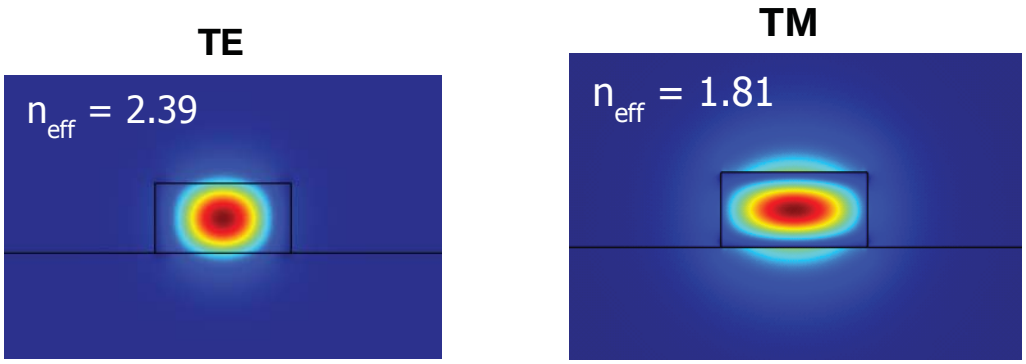

(a) (b)

Figure 3: (a) and (b) are the profiles of the Poynting vector in the direction of propagation for the fundamental TE and TM modes of a ridge waveguide, respectively. The height and width of the waveguide are 230 nm and 450 nm, respectively.

waveguides are more widely used compared to multimode waveguides, as more number of modes can unnecessarily complicate the operation of the device.

As Si is almost transparent in the optical communications wavelength ($\lambda = 1.55\mu$m), waveguide modes are inherently lossless. However, in practice, because of the presence of roughness on the sidewalls of these waveguides, the power in the guided mode couples into the radiation modes and therefore, the waveguide becomes lossy. With current fabrication quality, the typical loss of these waveguides is in the order of 1 dB/cm to 10 dB/cm [9].

2.1.2 Resonator Mode Analysis

Optical resonators are structures that trap the optical field for a long time (compared to the optical travel-time); and therefore, the intensity of optical field can be enhanced in such structures compared to waveguides. This field enhancement has several advantages; to name a few, more compact devices, and higher light-matter interaction. The latter enables more efficient nonlinear processes and low-power device tuning. As resonators have numerous applications in integrated optics, we will discuss the basics and their numerical modeling in this section.

Optical resonators are usually categorized into traveling-wave and standing-wave resonators. In traveling-wave resonators (TWRs), optical field travels around the resonator in one direction. However, in standing-wave resonators (StWRs), two contra-propagating fields travel around the resonator, and a standing-wave is formed in the resonator. TWRs are usually preferred over StWRs, as their operation and design are simpler. Throughout this work, we will only use TWRs for the design of photonic devices.

Figure 4 shows the three more commonly used types of TWRs, namely, microring, racetrack, and microdisk resonators. Microring and racetrack resonators are made by closing the end of an optical waveguide on its beginning in the form of a ring and racetrack, respectively. Hence, if the bending radii of these two types of resonators is not too sharp[5], they can be easily studied by their corresponding waveguide. For instance, if we assume that the total length of the microring resonator shown in Fig. 4 is L, and the effective index of its corresponding waveguide is n_{eff}, the resonance condition for this resonator can be written as

$$(n_{eff}\, k_o)L = 2\pi\, m\,. \tag{9}$$

where m is the azimuthal mode-number. Thus, the modes of the TWR with different m-numbers are separated by a fixed distance know as free spectral range (FSR). In the ideal

[5]At the location of the bend, the phase-front of field bends. Thus, the part of the phase-from closer to the center of the bend experiences a smaller effective index than the other extreme of the wavefront. This effect causes a change in the mode profile of the resonator and its corresponding local effective-index at the location of the bend. For Si-based resonators at $\lambda = 1.55\mu$m, the effect of bend becomes important for radius of curvature approximately less than 3 μm.

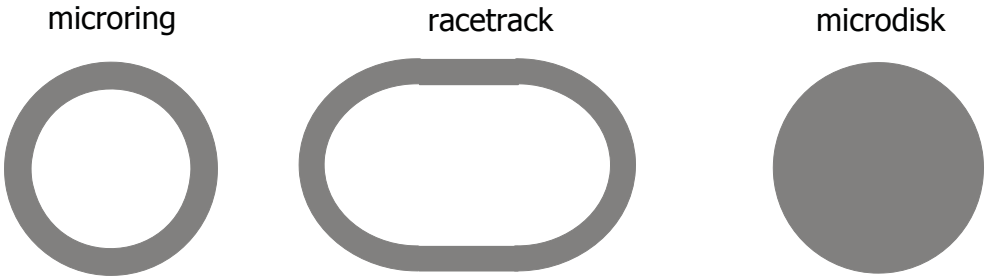

Figure 4: The structures of three most common planar TWRs, microring, racetrack, and microdisk.

case of no waveguide dispersion, n_{eff} is independent of the frequency and FSR is given by

$$\text{FSR} = \Delta\omega = 2\pi \frac{c}{L n_{eff}}. \tag{10}$$

However, in the presence of waveguide dispersion, the FSR is not fixed throughout the spectrum and can be shown that can be found using a similar expression as Eq. 10 with n_{eff} replaced by n_g, where n_g is he group index of the waveguide and is derived by

$$n_g = c/v_g = \frac{\partial n_{eff}}{\partial \omega}\omega + n_{eff}\,, \tag{11}$$

where v_g is the group-velocity and determines the energy propagation velocity of a wave packet.

On the other hand, to study the modes of microdisk or small microring resonators, the assumptions for using the waveguide mode for resonator modal analysis is no longer valid, and the Helmholtz wave Eq. 4 should be solved directly. As microring and microdisk resonators exhibit a cylindrical symmetry, their electromagnetic field components exhibit the same symmetry. Thus, the azimuthal dependence of electromagnetic field takes the form of $\exp(-jm\phi)$ and the fields can be expressed by

$$\mathbf{E} = \tilde{\mathbf{E}}(r,z)\ \exp(-jm\phi), \tag{12}$$

$$\mathbf{H} = \tilde{\mathbf{H}}(r,z)\ \exp(-jm\phi). \tag{13}$$

The position vectors r, z, and ϕ are shown in Fig. 5. By substituting the above equations into Eq. 4, the eigen-mode equation for a resonator with cylindrical symmetry is obtained. By implementing the resulting partial differential equations in COMSOL software package, resonant modes of this structure can be solved. Figure 5 shows the cross-section of a

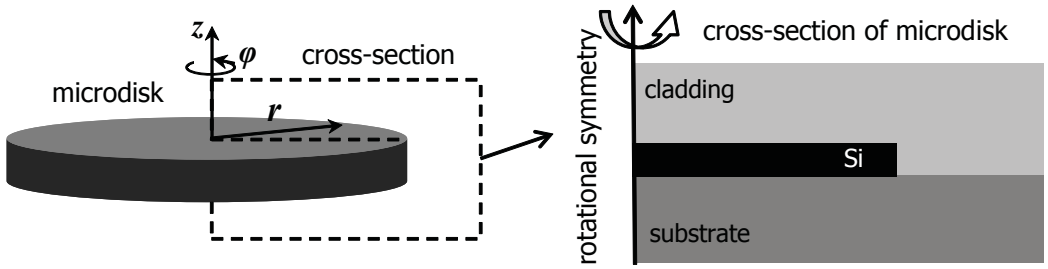

Figure 5: The structure of a microdisk resonator and its corresponding cross-section in the rz plane.

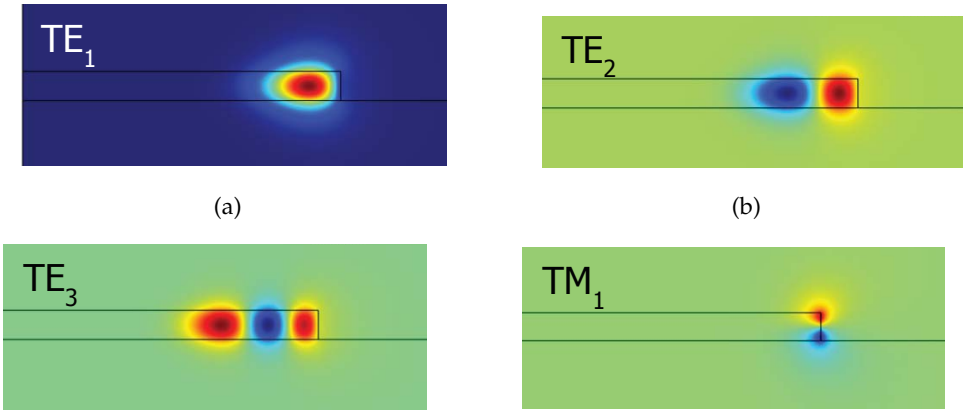

Figure 6: (a), (b), (c), and (d) show the distribution of the H_z field component of a the TE_1, TE_2, TE_3, and TM_1 modes of a 2.5 μm radius microdisk, respectively. The height of the microdisk is 230 nm and the device is covered with a SiO_2 cladding.

2.5 μm radius microdisk with Si slab thickness of 230 nm in the rz plane. Figures 6(a)-6(d) show the first three TE modes and the fundamental TM mode of this structure solved using COMSOL. The subscript represents the radial order of the mode. The multimode nature of this resonator may pose some challenges in its application for different optical signal processing devices. It is shown in [48] that through appropriate coupling, it is possible to excite only one class of radial-order modes in this device.

One important feature of the optical TWRs is the radiation of mode to the surrounding, as a result of the presence of bending in the optical path. Thus, the eigenvalues of the modes become complex, where the imaginary part of the resonance frequency accounts for the loss. To quantify the amount of loss, the quality-factor (Q) of a resonator is defined

as

$$Q_o \equiv \omega_o \frac{U(t)}{P_{loss}(t)}, \tag{14}$$

where ω_o is the resonance frequency, $U(t)$ is the energy stored in the resonator, and $P_{loss}(t)$ is the power dissipated by the resonator. Q of a resonator simply represents the ratio of the total energy of a resonator to the energy lost in one resonant cycle. It can be shown the Q can be calculated by

$$Q_o = \frac{\omega_r}{2\omega_i}, \tag{15}$$

where ω_r and ω_i are the real and imaginary parts of the complex resonance frequency of the resonator. For microdisk resonators with radii more than 2 μm, Q is larger than 10^7. In practice, the amount of loss caused by the surface roughness is much larger than the inherent radiation loss of microdisk resonators.

2.2 Coupled Mode Theory

Photonics circuits are usually designed through the coupling of various components such as waveguides and resonators. The modal analysis of these building blocks are introduced in Sections 2.1.1 and 2.1.2. Here, the temporal coupled-mode theory (CMT) that is a simple tool for studying the coupling of waveguides and resonators is presented.

The very basic device to study is a waveguide coupled to a TWR. Figure 7 shows such a configuration in which a bus waveguide is brought to the proximity of a microring resonator. As the distance between these devices becomes small, each device senses the presence of the other and they interact. Here, the input and output fields in the waveguide are defined as s_{in} and s_{out}, respective; and they are normalized such that $|s_{in}|^2$ and $|s_{out}|^2$ are the actual input and output optical power in the waveguide. Also, the amplitude of the circulating field in the resonator is defined as a, and it is normalized such that $|a|^2$ represents the energy in the resonator. Using these definitions the temporal coupling of the fields in this structure can be written as[6]

[6]It should be noticed that CMT is only valid when the coupling is weak.

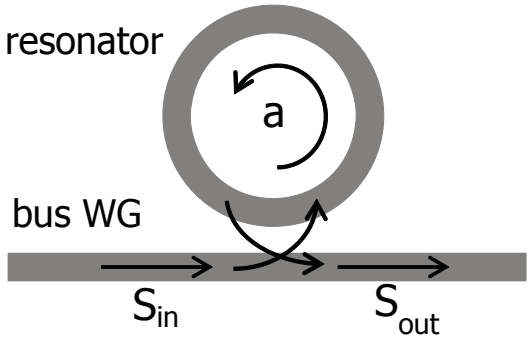

Figure 7: Schematic of a bus waveguide coupled to a TWR.

$$\begin{cases} \frac{\partial a}{\partial t} = (j\omega_o - 1/\tau_o - 1/\tau_c)a + \kappa S_{in}, \\ S_{out} = S_{in} - \kappa^* a, \end{cases} \tag{16}$$

where ω_o is the resonance frequency; and $1/\tau_o$ and $1/\tau_c$ are different loss rates of the resonator field amplitude, a. $1/\tau_o$ accounts for the intrinsic sources of loss such as material and scattering loss; and $1/\tau_c$ accounts for the rate of loss into the adjacent waveguide. κ represents the coupling of resonator field, a, to waveguide field, s_{in}, and can be shown that [49]

$$|\kappa| = \sqrt{2/\tau_c}. \tag{17}$$

Assuming a harmonic dependence of $j\omega$ for the time-domain field amplitudes, a and s_{out} are found by taking a Fourier transform from Eq. 16:

$$a(\omega) = \frac{\kappa}{j(\omega - \omega_o) + 1/\tau_o + 1/\tau_c} S_{in}(\omega), \text{ and} \tag{18}$$

$$T(\omega) = \frac{S_{out}}{S_{in}} = \frac{j(\omega - \omega_o) + 1/\tau_o - 1/\tau_c}{j(\omega - \omega_o) + 1/\tau_o + 1/\tau_c}. \tag{19}$$

Based on Eq. 15, it is shown that

$$Q_o = \frac{\omega_o \tau_o}{2}, \tag{20}$$

and similarly, coupling Q (Q_c) is defined as

$$Q_c = \frac{\omega_o \tau_c}{2}. \tag{21}$$

By combining Eqs. 19, 20, and 21 the transmission through the waveguide is derived as

$$T(\omega) = \frac{j(\omega-\omega_o)/\omega_o + 1/Q_o - 1/Q_c}{j(\omega-\omega_o)/\omega_o + 1/Q_o + 1/Q_c}. \tag{22}$$

The full-width half-maximum (FWHM) of the transmission (i.e., Eq. (22)) can be simply obtained by $\delta\omega_{\text{loaded}} = \omega_o/Q_{\text{loaded}}$, in which the loaded quality factor (Q_{loaded}) can be defined as

$$\frac{1}{Q_{\text{loaded}}} \equiv \frac{1}{Q_o} + \frac{1}{Q_c}. \tag{23}$$

Therefore, the amplitude of transmission at resonance ($\omega = \omega_o$) can be obtained from Eq. (22) as

$$T(\omega_o)^2 = \left| \frac{1/Q_o - 1/Q_c}{1/Q_o + 1/Q_c} \right|^2 = \left| 1 - 2\frac{Q_{\text{loaded}}}{Q_o} \right|^2. \tag{24}$$

There are three regimes in which the WG-resonator coupled-structure operates: (1) critical coupling, in which the coupling Q (Q_c) matches the intrinsic cavity Q (Q_o); (2) over-coupling, for which the coupling is stronger than the critical coupling $Q_c < Q_o$; (3) under-coupling, in which the coupling is weaker than the critical coupling case $Q_o < Q_c$. The amplitude and phase of these cases are depicted in Fig. 8. In the critical coupling case, all of the power is transferred from the waveguide to the resonator. However, in the over-coupling situation, the power is coupled back to the resonator. In the extreme case (i.e., $Q_c \ll Q_o$), the transmission is almost constant and equal to unity while the phase of transmission changes linearly with ω within the bandwidth of the resonator. Such a structure is an all-pass filter and will be used in this work to implement low-loss phase-shifters.

For many nonlinear and sensing applications, the intensity of light inside the resonator is of utmost importance. The highest intensity is achieved when all of the power is transferred from the waveguide to the resonator and the photon life-time inside the resonator is long. Therefore, for high intensity, critical coupling to a high finesse resonator is desirable. Knowing that the power circulating the resonator can be written as $P_{cir} = |a_{cw}|^2/T$, and

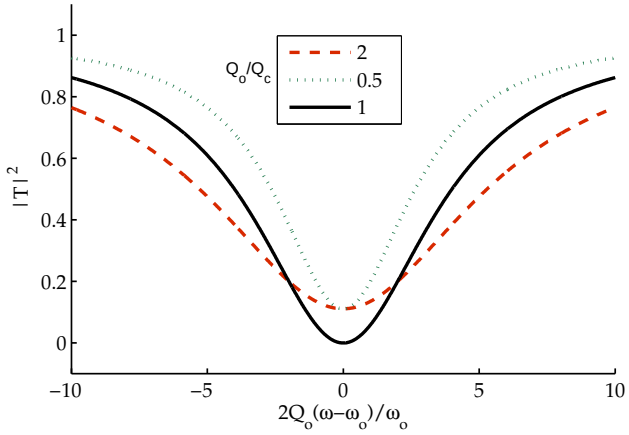

(a) Amplitude of power transmission $|T|^2$

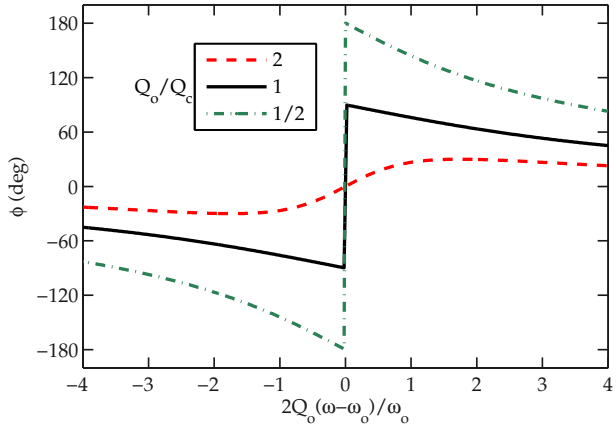

(b) Phase of transmission $\phi = \text{phase}(T)$

Figure 8: (a) The amplitude of the transmission function ($T(\omega)$) for three different ratios of Q_o/Q_c. If $Q_c = Q_o$ (i.e., critical coupling), $T(\omega_o)$ reaches zero. In the case of over-coupling ($Q_o > Q_c$) the linewidth is broadened. (b) The phase of the transmission function.

using Eq. (18) we can show that:

$$\text{(at resonance)} \qquad \frac{P_{cir}}{|S_{in}|^2} = \frac{a^2/T}{|S_{in}|^2} \tag{25}$$

$$= \frac{1/Q_c}{1/Q_c + 1/Q_o}\,(2/\pi)\frac{FSR}{\delta\omega} \tag{26}$$

$$= \frac{1/Q_c}{1/Q_c + 1/Q_o}\,(2/\pi)\mathcal{F}\,. \tag{27}$$

The first term on the right-hand side (RHS) of Eq. (27) represents the percentage of power initially dropped to the resonator, and the second term is defined as the finesse of the resonator and is a measure of the field enhancement inside the resonator.

2.3 *Heat Transport*

In this section, the basics of heat transport in thermooptic devices is introduced. As the dimension of our devices are much larger than the mean-free path of phonons in the material (except for Si slab[7]), macroscopic heat transfer equations are used throughout this work for this analysis.

2.3.1 Steady-State Heat Transport

2.3.1.1 Heat Conduction

Heat conduction is usually the most prominent means of heat flow inside solid materials. Conduction is referred to the flow of heat from a hot surface to a cold surface through atomic and molecular vibrations and is characterized by the Fourier's law

$$\mathbf{q} = -k\nabla T, \tag{28}$$

where $\mathbf{q}$ is the heat flux, T is the temperature, and k is the thermal conductivity of the material. This equation states that the rate of heat flow at a point in space is proportional to the gradient of the temperature, with the proportionality constant being the thermal conductivity of the material.

Figure 9(a) shows a slab of a uniform material with a thermal conductivity of k, thickness of L and a cross-section area of A. By integrating Eq. 28 from the left to the right surface of this slab, the total heat power passing through this slab is expressed by

$$Q = \frac{Ak}{L}(T_2 - T_1), \text{and} \tag{29}$$

$$= \frac{1}{R_k}(T_2 - T_1), \tag{30}$$

where R_k is the thermal resistance of the slab. As the thermal resistance of the material increases, the amount of temperature difference at the two ends of the slab increases for a fixed amount of heat power flow. Because of the similarity in the nature of the heat resistance and the electrical resistance, the slab shown in 9(a) can be symbolized by an

[7] As will be explained later, effective thermal properties can be used in this case to approximate the effect of phonon scattering from the boundaries.

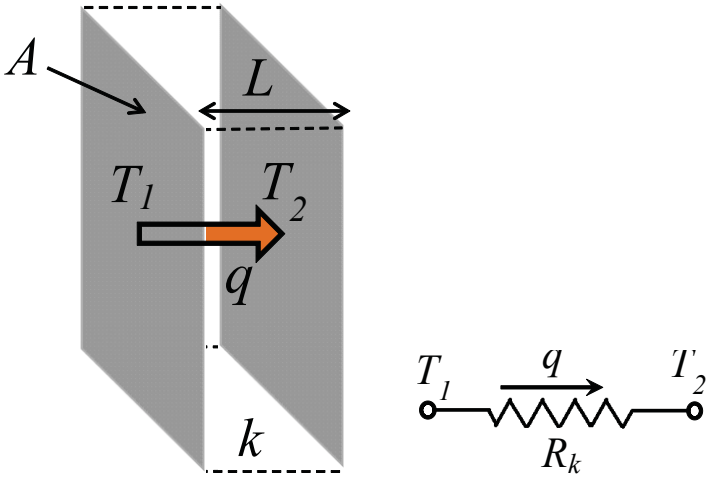

Figure 9: (a) Heat conduction model for a slab with a thickness of L, area of A, and thermal conductivity of k. Temperature at the left and right surface are T_1 and T_2, respectively. Heat power flux passing through the slab is q. (b) The equivalent electrical resistor model of the slab shown in (a). Temperature and heat flux are the counterparts of the voltage and current in this resistor.

electrical resistor as shown in Fig. 9(b). Here, heat power and temperature are the dual counterparts of current and voltage, respectively.

2.3.1.2 *Heat Convection*

At the interface of a solid and a fluid (gas or liquid), heat is most dominantly transfered through convection. Convection is referred to the transfer of heat through molecular motion or macroscopic motion of parcels of fluid. At the interface of a solid with fluid, heat flux out of the solid can be represented by the convection equation

$$q = \bar{h_c}(T_s - T_\infty), \tag{31}$$

where T_s and T_∞ are the temperatures of the surface of the solid and of the fluid (usually far from the surface), respectively. Also, $\bar{h_c}$ is the average convection heat transfer coefficient over the area of the surface in contact with the fluid. Similar to the conduction heat resistance, convection heat resistance can be defined as

$$R_c = \frac{1}{\bar{h_c} A} \tag{32}$$

where A is the area of contact between the surface and the fluid.

2.3.2 Transient Heat Transport

As we know, the temperature transient does not take place immediately when heat enters or exits a medium. Figure 10 shows the same slab as in 9(a) at a transient instance when the heat flux at its left and right surfaces is not equal. We know that the total heat entering this slab in a time, ΔT, is equal to the change in the internal energy of the slab. Thus, we have

$$[q(x) - q(x+dx)]\Delta t A = (\rho A dx)c(T(t+dt) - T(t)) + Q_s, \tag{33}$$

where Q_s is the generated heat inside the slab; c and ρ, are the specific heat capacity and density of the material, respectively. By rearranging this equation we derive the one-dimensional transient heat conduction equation

$$\rho c \frac{\partial T}{\partial t} - q_s = -\frac{\partial q}{\partial x} \tag{34}$$

$$= \frac{\partial}{\partial x}(k\frac{\partial T}{\partial x}). \tag{35}$$

where q_s is the density of generated heat inside the material. Similar to the derivation above, transient heat conduction for the three-dimensional case can be derived:

$$\rho c \frac{\partial T}{\partial t} - q_s = \nabla \cdot (k \nabla T). \tag{36}$$

2.3.3 Heat Transport Modeling

One the main focuses of in this work is the design and optimization of thermooptic devices for reconfigurable applications. In such devices, microheaters are fabricated along with the photonic devices to thermally tune their performance. There are several approximate analytical/semi-analytical solutions to the heat transport in these devices [50]. Although these approaches provide a physical insight into the device operation, they are not accurate and versatile enough to be used as a modeling approach for optimization purpose. Thus, in this work, we rely on the numerical modeling of heat transport in the devices of interest.

Figure 11(a) shows the architecture of the waveguide-microheater configuration on an SOI substrate used in this work. Here, the metallic microheater is placed on top of

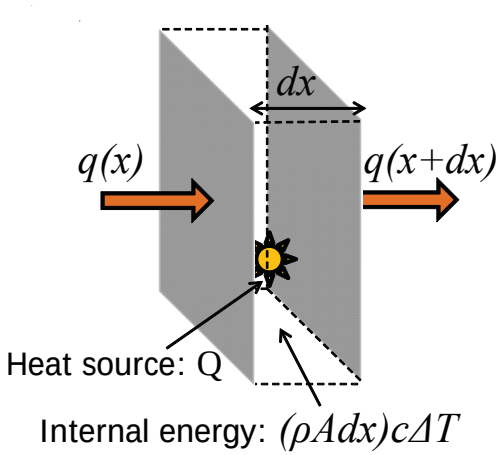

Figure 10: Heat conduction model for a slab at a transient instance . The parameters are the same as in Fig. 9(a).

the Si waveguide and is separated a distance t_{clad} by a cladding material. The details of structural parameters are shown in Fig. 11(b) and are tabulated in Table 1. The heat transport Eq. 36 is solved inside this structure with the FEM using COMSOL software package by applying appropriate boundary conditions. In these simulations, the structure is assumed to have translational symmetry and thus the cross-section of the device shown in Fig. 11(a) is modeled (Fig. 11(b)). Heat convection boundary condition is applied to the top surface of the device and isothermal boundary conditions are applied to left, right and bottom boundaries which are placed 20 μm away from the device. This large simulation window allows approximating the temperature at the boundary with zero with very good accuracy. The physical parameters are taken from different references [51]. However, for the deposited materials thermal properties might vary based on the deposition method. Here, the thermal properties are twigged to fit the modeling results to experimental results. All the physical parameters used for heat transport modeling are found in Table 2. As the thickness of the Si slab is around 200 nm and close to the mean-free path of phonons inside the slab, effective thermal conductivity is used for this material [52].

Figure 11(b) shows the distribution of temperature at the cross-section of waveguide-microheater configuration. White arrows show the heat flux in this structure. As seen in this figure, heat flux starts at the metallic microheater and diffuses through the structure.

Table 1: Device Parameters

BOX thickness	t_{BOX}	1 μm
cladding thickness	t_{clad}	1 μm
microheater thickness	t_h	100 nm
microheater width	W_h	1 μm
waveguide thickness	t_{wg}	220 nm
waveguide width	W_{wg}	480 nm

Table 2: Modeling Parameters

Material	$\rho(\frac{kg}{m^3})$	$c(\frac{J}{KgK})$	$k(\frac{W}{mK})$
Si	2330	703	163
Thermal SiO2	2203	733	1.38
PECVD SiO2	2203	650	1
LPCVD SiN	2500	170	20
Ni	1300	800	70

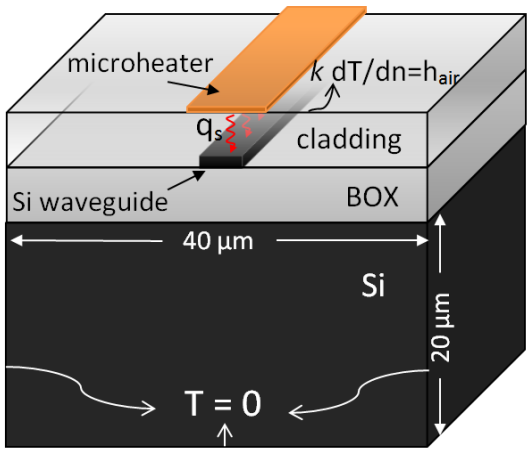

(a)

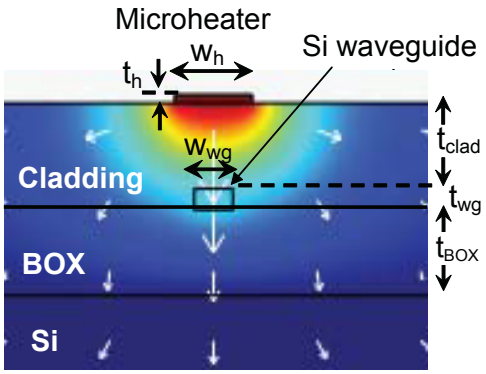

(b)

Figure 11: (a) Architecture of the metallic microheater over a Si waveguide on an SOI wafer. (b) Distribution of temperature at the cross-section of a SOI waveguide as heat is generated in the metallic microheater. White arrows shows the heat flux in this device.

CHAPTER III

OPTIMIZATION OF METALLIC MICROHEATERS

The vast optical signal processing capabilities enabled by reconfigurable photonic devices calls for a low-power and fast reconfiguration technology. At the same time, this technology should be CMOS-compatible, so that the whole Si photonic device is reliably and inexpensively fabricated using a CMOS fabrication facility. As discussed in Section 1.3.1, microheaters that are based on the thermooptic effect in Si are a powerful device for this reconfiguration purpose. However, these devices are usually slow (few microseconds to millisecond), and one of the main focuses of this work is to improve the reconfiguration speed of these device.

3.1 Device Architecture and Numerical Modeling

Figure 12 shows the architecture of the waveguide-microheater configuration on an SOI substrate which is considered in this work. Here, the metallic microheater is placed on top of the Si waveguide and is separated by a cladding material by the distance t_{clad} to avoid optical loss. Device dimensions are tabulated in Table 3. Figure 12 also shows the distribution of temperature at the cross-section of waveguide-microheater configuration. White arrows show the heat flux in this structure. The details of heat transport modeling are found in Section 2.3.

Throughout this work, the cladding thickness, t_{clad}, is taken 1 μm, which is the smallest possible thickness with negligible optical radiation loss. Since the goal in this optimization is to achieve faster devices, thinner cladding layer is used as it results in smaller heating volume and faster thermal response. The thickness of the BOX layer is 1 μm and the waveguide cross-section is $220 \times 450\text{nm}^2$, in this example. The cladding material is SiO_2 and microheater material is nickel (Ni). To maximize the overlap of microheater temperature profile with optical mode of the waveguide, a simple single-strip microheater that is

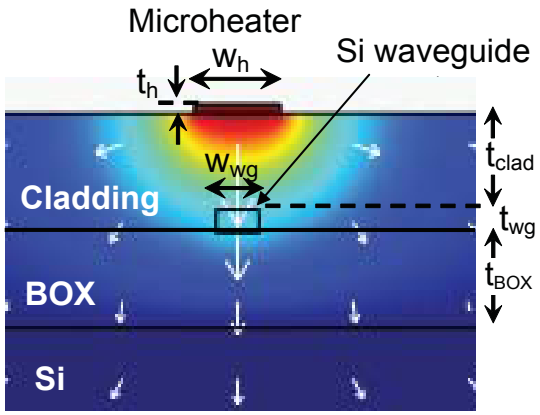

Figure 12: The architecture of the metallic microheater over the Si waveguide. The color profile shows the distribution of temperature at the cross-section of a SOI waveguide as heat is generated in the metallic microheater. White arrows shows the heat flux in this device.

Table 3: Device Parameters

BOX thickness	t_{BOX}	1 μm
cladding thickness	t_{clad}	1 μm
microheater thickness	t_h	100 nm
microheater width	W_h	1 μm
waveguide thickness	t_{wg}	220 nm
waveguide width	W_{wg}	480 nm

laterally co-centered with the waveguide is considered in this work as shown in Fig. 12.

One of the most important geometrical parameters in the optimization of the response of metallic microheater devices is the thickness of the BOX layers. Figures 13(a) and 13(b) show the rise/fall-time and steady-state temperature rise at the center of the Si waveguide for different thicknesses of BOX layer, respectively . The rise-time (fall-time) is defined as the time by which the temperature rises (falls) from 10% to 90% (90% to 10%) of the steady-state value when a step signal is applied to the microheater. Moreover, throughout this paper, the temperature rise in the Si waveguide is calculated for 1 mW of power dissipation over a 20 μm diameter microring resonator (i.e., 1mW/62.8μm) with the same radial cross-section as that of the simulated waveguide-microheater configuration (Fig. 12) . This microring resonator will be further used in our experiments to characterize the reconfiguration speed and power consumption of the designed microheaters. It is seen in

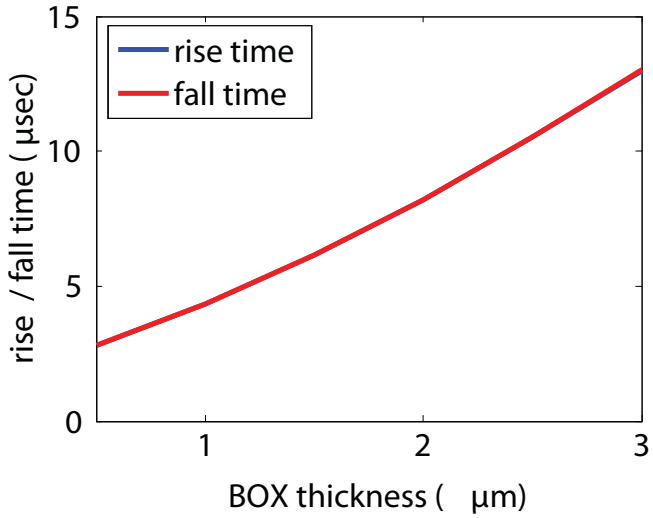

(a)

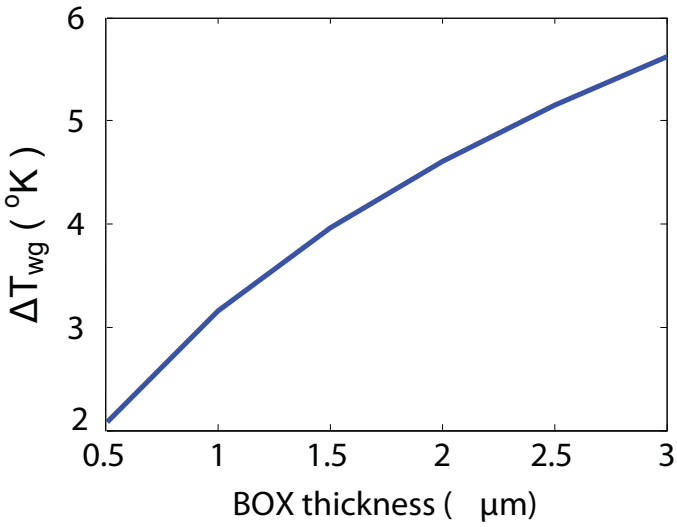

(b)

Figure 13: (a) Simulation results of the effect of BOX thickness on the rise-time and fall-time of temperature at the center of waveguide (b) Simulation result of the temperature rise at the center of the waveguide for 1mW power dissipation over a 20 μm diameter ring . The width of the microheater is 0.5 μm in these simulation.

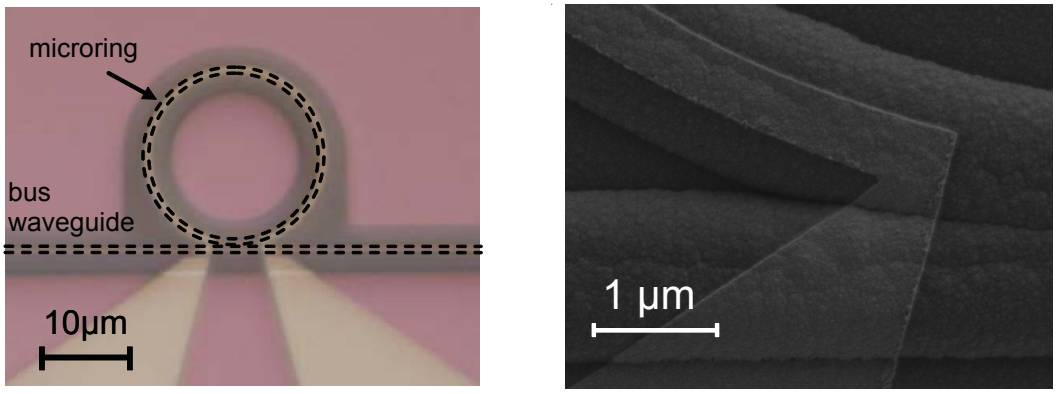

(a) (b)

Figure 14: (a) Optical micrograph of a 20 μm diameter microring with a 0.5 μm wide micro-heater on top. Resonator is side-coupled to a bus waveguide. (b) SEM of the microheater of the same device shown in (a).

Figs. 13(a) and 13(b) that the response of the microheater becomes faster at the price of less temperature rise or higher power consumption. Since, in this work, we are aiming to increase the reconfiguration speed of microheaters, thinner BOX layers are chosen. It should also be noted that the BOX layer should be kept thick enough to avoid leakage of the optical field into the substrate. 1 μm BOX guarantees that radiation to substrate is negligible and this thickness is chosen for the actual devices fabricated in this study.

3.2 Fabrication and Characterization

The performance of the microheater-waveguide configuration studied in the Section 3.1 can be characterized by fabricating a device based on this configuration and by monitoring its transmission properties as heat is dissipated in the microheater. Here, we fabricated 20 μm diameter microring resonators with same radial cross-section as shown in Fig. 12. As the radius of the bend is much larger than the variations of both optical field and temperature distribution, previous simulations for the waveguide with translational symmetry can be used with a good accuracy for the microring device with cylindrical symmetry. The device is fabricated on Soitec SOI wafers with the Si slab thickness of 220 nm, and a BOX layer of 1 μm thickness. The widths of the bus waveguide and microring are 450 nm to assure singlemode operation. First, the pattern of the device is written on

ZEP electron-beam resist using electron-beam lithography (JEOL 9300) and etched into Si by inductively-coupled-plasma (ICP) etching using a combination of Cl_2 and HBr gases (STS ICP). After this step, 1 μm SiO_2 is deposited using plasma-enhanced chemical-vapor-deposition (PECVD) and microheater patterns are defined by a lift-off process using ZEP electron-beam resist and electron-beam-evaporation. Microheaters are composed of 75 nm thick Ni and contact pads are covered with 150 nm gold (Au) for better electrical contact. To increase the yield in fabrication, we just perform one step lift-off process for both Ni and Au at the locations of microheaters and contact pads. In another lithography step, the area on the heating element (over the photonic device) is opened using ZEP resist, and Au is removed using Ni-safe Au etchant, GE-8148 (Transcene Inc.). The Au over the heating element is removed for higher electric resistance and higher power dissipation over the photonic device. Figure 14(a) shows the optical micrograph of the fabricated microring with integrated microheaters. Dashed lines depict the edges of the underlying photonic device. Figure 14(b) shows the scanning-electron micrograph of a 500 nm wide microheater over the microring.

The performance of the microheater is characterized by measuring the transmission of the fabricated microring using a standard optical characterization test setup, while different drive signals are applied to the microheater. The optical transmission is measured by coupling the TE-polarized light from a swept-wavelength tunable laser into the input waveguide, while the output of the device is coupled into a photodetector, and the data is transferred to a PC using a data-acquisition (DAQ) card. The drive signal of the microheater is applied using an RF probe (Microtech Inc.). Figure 15(a) shows the transmission spectra of the microring for different power dissipation values in the 500 nm wide microheater. It is observed that the resonance wavelength of microring is red-shifted as power dissipation is increased in the microheater. The resistance of this microheater is 590Ω at small power dissipations and increases almost linearly with power consumption by 34Ω/mW. This can be translated to 0.36°K/Ω change in the temperature of the microheater. Hence, the microheater can also be used as a thermistor in this device [53].

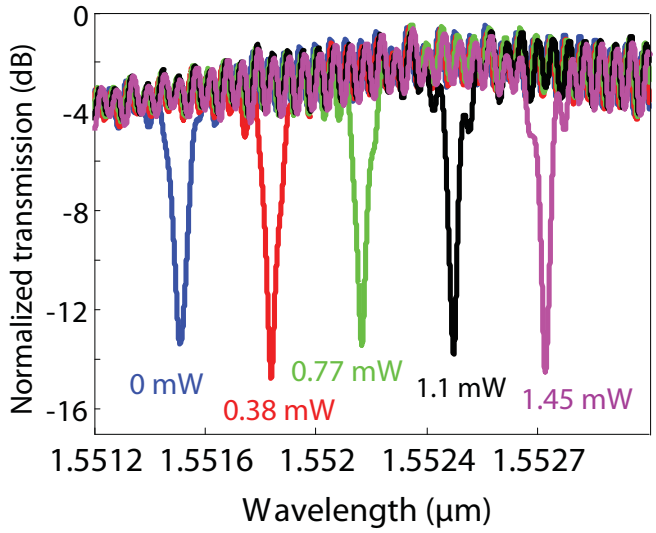

(a)

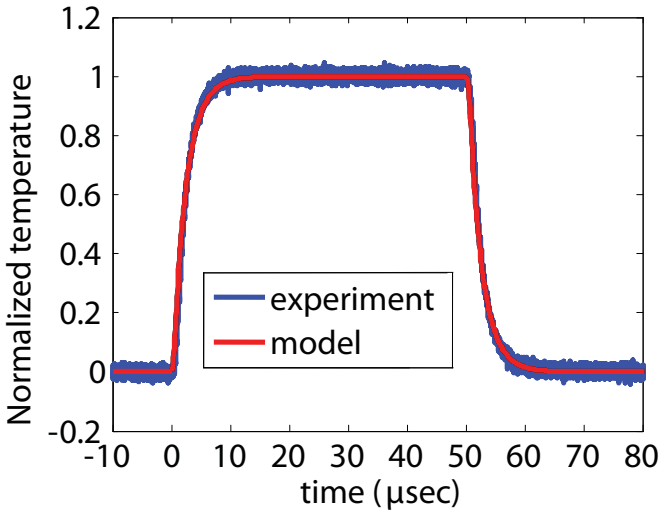

(b)

Figure 15: (a) Normalized transmission of the microring shown in Fig. 14(a) for different power dissipations in the microheater. (b) Experimental and simulation results of the normalized step response of the same microheater as in (a).

To measure the step-response of the microheater, the laser wavelength is fixed at the linear region of the microring resonance line-shape. Then a small-signal step is applied to the microheater, and the output of the microring is monitored on an oscilloscope. Applied signal should be small enough so that the laser wavelength remains in the linear region of the resonance. Figure 15(b) depicts the measured normalized step-response of the microheater along with the simulation results. Perfect agreement is obtained between measurement and simulation results. It is observed that the rise-time and fall-time of the microheater is around 4 μs.

3.3 Microheater Optimization

As discussed in Section 3.1, a single-strip microheater co-centered with the underlying photonic device is an efficient structure in terms of power consumption. The effect of the width of this microheater is studied in this section. Also, as shown in Section 3.1, to assure faster reconfiguration time, the minimum possible thickness of the BOX and cladding layers ($\approx$ 1 μm) should be used. Although BOX layer thermal properties are always fixed, the choice of the cladding material will affect the thermal response of the device and its effect is studied in this section.

3.3.1 Microheater Width

Figure 16(a) shows the simulation and experimental results of the temperature rise in the center of the Si waveguide as 1 mW power is dissipated in microheaters with different widths over a 20 μm diameter microring. It is observed that temperature rise is larger in narrower microheaters, and hence, they are more power efficient. To compare the experimental and simulation results, power dissipation in Au pads and thin-film connectors are extracted and numerical results are adjusted to take this power loss into account. We see that relatively good agreement between simulation and experimental results is obtained. The vertical axis on the right of Fig. 16(a) also shows the amount of frequency shift of the microring versus power dissipation.

Rise-time and fall-time of microheaters are also measured and shown in Fig. 16(b) for different microheater widths along with the simulation results. It is observed that as the

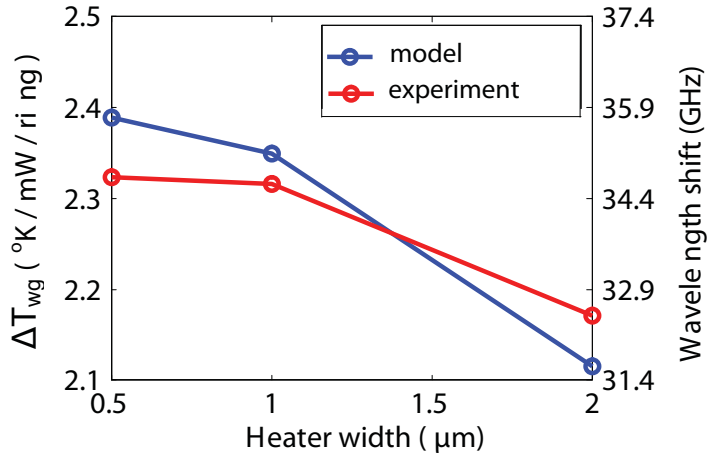

(a)

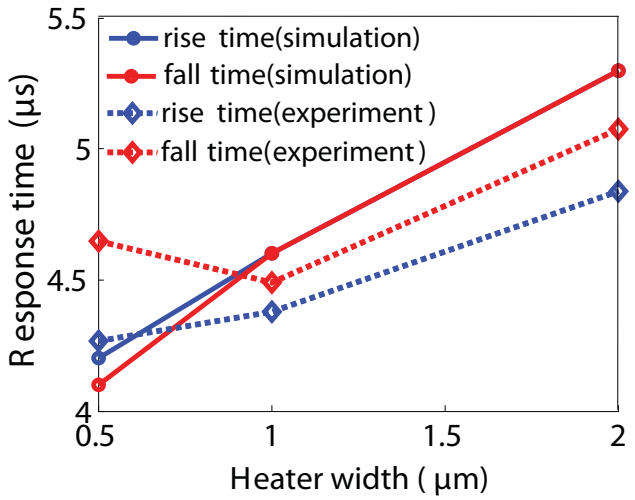

(b)

Figure 16: (a) Experimental and simulation results of the temperature rise in the core of a 20 μm diameter microring for different microheater widths. Vertical axis on the right shows the redshift in the resonance frequency (b) Experimental and simulation results of temperature rise-time and fall-time of microheaters with different widths.

width of the microheater is reduced, its reconfiguration time is decreased. This can be explained as a result of a smaller heating volume for narrower microheaters. However, as the width of the microheater becomes smaller than the lateral heat diffusion length (few micrometers), the improvement in the speed and also power consumption saturates. Hence, there is no need to further reduce the width of the microheater beyond 500 nm. The frequency response of these microheaters are also measured. For this measurement, a small-signal sinusoidal with frequency f is applied to the microheater. The optical output of the microring with a $2f$ frequency content (optical response is linear with respect to power dissipation) is locked to the double-frequency ($2f$) of the drive signal in a lock-in amplifier. From these measurements, the 3dB bandwidth of microheaters with widths of 2 μm, 1 μm, and 0.5 μm are measured to be 109 KHz, 132 KHz, and 139 KHz, respectively. This results also supports our previous observation that narrower microheaters reconfigure faster.

3.3.2 Cladding Material

One other important factor that affects the performance of microheaters, and is usually ignored, is the effect of cladding material. Conventionally, PECVD SiO_2 is used for cladding, because of the ease of fabrication and its CMOS-compatibility. An alternative material that can be used as the cladding is SiN. It has been shown before that SiN films deposited with low-pressure CVD (LPCVD) have high thermal conductivities (10 to 20 times more than PECVD SiO_2). Higher thermal conductivity is a requirement for faster heat diffusion. We fabricated the same devices as explained in Section 3.2 with LPCVD SiN cladding and measured their thermal response. Figure 17(a) shows the frequency response of the 1 μm wide microheater with PECVD SiO_2 and LPCVD SiN claddings. It is seen that the 3dB bandwidth is increased by 23% from 132 KHz with PECVD SiO_2 cladding to 162 KHz with LPCVD SiN cladding. Figure 17(b) compares the normalized step-response of these microheaters at the rise and fall of the drive signal. It is observed that the response of these devices are almost the same at large time-scales (≥ 1 μs). However, the device with LPCVD SiN cladding shows faster response at small time-scales (≤ 1 μs). The reason for the similar

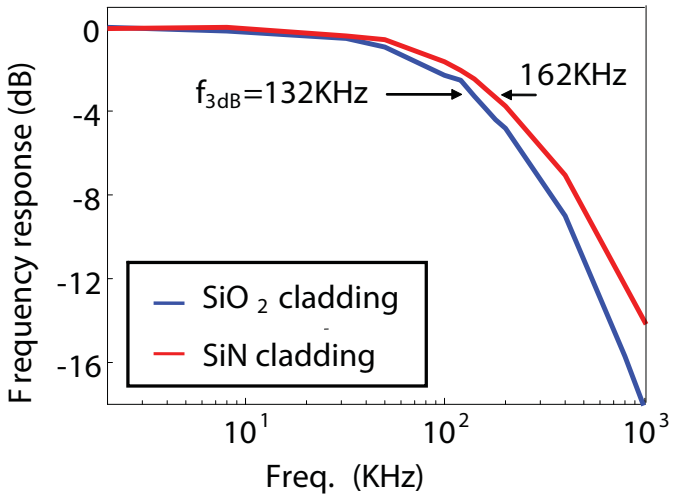

(a)

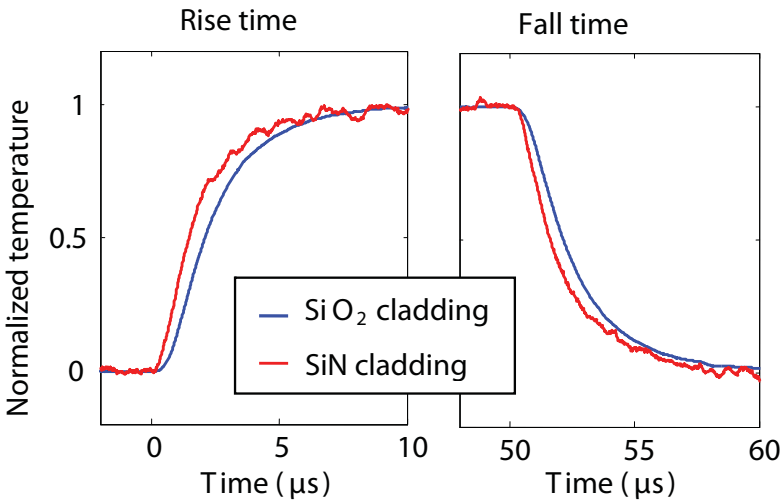

(b)

Figure 17: (a) Frequency response of microheaters with the width of 1 μm with PECVD SiO_2 and LPCVD SiN cladding. (b) The normalized step-response of the same microheaters as in (a) at the rise and fall edge of the drive signal.

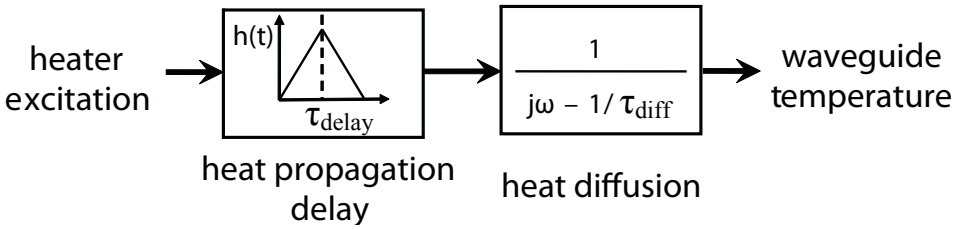

(a)

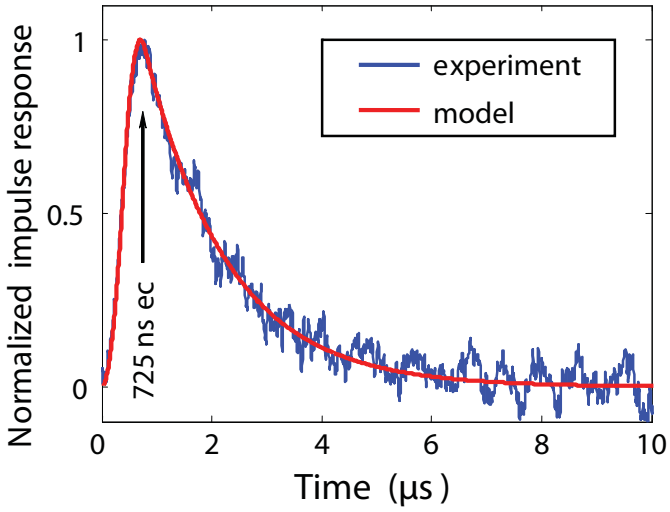

(b)

Figure 18: (a) Proposed model for heat transport in conventional microheaters. (b) Experimental result of the normalized impulse response of the microheater with a width of 1 μm and that of the fitted model shown in (a).

responses at large time-scales is the same order of thermal "RC" time-constant in SiO_2 and SiN claddings, as a result of the high specific heat capacity of SiN compared to SiO_2. However, at short time-scales when the steady-sate is not reached, thermal conductivity plays a much more important role in the response of the device, and thus, the SiN-clad device has a faster response. This behavior can be advantageous for pulsed-excitation of microheaters that is discussed in Section 3.5. The power consumption of these devices are also measured and it is found that the high thermal conductivity of SiN cladding results in 35% more power consumption compared to the device with SiO_2 cladding.

3.4 System-Level Model

Although it was shown in the Section 3.2 that simulation and experimental results match almost perfectly at large time-scales, the modeling accuracy reduces for shorter time-scales. This is mainly as a result of second-order heat transport effects such as the thermal contact resistance, which are not included in the modeling. In this section, a system-level model is introduced which is capable of accurately predicting the response of microheaters both at short and large time-scales.

Figure 18(a) shows the proposed model that is composed of a block with a delay-like response cascaded with a first-order linear-time-invarient (LTI) system. The delay is caused by the heat propagation from the microheater to the Si waveguide. The delay in the proposed model is intuitively chosen and it is seen that the combination of this delay with the first-order system fits to the actual response of the microheater with very good accuracy. The effective delay of this block is τ_{delay} and is shown on the delay response in Fig. 18(a). Also, the first-order LTI system with a time-constant of τ_{diff} models the heat diffusion in a simple layered structure. The model parameters are extracted for a 1 μm wide microheater by fitting the experimentally measured response to that of the model, resulting in $\tau_{delay} = 400\ ns$ and $\tau_{diff} = 1.5\mu$s. Figure 18(b) shows the experimental result for the normalized impulse-response of the described microheater along with the impulse-response of the proposed model. Experimental impulse response is evaluated by taking the derivative of the measured step-response of the system. It is observed that there is a good agreement between the experimental and modeling results both at short and large time-scales. We also observe a 725 ns delay in the impulse-response of this structure. This reveals that even by applying a high-energy pulse at the beginning of the excitation, reconfiguration in less that 725 ns is impractical. This limitation that is shown for the first time in this work is the ultimate reconfiguration speed limit in these type of microheaters.

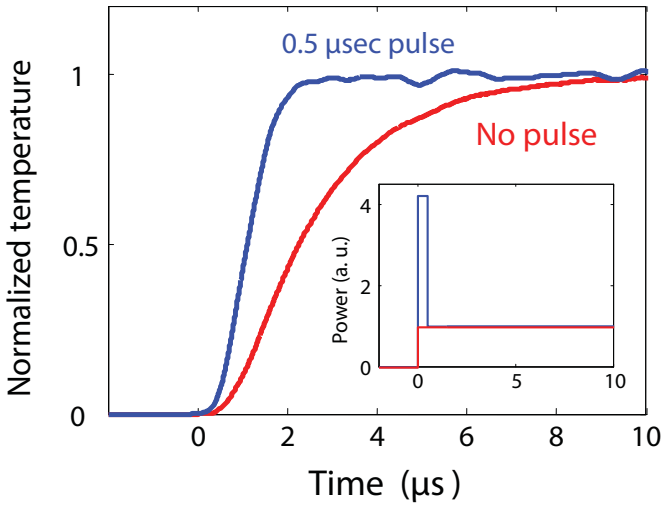

Figure 19: Experimental results of the response of 1 μm wide microheater to a step signal with (blue curve) and without (red curve) pulsed-excitation. Inset shows the power dissipation signals for the two cases.

3.5 Pulsed-Excitation of Microheaters

In Section 3.3, it was shown that the rise-time of the microheaters is around 4 μs. However, he detailed study of the impulse-response of these microheaters showed a heat propagation delay of about 700 ns. One approach to increase the reconfiguration speed of microheaters up to the limit posed by this heat propagation delay is through applying high-energy pulses at the beginning of the drive signal [54, 55]. Blue and red curves in Fig. 19 show the experimental results for the step-response of the microheater with and without the high-energy excitation pulse, respectively. For the pulsed-excitation response, we have considered a 500 ns high-energy pulse at the beginning of the excitation signal to enhance the rise-time of the system (inset of Fig. 19). It is observed that the rise-time of the device is reduced from 4.2 μs to almost 1 μs through pulsed-excitation. By shortening the duration of the pulse and increasing its peak-power up to 725 ns rise-time is achievable with practical peak-power levels.

3.6 Conclusion

The architectural and material optimizations on the microheaters, enhanced the reconfiguration times to approximately 4 μs. Also, through a pulsed-excitation approach, the

settling time of these microheaters is reduced to 725 ns. This is the limit in the reconfiguration time of the devices considered in this chapter, and it is imposed by the heat propagation delay from the microheater to the photonic device. In Chapter 4 a novel microheater architecture is proposed that improves the reconfiguration speed by one order of magnitude.

CHAPTER IV

ULTRAFAST SMALL-MICRODISK PHASE-SHIFTERS

As discussed in Chapter 3, it is challenging to improve the thermal reconfiguration speed beyond hundreds of nanosecond using conventional microheater-over-cladding architecture. Here, we propose and experimentally demonstrate a novel microheater design that is integrated with small microdisk resonators (diameter less than 5 μm) with sub-100-nanosecond reconfiguration time. This device has the potential to perform as a low-power, low-loss and ultra-compact phase-shifter for reconfiguration of Si photonics devices.

4.1 Device Architecture

In the conventional microheater architectures discussed in Chapter 3, microheater is usually separated by the photonic device through a cladding material which is usually SiO_2. The small thermal conductivity of the cladding material causes a heat propagation delay in the order of a few hundreds of nanosecond in such devices. As discussed in Chapter 3, this heat propagation delay limits the reconfiguration time to a few hundreds of nanosecond (725 ns in our optimized device). To reduce the heat propagation delay, we propose to use the Si slab for heat conduction because of its high thermal conductivity. As the placement of metal can cause a lot of absorption loss, heaters should be placed far from the optical mode. One particular device compatible for the implementation of this idea is a microdisk resonator, in which the mode is confined to the edge of the disk. Thus, microheaters can be directly placed on the Si layer toward the center of the microdisk and far enough from the optical mode of the resonator.

Figure 20 shows the cross-section of the H_z field profile of the first-order radial mode of a 2.5 μm radius microdisk resonator. It is observed that this mode extends approximately 1 μm toward the center of the microdisk. Thus, the microheater can be placed toward the center of the microdisk and far from the optical mode to avoid optical loss. Heat

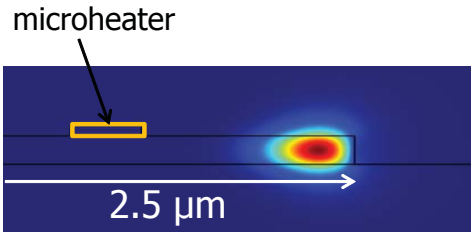

Figure 20: H_z field profile of the TE_1 mode of a 2.5 μm radius microdisk. The orange box on top of the microdisk shows the location of a metallic microheater placed far enough from the optical mode to prevent loss.

transport in this device is modeled using three-dimensional FEM with the COMSOL software package. Figures 21(a) and 21(b) show the horizontal (in the plane of the microdisk) and vertical (normal to the plane of the microdisk) cross-sections of the distribution of temperature inside a 2.5 μm radius microdisk, respectively. Microheater width is 0.5 μm and is placed 1.5 μm from the edge of the microdisk. It is seen that the surface of the Si is equi-temperature because of the high thermal conductivity of the Si. Figure 22 shows the normalized temperature rise inside the new design and the conventional microheater structure. It is seen that the rise-time of the new design is 3 μs as compared to the 4.4 μs in the conventional device. On the other hand, it is observed that the heat propagation delay in the response of the conventional microheater is considerably reduced for the new microheater design. To better investigate the heat propagation delay properties, normalized impulse response of the heater shown in Figs. 21(a) and 21(b) is depicted in Fig. 23. It is observed that the heat propagation delay is reduced to 25 ns in this device as compared to hundreds of nanosecond in the conventional design. Thus, it is expected that is device can offer sub-100-nanosecond reconfiguration time using pulsed excitation.

4.2 Device Fabrication

To verify the modeling results, 5 μm diameter microdisk resonators are fabricated on SOI wafer with Si slab thickness of 230nm, and a buried oxide layer of 1 μm. After the fabrication of photonic components on Si slab using electron-beam lithography (EBL) and ICP etching, 1 μm SiO_2 is deposited using PECVD and via holes are etched at the center of the microdisk resonator for the placement of the heaters. To assure good electrical connectivity

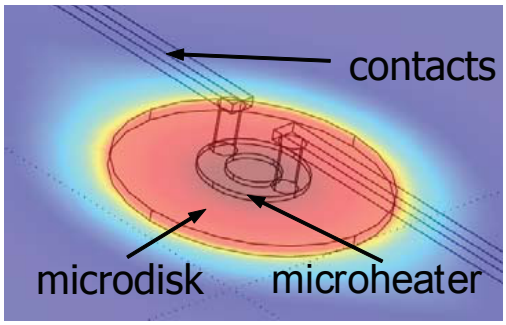

(a)

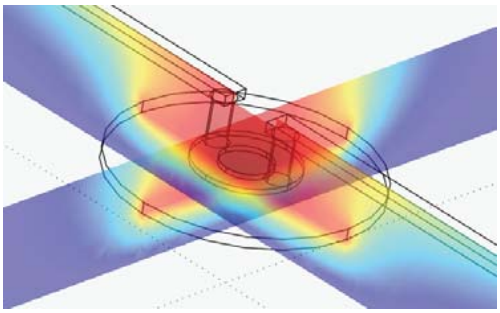

(b)

Figure 21: (a) and (b) show the distribution of temperature at the horizontal and vertical cross-sections of a 2.5 μm radius Si microdisk, respectively. The thickness of the BOX is 1 μm. The cladding layer is SiO_2 with a thickness of 1 μm. Microheater is composed of Ni with a width of 0.5 μm and is placed 1.5 μm from the edge of the microdisk.

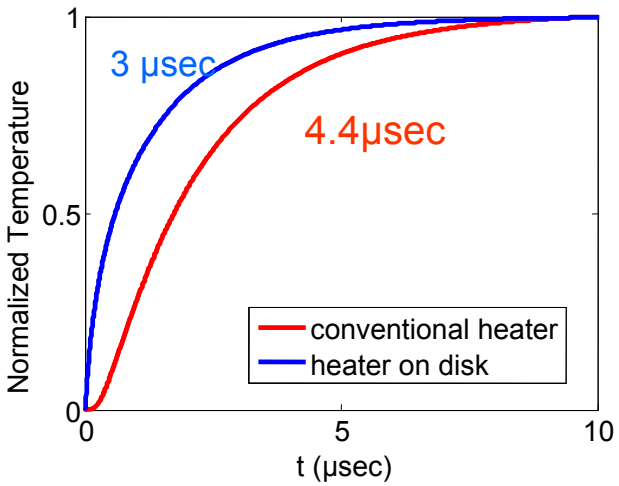

Figure 22: The normalized step-response of the microheater-on-microdisk design and the conventional microheater design placed over the cladding. The thickness of the BOX layer is 1 μm and the cladding is SiO_2 with a thickness of 1 μm for both cases.

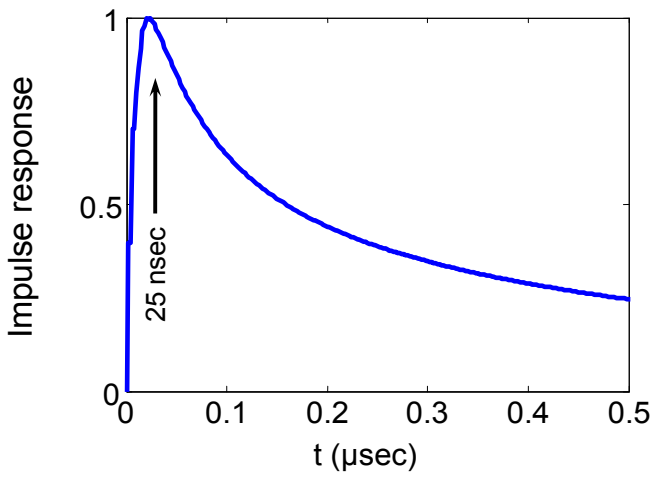

Figure 23: The modeling result for the normalized impulse-response of the microheater configuration shown in Figs. 21(a) and 21(b).

of microheaters, ZEP resist is reflowed for 30 minutes at 160^{o}C on hot plate which resulting in a via sidewall angle of 55 to 60 degrees. Etching of via is stopped approximately 50 nm left to the surface of the Si slab through a well-controlled etching process. Then, the remaining SiO_2 is wet-etched using buffered-oxide-etchant (BOE) so that the surface of Si is not damaged by the plasma bombardment (Fig. 24(b)). Microheater patterns are then defined using EBL and electron-beam evaporation through a liftoff process. 140 nm NiCr and 80 nm Au are deposited for microheater and connectors/pads, respectively. More details of the fabrication process is found in Section 3.2. Figure 24(a) shows the SEM of the fabricated microheater-on-microdisk design with a microdisk diameter of 5 μm. The width of the microheater is 0.3 μm and placed 1 μm from the edge of the microdisk. The dotted lines approximately show the photonic device underneath the cladding. Figure 24(b) shows the cross-section of a an etched via. Thanks to the good control on the etching step, the surface of the crystalline Si is not damaged.

4.3 Device Characterization

To characterization the performance of the small microdisk structure, a 5 μm diameter microdisk is fabricated in an add-drop configuration with the microheaters directly fabricated over the microdisk (Fig. 24(a)). The SEM of the device before the deposition of the

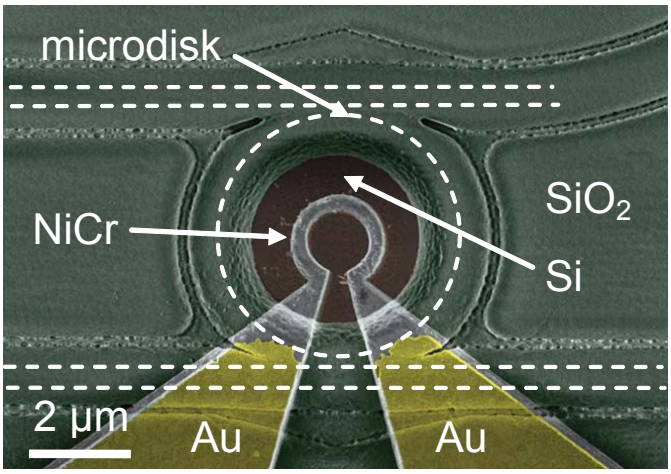

(a)

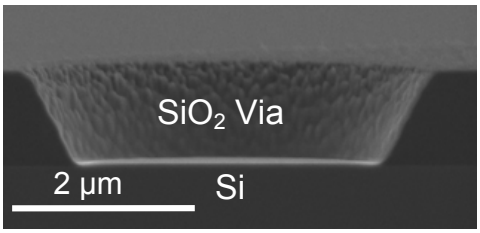

(b)

Figure 24: (a) The SEM of the fabricated microheater-on-microdisk design with a 5 μm diameter microdisk. The width of the microheater is 0.3 μm and placed 1 μm from the edge of the microdisk.

cladding material is shown in Fig. 25(a). The width of the bus waveguide at the coupling region to microdisk is 365 nm to satisfy phase-matching condition for strong coupling. Figure 25(b) shows the normalized transmission of the microdisk at its drop-port for zero microheater power dissipation. The bandwidth of the device is 0.33 nm thanks to the good phase-matching of the bus waveguide to the microdisk. By applying voltage across the microheater, the temperature of the microdisk is increased and its resonance wavelength is red-shifted (Fig. 30). The step-response of these microheaters is measured by fixing the laser wavelength at the linear region of the resonance line-shape of the drop port and by applying a small-signal step voltage to the heater and monitoring the optical output of the system on an oscilloscope. Figure 26 shows the rise and fall step-responses of this device.

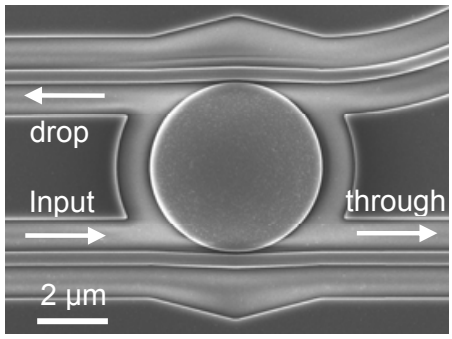

(a)

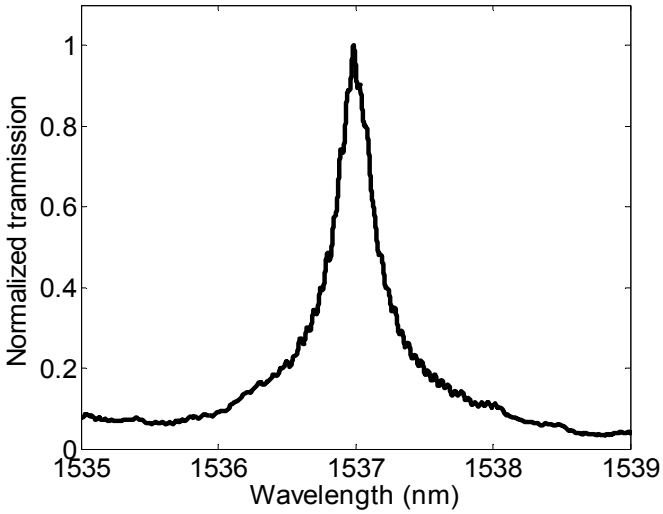

(b)

Figure 25: (a) The SEM of the fabricated add-drop microdisk filter. The diameter of the microdisk is 5 μm and the width of the waveguides is 365 nm. (b) Transmission spectrum of one mode of the device shown in (a) at the drop port.

The rise-time and fall-time of this device are measured to be 2.4 μs.

To characterize the pulsed-excitation property of this device, a 25 ns pulse is applied to the heater. Figure 27 shows the normalized response of the heater to this pulse. The heat propagation delay is measured to be 75 ns that is considerably smaller compared to that of conventional microheaters. However, this delay is not as small as that predicted by 3D simulation results of heat transport. One assumption considered in the modeling is the zero thermal-contact-resistance between different deposited materials. This assumption can result in an error for the estimation of the heat propagation delay. It is expected

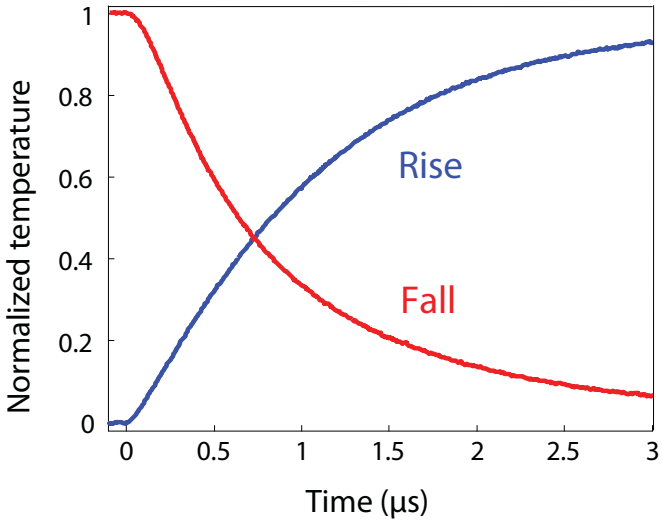

Figure 26: The normalized rise and fall response of the device shown in 24(a).

that through long annealing time, thermal-contact-resistance between the Si slab and the PECVD SiO_2 cladding to improve considerably. Also, it is expected that the metallic microheater to form silicide with the Si layer through rapid thermal annealing (RTA) at high temperatures, resulting in improved thermal contact.

4.4 System-Level Model

The numerical modeling of heat transport for microheaters provide an accurate estimate of the response of these devices. However, to gain more insight into the operation of the device, it is useful to derive a system-level model. In Section 3.4, a simple and accurate system-level model was proposed for the conventional microheaters. This model was composed of the cascade of a delay-like system and a first-order LTI system. By studying the response of the new microheater-on-microdisk design, it is found that the response of this device can be approximated using a similar model (Fig. 28(a)). However, the first-order system should be replaced by a second-order system ($h_2(t)$ in Fig. 28(a)) to better emulate the response of the new device. Figure 28(a) shows the block-diagram of the proposed model. In this model, τ_d is the delay of the delay-like system ($h_1(t)$); and τ_{sl} and τ_f are the slow and fast time-constants associated with the poles of the second-order system ($h_2(t)$), respectively. Also, the ratio between the slow and fast parts of $h_2(t)$ is

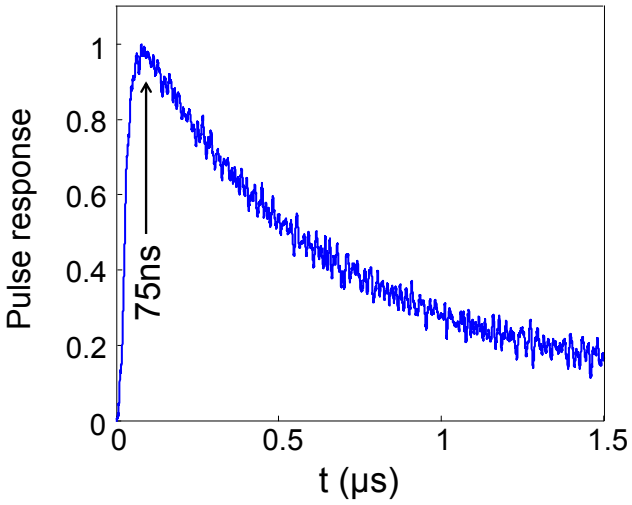

Figure 27: The normalized response of the device shown in Fig. 24(a) to a 25 ns pulse applied to the microheater.

denoted as c. This model is fitted to the pulsed-response shown in Fig. 27 and the result is shown in Fig. 28(b). A very good agreement between the model and experimental data is achieved. The parameters of the optimized model are

$$\begin{cases} \tau_d = 22\ ns \\ \tau_{sl} = 0.6\ \mu s \\ \tau_f = 3.57\ \mu s \\ c = 0.135 \end{cases} \tag{37}$$

4.5 Pulsed-Excitation of Microheaters

As observed in Section 3.5, applying a high-energy pulse to the excitation signal can improve the reconfiguration time of the microheater. The same approach can be used here for the microheater-on-microdisk design. Thanks to the system-level model, which was developed in Section 4.4, the exact excitation signal needed to excite the microheater from one state to the other can be easily derived. To find the appropriate pulsed-excitation signal, the excitation pulse used for the characterization of the device, $p(t)$, is passed through a filter which compensates the slow response of the second-order system. This

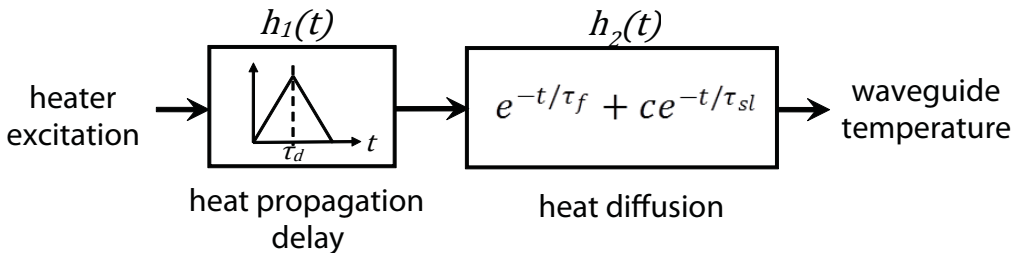

(a)

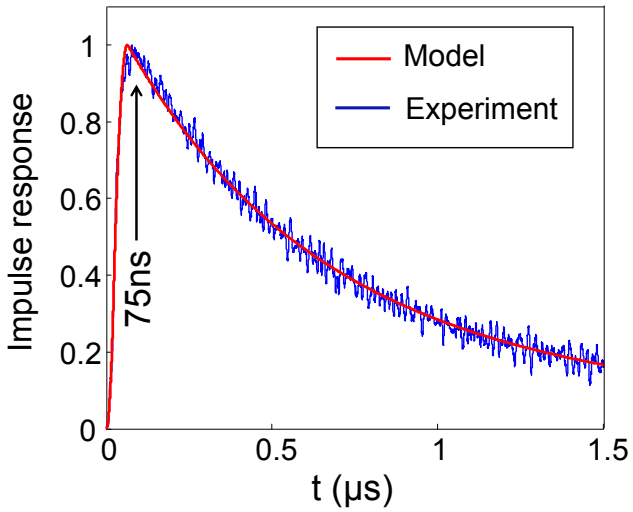

(b)

Figure 28: (a) The system-level model for the microheater-on-microdisk architecture. τ_d is the delay of the delay-like system ($h_1(t)$); and, τ_{sl} and τ_f are the slow and fast time-constants associated with the poles of the second-order system ($h_2(t)$), respectively. Also, the ratio between the slow and fast time-constants is denoted as c. (b) The model in (a) fitted to the response of the microheater to a 25 ns wide pulse (Fig. 27).

is an open-loop excitation approach and resembles the operation of a pre-distortion filter that compensates for the poles of the second-order system. By simple time/frequency domain signal operations, the response of this filter is found. The exact excitation is then derived by convolving the pulse, $p(t)$, with the filter response as

$$Excitation(t) = p(t) + \alpha p(t) * u(t) + \frac{(1-\alpha)(1-\exp(-t_p/\tau_{eff}))}{\tau_{eff}} \exp(-t/\tau_{eff}), \quad (38)$$

where t_p is the pulse-width of $p(t)$ and τ_{sl}, τ_f, and c are the parameter of the impulse model in Fig. 28(b). The first term on the right-hand side (RHS) of Eq. 38 is the high-energy pulse at the beginning of the excitation to overdrive the microheater. The second term is the

steady-state exictation and the third term is a decaying exponential. All the parameters in Eq. 38 can be found by these relations:

$$\begin{cases} \frac{1}{\tau_{eff}} = \frac{1}{c}\left(\frac{c}{\tau_f} + \frac{1}{\tau_{sl}}\right) \\ \frac{1}{\tau_T} = \frac{1}{\tau_f} + \frac{1}{\tau_{sl}} - \frac{1}{\tau_{eff}} \\ \alpha = \frac{\tau_T \tau_{eff}}{\tau_f \tau_{sl}} \end{cases} . \tag{39}$$

Using the parameters found in Eq. 39, the appropriate excitation signal can be found. The square root of the excitation signal in Eq. 38 that corresponds to the excitation voltage is shown in Fig. 29(a) for the parameters found in Eq. 37. It is seen that the voltage of the initial pulse is almost 6 times higher than the steady-state excitation voltage. By applying this excitation signal to the microheater shown in Fig. 24(a), the pulsed-excitation response in measured and shown in Fig. 29(b) (red curve). It is observed that the optical response of the system is settled in 88 ns. This response is the fastest response of a thermo-optic device reported to this date.

4.6 Power Consumption

One very important figure-of-merit in reconfigurable devices is the power consumption. As seen in Chapter 3, there is a tradeoff between power consumption and speed. Since in this work the main purpose is to improve the reconfiguration speed, power consumption is sacrificed for faster response. However, in the new microheater design, because of the very small heating volume of the device, power consumption is drastically improved. Figure 30 shows 0.33 nm red-shift of the drop response of the 5 μm diameter microdisk device shown in Fig. 25(a) for 0.24 mW power dissipation over the microdisk. This corresponds to 1.37 nm (177 GHz) change in the resonance frequency for 1 mW power dissipation. Also, this measurement was performed for the similar device with a diameter of 4 μm, and 2.5 nm (265 GHz) wavelength shift was measured for 1 mW power dissipation. This is the largest wavelength shift per milliwatt power reported to this date.

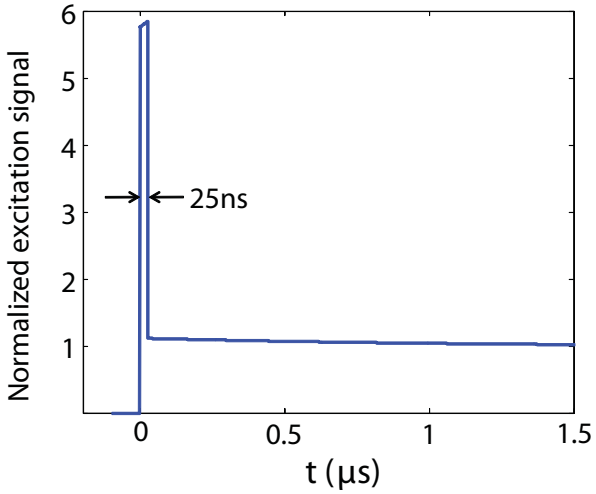

(a)

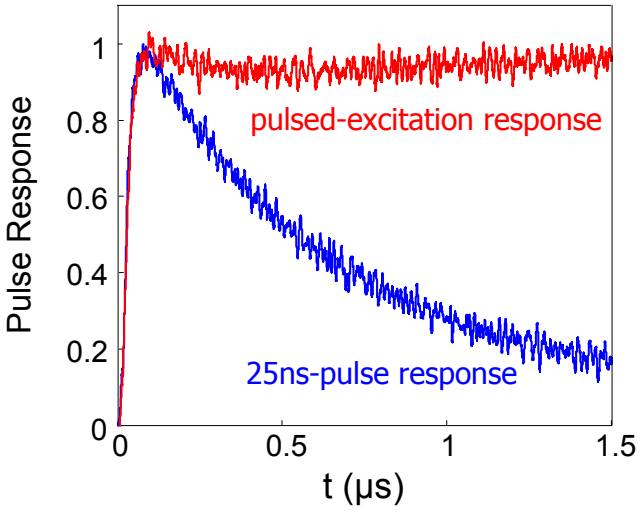

(b)

Figure 29: (a) The normalized excitation signal found for the pulsed-excitation of the microheater with normalized impulse response shown in Fig. 27 (b) The normalized response of the microheater-on-microheater device shown in Fig. 24(a) to a 25ns-pulse (blue curve) and to the excitation signal shown in (a) (red curve).

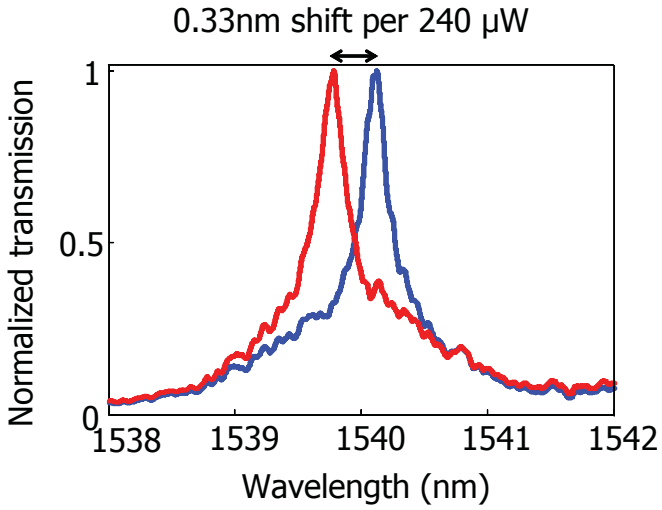

Figure 30: Transmission spectra of the drop port of the add-drop device shown in Fig. 25(a) for zero (red curve) and 240 μW (blue curve) power dissipation values in the microheater.

4.7 Differential Microheater Operation

As observed in Sections 3.5 and 4.4, the settling time of a microheater can be pushed beyond the step-response rise-time by applying a high-energy pulse at the beginning of the excitation signal. One limitations if this method is that the device cannot be cooled using a similar method. Thus, whenever cooling is needed, the reconfiguration time will be limited to a few microseconds. To tackle this problem, the microheaters can be designed in a differential architecture such that the two differential devices act in a push-pull behavior. Thus, the effect of cooling of one microheater can be emulated by heating its differential counterpart. If appropriately designed, this system can maintain its state while the two microheaters are cooling at the same time. Thus, when there is no need for reconfiguration, the two microheaters are cooled down such that the optical output of the device is maintained.

One essential reconfigurable device in many photonic circuits is a tunable coupler which is usually implemented using a Mach-Zehnder interferometer (MZI). Here, we use the developed ultrafast small microdisk phase-shifters at each arm of a MZI to form a differentially addressable coupler (Fig. 31). Metallic microheaters are directly integrated

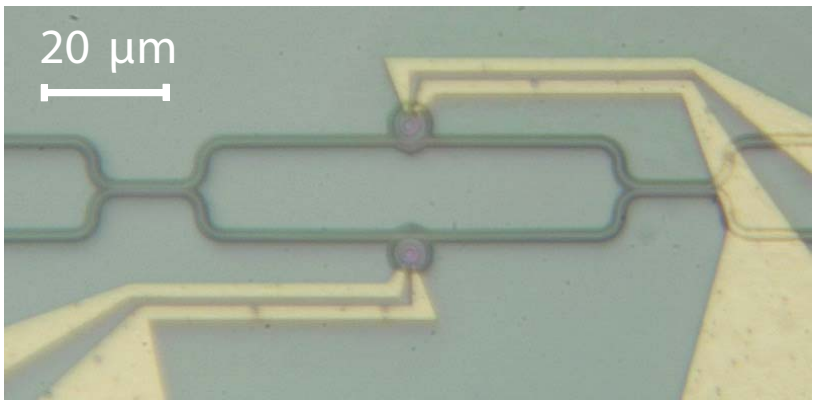

Figure 31: Optical micrograph of the differentially tunable coupler with integrated microheaters. The input and output couplers are 3dB directional couplers.

over the microdisk for fast reconfiguration. The optical micrograph of the tunable device is shown in Fig. 31. The responses of the microheaters in this device are individually tested and both had a heat propagation delay of about 75 ns. By using the model shown in Fig. 28(a) the appropriate pulsed-excitation signals (Eq. 39) for these two microheaters are found. By applying these excitation signals to these microheaters, the differential operation of this device is tested. Figure 32(a) shows the optical output of this device (lower input waveguide excited and lower output waveguide measured). At the beginning ($t < 0$) no signal is applied to either of microheaters. At $t = 0$, an excitation signal is applied to the upper microheater (H_1), and thus, the state of the optical output is changed (Fig. 32(b)). Then, at $t = 5\mu$s, an excitation signal is applied to the lower microheater (H_2) and the state of the optical output is changed in the opposite direction (Fig. 32(c)). These results show that the differential reconfiguration can be used to change the state in opposite directions very fast. Figures 32(b) and 32(c) show the response of the microheater at the rise and fall instances.

4.8 Modeling of crosstalk in small-microdisk phase-shifters

One of the very important performance measures of microheaters for large-scale photonics integration is their crosstalk with neighboring devices. This is very critical as the distance of adjacent devices becomes comparable to the heat diffusion length of the microheater. Here we compare the crosstalk performance of the heater-on-disk architecture with that

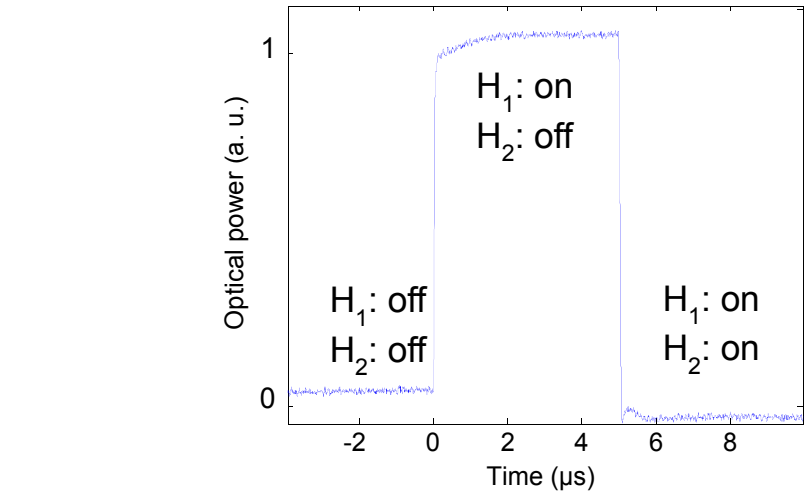

(a)

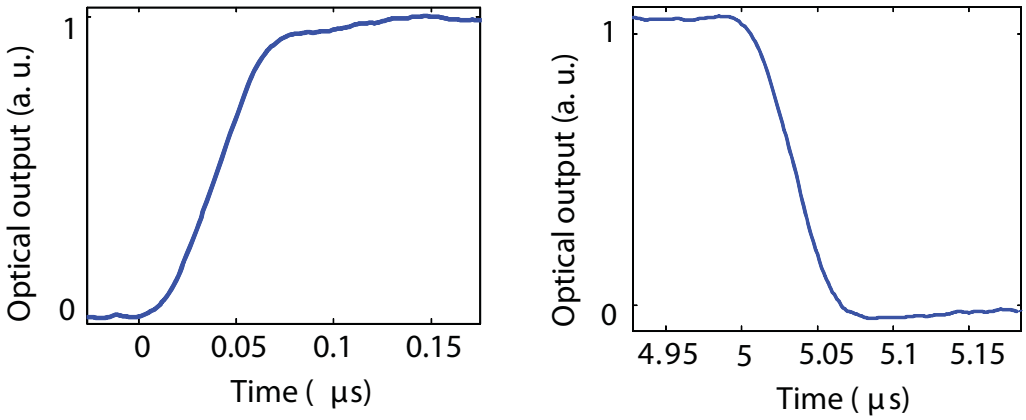

(b) (c)

Figure 32: (a) The response of the differential coupler to pulsed-excitation of the two arms. At $t = 0$ a signal is applied to the upper microheater H_1 and at $t = 5\mu$s a signal is applied to the lower microheater H_2. (b) and (c) are the responses of the differential coupler at $t = 0$ and $t = 5\mu$s.

of the more conventional heater-on-cladding. Figure 33(a) shows the temperature profile at the horizontal cross-section of two 5 μm diameter microdisks with a 50 nm gap, when the microdisk on the left is heated using a microheater directly placed on the Si layer. It is observed that as a result of the relatively large heat diffusion length ($\approx$1 μm) the adjacent microdisk is also heated. This thermal crosstalk is studied in this section.

We numerically modeled the relative shift of the resonance wavelength of the neighboring resonator ($\Delta\lambda_2$) to that of the directly heated microdisk ($\Delta\lambda_1$). This relative resonance shift quantifies the thermal crosstalk of the heater configuration and the numerical results are shown in Fig. 33(b). The blue curve shows the simulation result for the heater-on-disk configuration. The relative resonance shift is less that 10% when the distance of the resonators is more than 400 nm and this value drops below 1% for resonator gap of 3 μm. In these simulations, the thickness of the Si layer, BOX layer, and the SiO_2 caldding layer is 220 nm, 1 μm, 1 μm, respectively. The diameter of the microdisk is 5 μm, and the outer and inner diameters of the microheater are 1 μm and 0.5 μm, respectively.

We also modeled the thermal crosstalk of the heater-on-cladding configuration in which the microheater is placed on a 1 μm SiO_2 caldding over the microdisk and the result is shown by the red curve in Fig. 33(b). It is observed that the crosstalk is increased by almost a factor of two compared to the microheater-on-microdisk architecture. In this simulation, we increased the diameter of the microheater to 2 μm while keeping its width at 0.5 μm. The reason for this is that a 1 μm diameter microheater has a very high thermal resistance and as a result, the temperature of the microheater becomes much higher than the microdisk. This is not desirable as the failure rate of the resistive microheater increases with the operating temperature. In fact, increasing the microheater diameter did not considerably change the thermal crosstalk, which is counter-intuitive in the first glance. We also simulated the crosstalk for the same architecture with 3 μm thick BOX layer [1] and the result is shown by the black curve in Fig. 33(b). The crosstalk in this configuration is 30% higher at small microdisk gaps and a few times higher at microdisk gaps beyond 4 μm. Therefore, for high integration level, thin BOX layers outperform in terms of thermal

[1] This BOX layer thickness is very common in Si photonics.

crosstalk. However, this comes at the cost of higher power consumption because of lower thermal resistance of the microheater configuration.

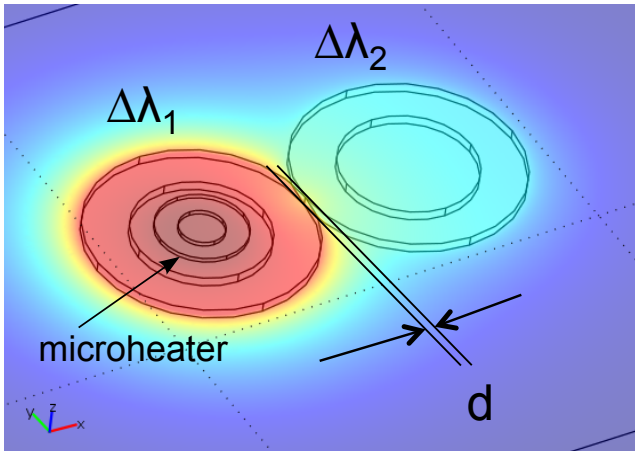

(a)

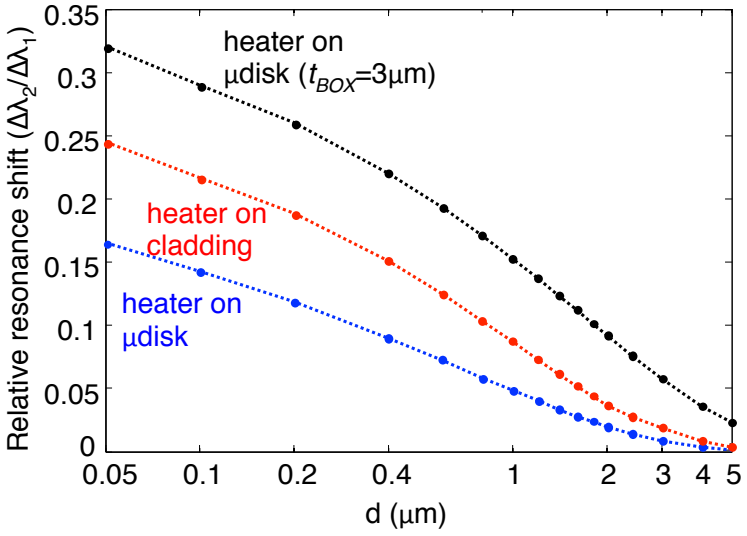

(b)

Figure 33: (a) Temperature profile at the horizontal cross-section of two 5 μm diameter microdisks with a 50 nm gap, when the microdisk on the left is heated with a microheater directly placed on the Si layer. (b) Modeling results of the relative resonance shift of two adjacent microdisks for heater-on-disk configuration (blue curve), heater-on-(1 μm)cladding configuration (red curve), and heater-on-(3 μm)cladding configuration (black curve).

CHAPTER V

NONLINEAR OPTICS IN SILICON MICRORESONATORS

5.1 Introduction

If it was not for nonlinear electrical phenomena, none of the functionalities in today's microprocessors would exist. The operation of a simple electronics switch, as the most fundamental element in digital electronics, is governed by nonlinear response of matter to the electrons and holes in the device. Similarly, response of matter to electromagnetic waves and especially optical waves is nonlinear by nature, which is unfortunately (!) much weaker than electrical nonlinearities. Therefore, it was not until the advent of high power lasers that such nonlinear phenomena were discovered.

Similar to electronics, the deployment of nonlinear processes in optics can considerably extend the capabilities of signal processing. Through the mixing of different optical waves in a nonlinear material, light generation, wavelength conversion, phase conjugation, and signal amplification and regeneration can be achieved. These functions are among the most common nonlinear optics functions with numerous applications in fiber optics and microwave-photonics. It should be noted that because of the weak nonlinear phenomena and their practical challenges, many of the nonlinear functions in today's systems are carried out using electronics with the addition of optical-to-electrical and electrical-to-optical conversion. This approach although useful in many systems, is not transparent[1] to the bandwidth of signal and is limited to the electronics bandwidth. Therefore, an all-optical solutions that can be achieved through optical nonlinearities is essential. In this chapter, we theoretically study third-order nonlinearity in Si and discuss its practical applications.

[1] A Transparent optical system is one whose operation is independent of the data bandwidth and modulation scheme. In order for a system to be transparent, its operation should be all-optical.

5.2 *Optical Nonlinearity in Silicon*

Crystalline Si belongs to the m3m point-group symmetry and therefore exhibits an inversion symmetry. The first non-zero optical nonlinearity in materials with inversion symmetry is the third-order nonlinearity which is also referred to as $\chi^{(3)}$ nonlinearity. This nonlinearity is composed of two sources, one from an electronic contribution and the other from an inelastic Raman scattering contribution rising from lattice vibrations. The electronic third-order nonlinearity is also known as Kerr effect and responds instantaneously to the incoming waves and is therefore wide-band. However, Raman Scattering is a resonant process and therefore is a narrow-band process. The advantage of Raman process in Si is that it is stronger than electronic nonlinearity and light generation has been achieved using this effect [56, 57]. On the other hand, electronic Kerr nonlinearity is wideband and therefore more appropriate for wavelength-division multiplexing and general optical signal processing applications. In this work, we focus on the electronic nonlinearity because of their more versatile application in telecommunications. Electronic Kerr nonlinearity is relatively strong in Si and is two orders of magnitude stronger than that of fused silica in optical fibers. Numerous nonlinear processes have been demonstrated in the past two decades in fiber optics systems and therefore, the comparison of different nonlinear figures-of-merit in Si with those in silica is relevant from a practical point of view.

One of the advantages of guided-wave optics is the possibility of confining light in a small cross-section and increasing its intensity, which in turn intensifies the nonlinear process. By using High-index-contrast material platforms such as Si it is possible to confine light at sub-wavelength dimensions. For example a typical Si ridge waveguide has an effective mode area [2] of $(0.75\lambda_0/n_{Si})^2$. This is more than two orders of magnitude smaller than the effective mode area of a common single-mode fiber. The combination of strong Kerr nonlinearity and high optical confinement results in four to five orders of magnitude higher effective nonlinearity in Si waveguides compared of silica fibers. This enables to

[2] Effective mode-area is a parameter defined later in this chapter.

realize nonlinear processes in Si with pump powers in the order of a few hundreds of milliwatt, which makes them powerful tools for on-chip all-optical solution. Up to this date, there has been numerous demonstrations of nonlinear optical processes in Si such as, wavelength conversion [27, 28, 58], optical regeneration [59], and signal generation [56].

In order to make nonlinear optical processes practical for a truly on-chip solution, pump power requirement should be decreased to almost a milliwatt. One approach to enhance the nonlinear effect is through the enhancement of light inside optical microresonators [3]. As explained in Section 2.2, the intensity of the incoming light can be enhanced in a resonator by $\frac{1}{\pi}\mathcal{F}$ at critical coupling (see Eq. 27), where $\mathcal{F}$ is the finesse of the resonator. With recent advancements in the fabrication of microresonators, finesse values as large as a few thousands has be achieved in Si-based devices [5, 7]. This allows us to reduce the pump power to even below one milliwatt and enable a truly integrated nonlinear solution.

In spite of the strong nonlinear interactions in Si, both linear and nonlinear losses in Si are major obstacles for an efficient nonlinear process. Rayleigh scattering loss is strong in sub-wavelength Si ridge waveguides (1-2 dB/cm in Si waveguide compared to 0.17 dB/km in silica fiber). Also, the photon energy of light at telecommunication wavelength is more than half of the bandgap of Si and therefore, two-photon absorption (TPA) is strong at this wavelength. TPA process results in free-carrier generation that will in turn introduce free carrier absorption (FCA). This is the limiting factor in third-order nonlinear processes in Si at telecommunication wavelength (λ =1.55μm) and is discussed in detail in this chapter.

5.3 Couple-Mode Theory of Four-Wave Mixing in Silicon Resonators

In this section, we develop the coupled-mode theory equations governing the four-wave mixing interaction of waves in Si microresonators. First, we define the physics behind the third-order nonlinearity in Si. Then the nonlinear polarization is treated as a perturbation

[3] In literature, both of the terms "microresonators" and "cavities" are used by different authors. "Cavity" is the more common term in the physics community and the concept of "cavity quantum-electrodynamics" is an example of such usage. On the other hand "microresonators" or "resonators" is more common in optical engineering community. In this work, since we are seeking practical optical signal processing solutions, we use the term "microresonators".

on the modes of the resonator, and through a first-order perturbation theory, temporal coupled-mode equations of the interacting waves are derived.

5.3.1 Third-order Nonlinear Polarization in Silicon

At low optical power, polarization of atoms and molecules of matter is linearly proportional to the strength of the electric field. When the force from the external electric field becomes comparable to the inter-atomic Coulomb's force, matter responds in a nonlinear fashion to the applied electric field. This can be represented through a Taylor series expansion of polarization field which contains nonlinear terms given by

$$\mathbf{P}(\mathbf{r},t) = \epsilon_0\chi^{(1)}\mathbf{E}(\mathbf{r},t) + \epsilon_0\chi^{(2)}\mathbf{E}(\mathbf{r},t)\cdot\mathbf{E}(\mathbf{r},t) + \epsilon_0\chi^{(3)}\mathbf{E}(\mathbf{r},t)\cdot\mathbf{E}(\mathbf{r},t)\cdot\mathbf{E}(\mathbf{r},t) + \dots \tag{40}$$

where the first $\chi^{(1)}$, $\chi^{(2)}$, and $\chi^{(3)}$ are the first, second, and third order susceptibility tensors, respectively. Here, the multiplications are tensor multiplication and $\chi^{(2)}$ and $\chi^{(3)}$ are of third and fourth rank. Since Si has an inversion symmetry it can be easily seen that all the even order polarization terms in Eq. (40) vanish including the $\chi^{(2)}$ term. In Eq. (40) we assumed that susceptibility tensors are independent from frequency. In reality, this is not a valid assumption and by taking the frequency dependence of susceptibility tensors, we can defined the third-order polarization in the frequency domain as

$$P_i^{(3)}(\mathbf{r},\omega_1) = \epsilon_0\chi_{ijkl}^{(3)}(\omega_1;\omega_2,\omega_3,\omega_4)E_j(\mathbf{r},\omega_2)\cdot E_k(\mathbf{r},\omega_3)\cdot E_l(\mathbf{r},\omega_4)\,, \tag{41}$$

where i, j, k, and l are different coordinate indices and Einstein notation is used in the above relation. Conservation of energy requires that $\omega_1 = \omega_2 + \omega_3 + \omega_4$. Here, $\chi^{(3)}$ is composed of the electronic and Raman contributions and is given by

$$\chi^{(3)} = \chi^{e} + \chi^{R}\,. \tag{42}$$

Raman scattering couples waves that are separated in frequency by the Raman shift, which is 15.6 THz in Si. In this work, the interacting waves are considered to fall in the fiber optics C band [4] and therefore, contribution from Raman scattering is ignored. The electronic Kerr

[4] C band covers 1530 nm to 1565 nm.

nonlinearity is anisotropic in Si [60] and is given by

$$\chi^e_{ijkl} = \chi^e_{1111}[\frac{\rho}{3}(\delta_{ij}\delta_{kl} + \delta_{ik}\delta_{jl} + \delta_{il}\delta_{jk}) + (1-\rho)\delta_{ijkl}], \tag{43}$$

where $\rho \equiv 3\chi^e_{1122}/\chi^e_{1111}$ is the nonlinear anisotropy. In Si χ^e_{1111} is measured and its real and imaginary parts determine the Kerr coefficient n_2 and TPAcoefficient β_T through

$$\frac{\omega}{c}n_2(\omega) + \frac{i}{2}\beta_T(\omega) = \frac{3\omega}{4\epsilon_0 c^2 n_0^2(\omega)}\chi^e_{1111}(\omega,\omega,-\omega,\omega), \tag{44}$$

where $n_0(\omega)$ is the refractive index of Si at ω. The values of n_2 and β_T are measured in several references [61]. In this work, we use $n_2 = 0.45 \times 10^{-13}$ cm^2/W and $\beta_T = 0.79 \times 10^{-11}$ m/W at telecommunication wavelength. The nonlinear figure-of-merit (NFOM) is defined as $F_n = n_2/\lambda\beta_T$ and is 0.36 at 1.5 μm in Si. The large value of the imaginary part of χ^e_{1111} is because of the strong TPA in Si at 1.5 μm. This effect limits the nonlinear efficiency in Si at this wavelength.

The strong TPA in Si results in the generation of electrons and holes that results in both free-carrier absorption (FCA) loss and change of index of refraction through the plasma dispersion effect [45]. This phenomenon is representable through a free-carrier susceptibility

$$\chi^f = 2n_0[n_f + ic\alpha_f/2\omega] \tag{45}$$

where n_f and α_f are given by the following empirical formulas

$$n_f(N_e,N_h) = -(8.8\times10^{-4}N_e + 8.5N_h^{0.8})\times10^{-18} \tag{46}$$

$$\alpha_f(N_e,N_h) = -(8.8N_e + 6.0N_h)\times10^{-18} \tag{47}$$

where N_e and N_h are the density of free electrons and holes in cm^{-3}, respectively. Here, $\alpha_f(N_e,N_h)$ is the propagation loss in cm^{-1}. The dynamics of free carrier density is governed by the following carrier continuity equation

$$\frac{\partial N_\nu}{\partial t} = -\frac{N_\nu}{\tau_{rec}} + G \tag{48}$$

where τ_{rec} and G are the recombination lifetime and the generation rate of free carriers. Here, subscript ν refers to either electrons or holes. In this equation, we neglected the

drift current term as it is very small in high-resistive Si. τ_{rec} is mainly determined through carrier recombination at the surface states of the Si device and varies from a few hundreds of picoseconds in sub-micron ridge waveguides to tens of nanosecond in rib waveguides with smaller surface-to-volume ratio. G is determined through the TPA rate and is given by

$$G = \frac{\beta_T I^2}{2\hbar\omega} \tag{49}$$

where $I = \frac{1}{2}\epsilon_0 n_0 c|E|^2$ is the intensity of the optical wave.

5.3.2 Coupled-Mode Theory of Four-Wave Mixing

The third-order nonlinear term in Eq. (41) results in the mixing of incoming signals at different frequencies and the generation of polarization field at new frequencies. These polarization fields will in turn result in the radiation of electric fields at these new frequencies. Now, assume that the two CW sources with frequencies ω_s and ω_p propagate in the nonlinear medium. Here, subscripts "p" and "s" refer to pump and signal. Mixing of signals results in the generation of $3\omega_s$, $3\omega_p$, $2\omega_s \pm \omega_p$, and $2\omega_p \pm \omega_s$. These new frequencies mix together and with the original waves and generate new frequencies and this process goes on forever. However, in practice there is a certain condition (phase-matching condition) needed for these new frequencies to prevail. Here, we are interested in the two generated waves that lie close to the original waves, i.e. $2\omega_s - \omega_p$, and $2\omega_p - \omega_s$. Figure 34 shows the schematic of the generation of the $2\omega_p - \omega_s$ wave defined as ω_i. In this picture, two pump photons give out their energy and one signal and one idler photons are generated. This process is know as four-wave mixing (FWM), and is used extensively for the generation of new optical waves and wavelength conversion. These type of processes in which the conservation of energy is satisfied among the interacting optical waves is known as a parametric process. In this work, we consider that the energy of pump is much larger than that of signal and therefore, the generation of $2\omega_s - \omega_p$ wave is much weaker than the generation of $2\omega_p - \omega_s$ wave and only the latter wave is considered in the derivation of coupled-mode theory.

Consider a TWR in Si such as the one studied in Sections 2.1.2 and 2.2. Figure 35 shows

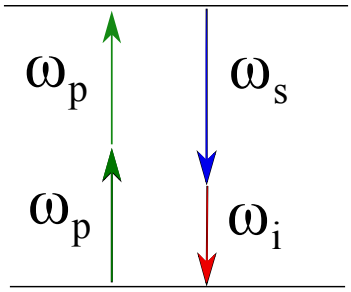

Figure 34: Schematic of the parametric FWM process in which two pump photons give their energy to one signal and one idler photons. Conservation of energy is satisfied in this process through the interacting photons.

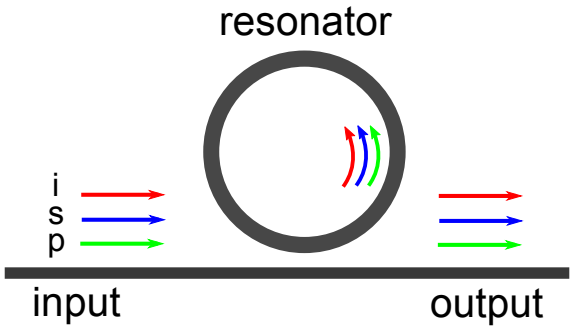

Figure 35: Schematic of a TWR that is used in a FWM process. The incoming wave is composed of three different frequencies pump, signal and idler represented through green, blue, and red arrows, respectively. In this picture, the incoming waves are coupled into the resonator where FWM takes place.

the schematic of this resonator with three input waves, pump, signal and idler, coupled into this resonator. If the frequencies of these waves satisfy conservation of energy as the one depicted in Fig. 34 and are also in resonance with the resonator, FWM takes place inside the resonator [5]. Here, we develop the CMT for this FWM process in a TWR in Si. The field of this resonator can be expanded on the basis of its modes at the excited frequencies as

$$\mathbf{E}(\mathbf{r},\omega) = \sum_{\nu=i,s,p} A_\nu(\omega)\mathbf{E}_\nu(\mathbf{r},\omega), \tag{50}$$

where $\mathbf{E}_\nu(\mathbf{r},\omega)$ is the eigenmodes of the resonator. Wave equation for this field is given by

$$\nabla^2\mathbf{E}(\mathbf{r},\omega) + \frac{\omega^2}{c^2}\epsilon_r(\mathbf{r},\omega)\mathbf{E}(\mathbf{r},\omega) = -\mu_0\omega^2\mathbf{P}^{NL}(\mathbf{r},\omega), \tag{51}$$

where $\mathbf{P}^{NL} = \mathbf{P}^{(3)} + \mathbf{P}^f$, where $\mathbf{P}^{(3)}$ and $\mathbf{P}^f$ are given by the susceptibility tensors in Eqs.

[5] We explain further in this chapter that phase-matching is automatically satisfied in TWRs

(41) and (45). By substituting (50) in (51) and multiplying the both side of the equation by $\mathbf{E}^*_{\nu'}$ and integrating over the volume of the resonator, applying the orthogonality of modes [6], and converting the equation to time-domain [7] we obtain

$$\frac{d^2A_\nu}{dt^2} + \omega_{0\nu}^2 A_\nu = \frac{\frac{d^2}{dt^2}\int d\mathbf{r}\mathbf{E}^*_\nu(\mathbf{r},\omega_{0\nu})\mathbf{P}(\mathbf{r},t)}{\epsilon_0\int d\mathbf{r}\epsilon_r(\mathbf{r},\omega_{0\nu})|\mathbf{E}(\mathbf{r},\omega_{0\nu})|^2}. \tag{52}$$

If we assume that the optical field is narrowband and close to a single resonance, field amplitudes and polarization vectors can be considered as $A_\nu(t) = A'_\nu(t)e^{-i\omega_{0\nu}t}$ and $\mathbf{P}(t) = \mathbf{P}'(t)e^{-i\omega_{0\nu}t}$. Considering this time-domain dependence and assuming slowly-varying amplitude approximation, i.e., $\frac{d^2}{dt^2}A' = 0$, Eq.(52) is transformed to

$$\frac{dA_\nu}{dt} = i(\omega_{0\nu} - \omega_\nu)A_\nu - \frac{A_\nu}{\tau_{t\nu}} + \frac{i\omega_\nu}{2\epsilon_0}\frac{\int d\mathbf{r}\mathbf{E}^*_\nu(\mathbf{r},\omega_{0\nu})\mathbf{P}(\mathbf{r},t)}{\int d\mathbf{r}\epsilon_r(\mathbf{r},\omega_{0\nu})|\mathbf{E}(\mathbf{r},\omega_{0\nu})|^2}, \tag{53}$$

where we have dropped the prime sign from A'. In the derivation of the above formula we have assumed an imaginary resonance frequency to account for the linear loss. This loss is represented by the photon lifetime in the resonator $\tau_{t\nu}$, which is related to the resonator Q factor through $\tau_{t\nu} = Q_{t\nu}/\omega_{0\nu}$.

The polarization integral in Eq. (53) consists of a third-order nonlinearity polarization and a free-carrier polarization. The third-order polarization integral consists of the mixing of the p, s, and i terms through the $\chi^{(3)}$ tensor given in Eq. (43). This tensor couples the third-order product of different electric field components to the nonlinear polarization. Considering the exact form of $\chi^{(3)}$ does not allow us to derive a simple form of CMT of FWM. However, if we assume that most of the energy of the electric field is along one of the transverse directions, i.e. x or y, (considering the direction of propagation along z) the vector nature of the field can be ignored and a single $\chi^{(3)}$ coefficient can be considered for all of the mixing terms in Eq. (41). It should be noted that the $\chi^{(3)}$ value in the x and y direction varies by 14%; therefore, this simplification of the problem does not introduce a large error in the final result. Using this approximation and combining Eqs. (41), (43), and

[6] Mode orthogonality used here are: 1) $\int \epsilon_r \mathbf{E}_\nu \cdot \mathbf{E}^*_{\nu'} = \int \nabla^2\mathbf{E}_\nu \cdot \mathbf{E}^*_{\nu'} = 0$ for $\nu \neq \nu'$ and 2) $\int \nabla^2\mathbf{E}_\nu \cdot \mathbf{E}^*_\nu = \frac{\omega_\nu^2}{c^2}\int \epsilon_r|\mathbf{E}_\nu|^2$

[7] By replacing $j\omega$ with $\frac{d}{dt}$

(50), third-order polarization vector is given by

$$P^{(3)}(\mathbf{r},t) = \frac{3}{4}\epsilon_0 \sum_{jkl} \chi^{(3)}_{ijkl} A_j(t) A_k^*(t) A_l(t) e^{-i(\omega_j - \omega_k + \omega_l)} E_j(\mathbf{r},\omega_{0j}) E_k^*(\mathbf{r},\omega_{0k}) E_l(\mathbf{r},\omega_{0l}), \quad (54)$$

where the electric fields are treated scalar and $\chi^{(3)}_{ijkl} = \chi^{(3)}(-\omega_i;\omega_j,-\omega_k,\omega_l)$. As explained earlier we have assumed a single $\chi^{(3)}$ coefficient and we also ignore its frequency dependence as the dispersion of $\chi^{(3)}$ is small in the bandwidth of interest. Also, through Eq. (45) we define the free-carrier polarization as

$$P^f(\mathbf{r},t) = \epsilon \sum_j \chi^f[\omega_j, N(\mathbf{r},t)] A_j(t) e^{-i\omega_j t} E_j(\mathbf{r},t). \quad (55)$$

Using Eqs. (54) and (55) we calculate the polarization integral in (53) and the dynamic equation of the field amplitude is derived as

$$\frac{dA_i}{dt} = i(\omega_i - \omega_{i0})A_i - \frac{A_i}{2\tau_{ti}} + \frac{i\omega_i}{2n_{0i}^2}\chi^f(\omega_i,\overline{N}_i)A_i + i\sum_{jkl}\gamma_{ijkl}A_jA_k^*A_l, \quad (56)$$

where we replaced the subscript ν with i. Here, $n_{0\nu}$ is the refractive index of Si at ω_ν, $\overline{N}_\nu$ is the field-average free carrier density, γ_{ijkl} is the nonlinear parameter, and the field amplitudes are normalized such that $|A_\nu|^2 = U_\nu$ is the energy of the field in the resonator. The third term in Eq. (56) represents both the nonlinear frequency shift and loss caused by the free carriers. Here, we assume that χ^f is a linear function of free carrier density and the field-averaged free carrier density is given by

$$\overline{N}_\nu(t) = \frac{\int_{Si} d\mathbf{r} N(\mathbf{r},t)\epsilon_r(\mathbf{r},\omega_{0\nu})|\mathbf{E}(\mathbf{r},\omega_{0\nu})|^2}{\int d\mathbf{r}\epsilon_r(\mathbf{r},\omega_{0\nu})|\mathbf{E}(\mathbf{r},\omega_{0\nu})|^2}. \quad (57)$$

The nonlinear parameter γ_{ijkl} in Eq. (56) is also given by

$$\gamma_{ijkl} = \frac{3\omega_i\eta_{ijkl}\chi^{(3)}(-\omega_i;\omega_j,-\omega_k,\omega_l)}{4\epsilon_0 n_{0i}n_{0j}n_{0k}n_{0l}\overline{V}_{ijkl}} \quad (58)$$

where $\overline{V}_{ijkl} \equiv (V_iV_jV_kV_l)^{1/4}$ is the average mode volume of the resonator with V_ν being the mode volume at ω_ν, and

$$\eta_{ijkl} = \frac{\int_{Si} d\mathbf{r}(\epsilon_{ri}\epsilon_{rj}\epsilon_{rk}\epsilon_{rl})^{1/2}E_i^*E_jE_k^*E_l}{\{\prod_{\nu=i,j,k,l}\int_{Si} d\mathbf{r}\epsilon_{r\nu}^2|E_\nu|^4\}^{1/4}}. \quad (59)$$

V_ν is given by

$$V_\nu \equiv \frac{\{\int d\mathbf{r}\epsilon_r(\mathbf{r},\omega_{0\nu})|\mathbf{E}(\mathbf{r},\omega_{0\nu})|^2\}^2}{\int\limits_{Si} d\mathbf{r}\epsilon_r^2(\mathbf{r},\omega_{0\nu})|\mathbf{E}(\mathbf{r},\omega_{0\nu})|^4} \tag{60}$$

and the subscript Si denotes that the integration is only over the Si region. In order to find $\overline{N}$, we take the field-average of Eq. (48) and the free-carrier dynamics is given by

$$\frac{\partial \overline{N}_\nu}{\partial t} = -\frac{\overline{N}_\nu}{\tau_{rec}} + \overline{G}. \tag{61}$$

By taking the field-average of Eq. (49) and assuming that only the pump wave contributes to TPA we arrive at

$$\overline{G}_p(t) \equiv \frac{c^2\beta_T U_p^2}{2\hbar\omega_p n_{0p}^2(\overline{V}^f)^2} \tag{62}$$

where U_p is the pump energy, and effective mode volume related to TPA-induced free-carrier effect is

$$V_\nu^f \equiv \{\frac{[\int d\mathbf{r}\epsilon_r(\mathbf{r},\omega_{0\nu})|\mathbf{E}(\mathbf{r},\omega_{0\nu})|^2]^3}{\int\limits_{Si} d\mathbf{r}\epsilon_r^3(\mathbf{r},\omega_{0\nu})|\mathbf{E}(\mathbf{r},\omega_{0\nu})|^6}\}^{1/2}. \tag{63}$$

In deriving Eq. (62) we have ignored the field mismatch between the pump, signal and idler waves. This is a good approximation since the field-profile dispersion is very small in the frequency range of interest.

Rewriting Eq. (56) for pump, signal, and idler waves we arrive at the following coupled-mode equations for FWM in a resonator with TPA and FCA

$$\begin{aligned}\frac{dA_p}{dt} &= i\Delta\omega_p A_p - \frac{A_p}{2\tau_{tp}} + \frac{i\omega_p n_p^f}{n_{0p}}A_p + i(\gamma_p U_p + 2\gamma_{ps}U_s + 2\gamma_{pi}U_i)A_p \\ &\quad + 2i\gamma_{pspi}A_sA_iA_p^* + \frac{iA_p^{in}}{\sqrt{\tau_{ep}}},\end{aligned} \tag{64}$$

$$\begin{aligned}\frac{dA_s}{dt} &= i\Delta\omega_s A_s - \frac{A_s}{2\tau_{ts}} + \frac{i\omega_s n_s^f}{n_{0s}}A_s + i(\gamma_s U_s + 2\gamma_{sp}U_p + 2\gamma_{si}U_i)A_s \\ &\quad + i\gamma_{spip}A_p^2A_i^* + \frac{iA_s^{in}}{\sqrt{\tau_{es}}},\end{aligned} \tag{65}$$

$$\begin{aligned}\frac{dA_i}{dt} &= i\Delta\omega_i A_i - \frac{A_i}{2\tau_{ti}} + \frac{i\omega_i n_i^f}{n_{0i}}A_i + i(\gamma_i U_i + 2\gamma_{ip}U_p + 2\gamma_{is}U_s)A_i \\ &\quad + i\gamma_{ipsp}A_p^2A_s^* + \frac{iA_i^{in}}{\sqrt{\tau_{ei}}},\end{aligned} \tag{66}$$

where $\Delta\omega_\nu = (\omega_\nu - \omega_{\nu 0})$, $U_\nu = |A_\nu|^2$ is the wave energy in the resonator, and $n_\nu^f = n_{f\nu} + ic\alpha_{f\nu}/(2\omega_\nu)$ is the free carrier refractive index and loss term. We have also added a source term represented by $\frac{A_\nu^{in}}{\sqrt{\tau_{e\nu}}}$, where $|A_\nu^{in}|^2$ is the power of the wave in the input waveguide and $\tau_{e\nu}$ is the photon lifetime through the coupling to the external waveguide. Also, we simplified the nonlinear coefficients as $\gamma_v \equiv \gamma_{vvvv}$ and $\gamma_{uv} \equiv \gamma_{uvvu}$.

In Eqs. (64)-(66) the fourth term on the RHS is self-phase modulation (SPF), the fifth and sixth terms are cross-phase modulation (XPF), and the seventh term represents FWM. The imaginary part of γ corresponds to TPA and results in a source of loss in Eqs. (64)-(66). The real part of γ in the SPM and XPM terms results in a shift in the resonance frequency of the resonator. This is the source of the nonlinear contribution to the resonance frequency mismatch that is discussed in the next section.

5.3.3 Dispersion and Phase-Matching Condition

5.3.3.1 Phase-Matching Condition in Waveguides

In the context of FWM and in general in nonlinear parametric processes in waveguides and in bulk material, it is well-known that the phase-matching condition of the interacting waves is required in order to have an efficient nonlinear process. Phase matching is usually satisfied through the engineering of the dispersion properties of the waveguide. When studying parametric processes in resonators, the phase-matching condition is usually automatically satisfied. However, resonator dispersion should still be engineered to have the resonator modes exactly at the frequencies of the interacting waves. We will discuss this effect in this section. However, it is instructive to first examine the phase-matching condition in FWM in a waveguide.

The nonlinear coupled-mode equations for waveguides are very similar to those of resonators presented in the previous section; the difference being that the dynamics of the amplitude of waves is treated in space instead of time. It is easily shown (see Ref. [62])

that the coupled-mode equation for the pump wave in a waveguide is given by

$$\frac{dA_p}{dz} = -\frac{\alpha}{2}A_p + \frac{i\omega_p n_p^f}{c}A_p + i(\gamma_p|A_p|^2 + 2\gamma_{ps}|A_s|^2 + 2\gamma_{pi}|A_i|^2)A_p + 2i\gamma_{pspi}A_sA_iA_p^* exp(-i\Delta k_{linear}z)\,, \tag{67}$$

where the nonlinear coefficients γ are redefined for the waveguide and $\Delta k_{linear} = 2k_p - k_i - k_s$ with k_ν being the propagation constant at ω_ν. It can be shown that for the non-depleting pump approximation [8] pump wave is given by

$$A_p = P_p exp(i\gamma P_p z) \tag{68}$$

where P_p is the pump power and we have ignored the loss and free-carrier terms in Eq. (67). Replacing Eq. (68) in the coupled-mode equation for signal and idler waves we arrive at

$$\frac{dA_s}{dz} = i2\gamma P_p A_s + 2i\gamma A_i^* P_p exp(-i\Delta kz)\,, \tag{69}$$

$$\frac{dA_i^*}{dz} = -i2\gamma P_p A_i^* - 2i\gamma A_s P_p exp(i\Delta kz)\,, \tag{70}$$

where the loss and free carrier terms are ignored and $\Delta k = \Delta k_{linear} - 2\gamma P_p$ is the nonlinear phase mismatch. Following the same procedure as in Ref. [62] we arrive at the gain coefficient

$$g = \sqrt{(\gamma P_p)^2 - (\Delta k/2)^2}\,. \tag{71}$$

Gain maximum ($g_{max} = \gamma P_p$) occurs for

$$\Delta k = \Delta k_{linear} - 2\gamma P_p = 0\,. \tag{72}$$

This is know as the **phase-matching condition** for FWM. At low pump power the nonlinear term in the phase-matching condition (second term on the RHS) can be ignored. The linear term in the phase-matching condition requires that the momentum of the interacting waves to be conserves in the FWM process [9]. From a classical point of view, phase-matching condition requires that the signal field generated by the nonlinear polarization

[8] The non-depleting pump approximation is valid when the pump power is much higher than the signal and idler power and this condition remains valid throughout the length of the nonlinear process.

[9] Momentum of photon is $\mathbf{p} = \hbar\mathbf{k}$.

(with phase term $exp(i(2k_p - k_i)z)$) be in phase with signal propagating in the waveguide (with phase term $exp(ik_s z)$). This requires that $\Delta k_{linear} = 0$. The presence of the nonlinear term in Eq. (72) originates from the change of the propagation constant of the interacting waves induced by the SPM of pump and XPM of pump on signal and idler. The linear part of phase-matching condition is given by the dispersion properties of the waveguide by

$$\Delta k_{linear} = -\beta_2(\Delta\omega)^2 - \frac{1}{12}\beta_4(\Delta\omega)^4 \tag{73}$$

where $\beta_2 = d^2k/d\omega^2$ and $\beta_4 = d^4k/d\omega^4$ are the second-order and fourth-order group-velocity dispersion (GVD) of the waveguide, and $\Delta\omega$ is the angular frequency difference of the pump with signal/idler waves. Usually β_4 can be ignored when β_2 is nonzero and $\Delta\omega$ is small. Thus, from Eq. (72) the second-order GVD has to be slightly negative (i.e., in the anomalous dispersion regime) to compensate for the nonlinear term in the phase-matching condition. This is the dispersion criterion that is most commonly used for the design of waveguides for FWM applications.

Throughout this work, we use ridge waveguides on SOI platform with SiO_2 cladding. The typical width and height of single-mode ridge waveguides is around 250 nm and 500 nm, respectively. Figures 36(a) and 36(b) show the GVD of the TE mode of Si ridge waveguide with different widths and with the height of 200 nm and 250 nm, respectively. The dispersion of waveguides are calculated using the RF-module of Comsol software. The dashed line shows the GVD of the bulk Si [63]. Material dispersion properties are provided in Appendix B. The inset in 36(a) schematically shows the cross-section of the ridge waveguide considered in these simulations. The dispersion parameter D shown in these figures is common in fiber optics and is related to β_2 through

$$D = -\frac{2\pi c}{\lambda^2}\beta_2\,. \tag{74}$$

It is seen that the dispersion of bulk Si is normal (i.e. $D < 0$). Because of the high field confinement effect in ridge waveguides, dispersion is shifted to the anomalous dispersion regime. This is in favor for the phase-matching condition as explained above. We have also plotted GVD for a 450 nm wide Si waveguide with different heights in Fig. 37. A height range of 250 nm to 300 nm gives a anomalous dispersion of around 1000 ps/nm.km. We

keep the waveguide width below 450 nm for single-mode waveguide operation. We also studied the dispersion properties of the TM mode of Si waveguides. For height below 300 nm, waveguides exhibit a normal dispersion. Figure 38 shows the GVD of the TM mode of a 300 nm high waveguide for different widths. It is observed that the GVD characteristic of TM mode is different from that of the TE mode. At waveguide width around 500 nm, Si waveguides exhibit an anomalous dispersion which could be useful for FWM application.

5.3.3.2 Effect of Dispersion in Resonators

With the introduction to phase-matching condition in waveguides in the previous section, we proceed to the effect of dispersion on the efficiency of FWM process in resonators, which is the subject of interest in this work. Examining the coupled-mode equations for a resonator, we realize that the propagation phase of interacting waves is embedded in the field-overlap coefficient η in Eq. (59). The field profile of a TWR can be written as

$$\mathbf{E}(\mathbf{r}_T,\rho) = \mathbf{E}_T(\mathbf{r}_T)exp(-i\phi(\rho)), \tag{75}$$

where $\mathbf{r}_T = (r,z)$ and ρ are the transverse and longitudinal (to the direction of traveling wave) coordinate vectors. In the wavelength range of interest the transverse component of the resonance field does not have significant frequency dependence and therefore, we can approximate η in Eq. (59) by

$$\eta_{ijkl} = \frac{1}{L_R}\oint exp[-i(\phi_i(\rho) - \phi_j(\rho) + \phi_k(\rho) - \phi_l(\rho))]d\rho, \tag{76}$$

where L_R is the length of the resonator and the integral is taken over the length of the resonator. For a simple TWR, $\phi(\rho) = \beta\rho$ and it can be easily shown that if pump azimuthal mode number is exactly in the center of the signal and idler mode numbers, we have $\eta = 1$. This is exactly the well-known fact that the linear phase-matching condition in a TWR is automatically satisfied (i.e., $2\beta_p - \beta_s - \beta_i = 0$). From the quantum point-of-view the conservation of the linear momentum in waveguides is transformed into the conservation of angular momentum in TWR, which is automatically satisfied.

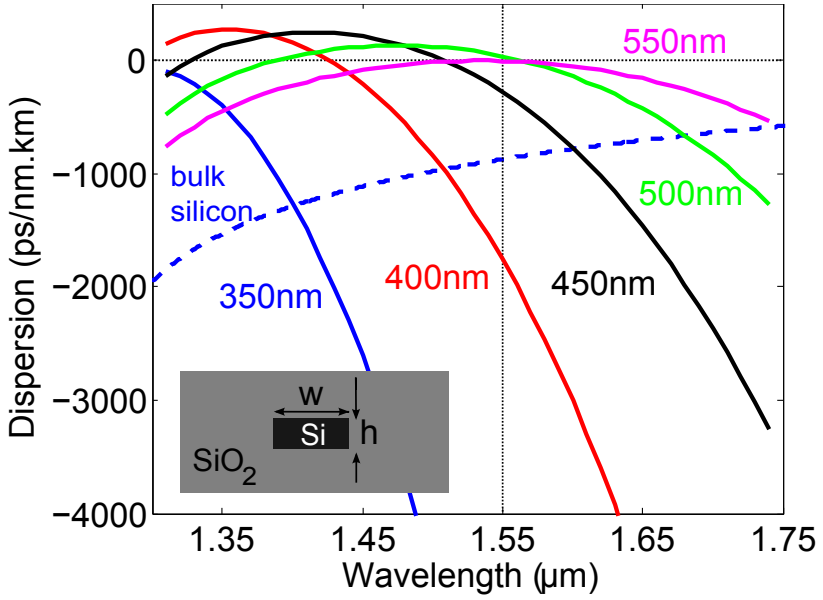

(a)

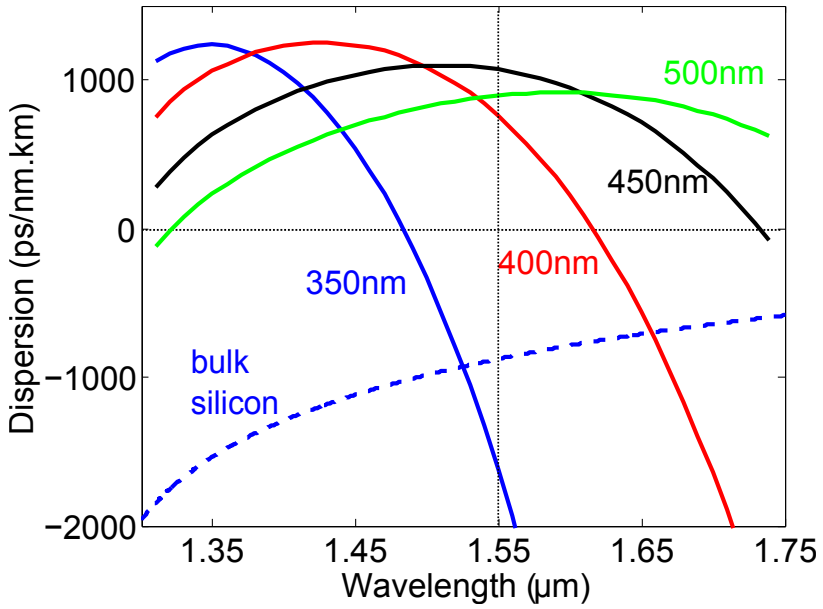

(b)

Figure 36: (a) and (b) show the GVD of Si ridge waveguides for the TE polarization for different widths for heights of 200 nm and 250 nm, respectively. The number next to each curve represents the width of the waveguide. The dashed line shows the GVD of bulk Si. The inset in (a) schematically shows the cross-section of the ridge waveguide considered in these simulations.

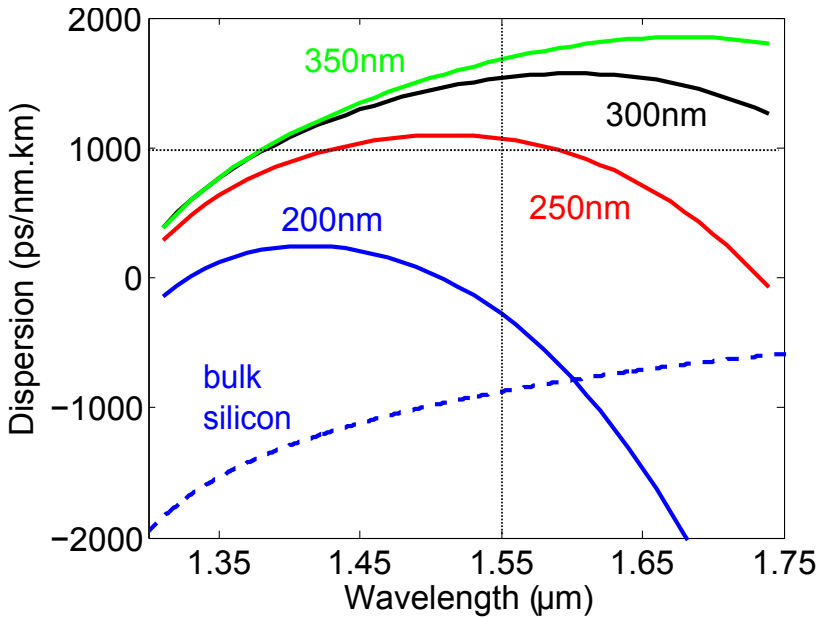

Figure 37: GVD of 450 nm wide Si ridge waveguides for the TE polarization for different heights. The number next to each curve represents the height of the waveguide. The dashed line shows the GVD of bulk Si.

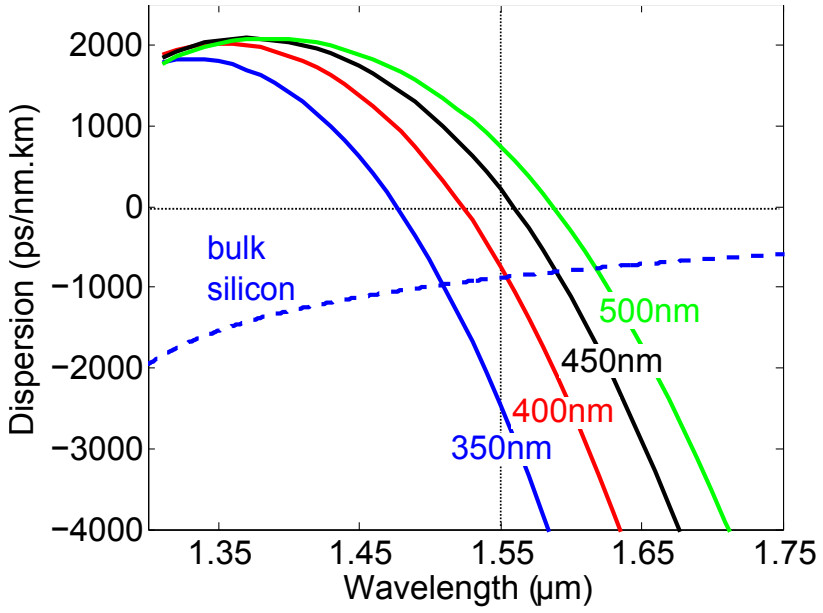

Figure 38: GVD of 300 nm high Si ridge waveguides for the TM polarization for different widths. The number next to each curve represents the width of the waveguide. The dashed line shows the GVD of bulk Si.

Although dispersion engineering is not required for phase-matching condition in resonators, the dispersion of the traveling wave manifests itself in the mismatch of the resonance frequencies with the frequencies of the interacting waves. The first term in Eqs. (64)-(66), $(i\Delta\omega_\nu)$, represents the detuning of the wave from the resonance frequency of the corresponding mode. More accurately, if we consider the effects of SPM and XPM of pump, the frequency detuning is given by $\Delta\omega_\nu = \omega_\nu - (\omega_{\nu 0} - q\gamma_{\nu p}U_p)$ [10] where $q = 1$ for $\nu = p$ and $q = 2$ for $\nu = s, i$. To have the maximum enhancement of interacting waves in the resonator, all of these waves should be at resonance, i.e., $\Delta\omega_\nu = 0$, and we arrive at the following condition for TWRs

$$\Delta\Omega = \Delta\Omega_{linear} + 2\gamma U_p = 0\,, \tag{77}$$

where $\Delta\Omega$ is defined as the **resonance frequency mismatch** in which

$$\Delta\Omega_{linear} = 2\omega_{p0} - \omega_{s0} + \omega_{i0}\,. \tag{78}$$

In a TWR, it can be easily seen that

$$\Delta\Omega_{linear} = v_g\beta_2(\Delta\omega)^2\,, \tag{79}$$

where v_g and β_2 are the group velocity and GVD of the traveling wave in the resonator and $\Delta\omega$ is the frequency spacing of pump and signal/idler waves. It is seen that as in waveguides, at low pump power, zero GVD is required to satisfy efficient FWM process. However, at high pump power the contributions from SPM and XPM of pump requires anomalous dispersion in the TWR.

As seen in this section, the dispersion of the resonator plays and important role in the frequency detuning of the resonator from the interacting waves. As the enhancement line-shape of the TWR is Lorentzian, frequency mismatch larger than the linewidth of the

[10] Here, we ignored the contribution of the free carriers on the resonance frequency shift, which is almost identical for pump, signal and idler. In reality, there is another physical effect that we have ignored in these relations, being the self-heating of the resonator as result of absorption both through TPA and FCA effects. In practice, the overall effect of free carrier and thermal resonance shifts can be compensated by for example adjusting the temperature of the substrate using a thermo-electric cooler (TEC). It has been shown before that the interplay between the free-carrier and thermal resonance shift can result in the modulation of the resonance wavelength, which might complicate the practical application of these devices [64]. Here, we ignore both these effects as they are almost identical for the resonance modes of interests.

resonance can cause significant loss in the enhancement of light and the resulting FWM process. In the next chapter, we employ the coupled-mode equations (64)-(66) to derive the efficiency of the FWM process

5.4 Wavelength Conversion in Si TWRs

One of the very useful applications of FWM is wavelength conversion, which is widely utilized in fiber optic networks. There are several methods for implementing FWM wavelength conversion [65]. In this work, we employ the most conventional approach in which a CW pump is used to convert the information of signal to idler wave. In this process, two photons of pump give out their energy and one signal and one idler photons are generated. Through this process, the information of the signal photon is transferred into the idler photon. Wavelength conversion efficiency (WCE) is defined as

$$\eta_{WC} = \frac{P_{idler}^{out}}{P_{signal}^{in}}, \tag{80}$$

where P_{idler}^{out} and P_{signal}^{in} are the output power of the idler and the input power of the signal waves, respectively. In this work, we assume that $P_{idler}^{in} = 0$ and $P_{signal}^{in} \ll P_{pump}^{in}$ (non-depleting pump approximation). Using this excitations condition, we theoretically solve for η_{WC} by integrating the coupled-mode equations (64)-(66).

TPA and FCA loss and the SPM/XPM-induced frequency mismatch are the limiting factors in the FWM process. Thus, we first simulate the level of loss and frequency mismatch as a function of circulating power in the resonator. Throughout this chapter, we consider a ring resonator with a cross-section of 450×220 nm^2. All of the parameters of the resonator used in the simulation of FWM are summarized in Table 4. We assume that pump, signal, and idler are critically coupled to the input waveguide at low power (i.e., ignoring losses due to TPA and FCA). Figure 39(a) shows the degradation of the Q of the resonator indued by TPA and FCA versus the circulating power in the resonator. Solid black curve shows the Q caused by the TPA (i.e., Q_{TPA}) and the red lines (solid, dashed, and dotted) show the Q caused by FCA (i.e., Q_{FCA}) for different values of free-carrier lifetime in the device. We have also plotted the Q caused by both of these nonlinear effects (i.e., Q_{NL}). Blue, green and orange curves show Q_{NL} for free carrier lifetimes of 1 ns, 0.1 ns

and 10 ps, respectively. It is observed for the typical free-carrier recombination lifetime of 1 ns, [11] Q_{NL} drops to 10^5 for 0.1 W circulating power in the resonator. As it will be seen in this chapter this amount of power is not enough to provide practical conversion efficiency and the recombination lifetime has to be lowered by active removal of free carriers (see Ref. [66]).

Table 4: Material and resonator parameters

microring width	w	450 nm
microring height	h	230 nm
microring radius	r	20 μm
microring effective index	n_{eff}	2.35
microring group index	n_g	4.25
microring GVD	D	2000 ps/km.nm
Kerr coefficient of Si [61]	n_2	0.45×10^{-13} cm^2/W
TPA coefficient of Si [61]	β_T	0.79 cm/GW
Effective mode area	$A_{eff} = V_{eff}/L_r$	0.114 μm^2
Effective free-carrier mode area	$A^f_{eff} = V^f_{eff}/L_r$	0.103 μm^2

Figure 39(b) shows the nonlinear frequency mismatch, $\frac{1}{2\pi}\gamma U_p$, versus the circulating power in the resonator. It is seen that for circulating power of 1 W, nonlinear frequency mismatch is around 5 GHz which is more than the typical linewidth of a Si resonator ($\delta f_{FWHM} \approx 2\ GHZ$ for a $Q = 10^5$). This indicates that the nonlinear source of frequency mismatch cannot be ignored at high power levels. We show in the next section that through a novel quasi-phase matching (QPM) method in resonators, frequency mismatch can be compensated. Therefore, nonlinear loss mechanism in Si resonators is the only source limiting the conversion efficiency.

By integrating the coupled-mode equations of FWM in time we can numerically numerically solve for the evolution of pump, signal and idler. Figure 40 shows the evolution of pump enegry in the resonator and signal and idler output power in a 20μm diameter resonator with D=2000 ps/nm.km and $\tau_{rec} = 1\ ns$. Blue, red, and black curves show

[11] Free carrier recombination lifetime is on the order of 0.5 ns to 1 ns for high confinement Si waveguides. Recombination lifetime increases as the width of the resonator cross-section is increased. It has been shown that through active removal of free carriers by incorporating a PN-junction, free carrier lifetime can be reduced down to 12.2 ps [66].

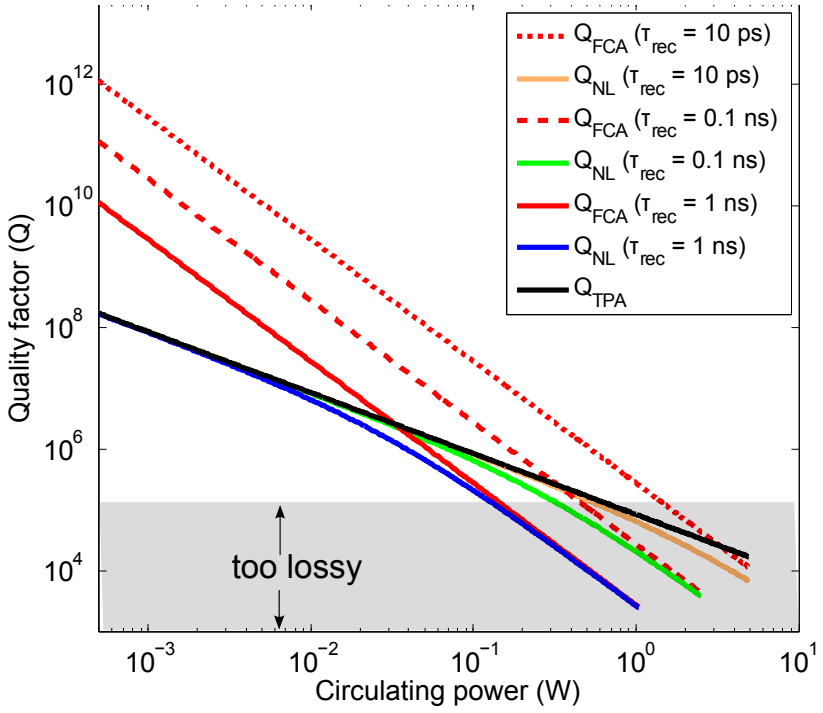

(a)

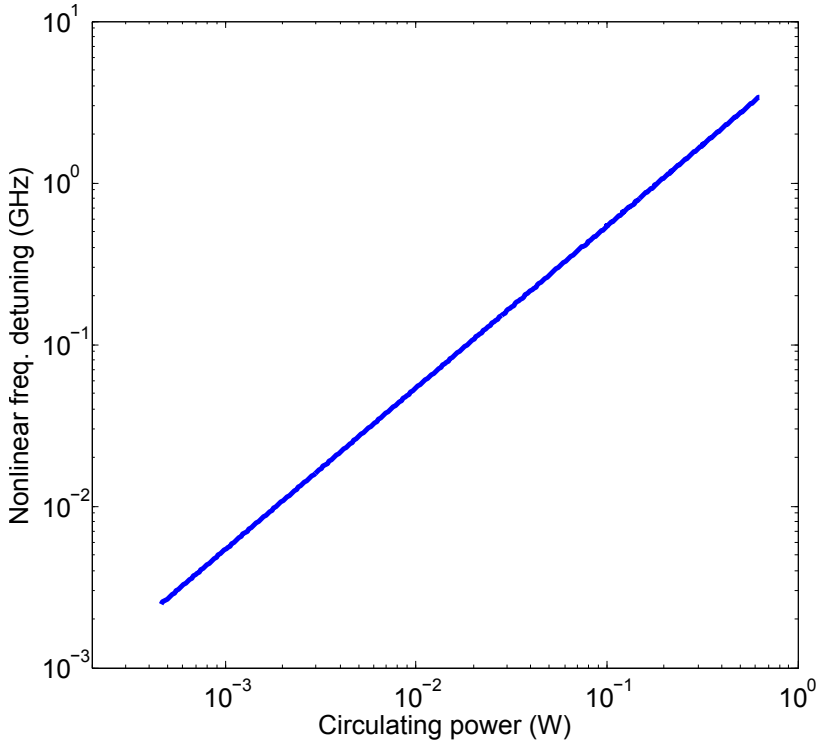

(b)

Figure 39: (a) shows the degradation in the Q of a resonator caused by nonlinear loss sources, i.e. TPA, and FCA. Solid black curve shows the Q caused by the TPA, Q_{TPA}, and the solid, dashed, and dotted red lines show the Q caused by FCA, Q_{FCA}, for free-carrier lifetimes of 1 ns, 0.1 ns and 10 ps, respectively. Blue, green and orange curves show the total nonlinear Q, Q_{NL}, for free-carrier lifetimes of 1 ns, 0.1 ns and 10 ps, respectively. (b) shows the nonlinear frequency mismatch, $\frac{1}{2\pi}\gamma U_p$, versus the circulating power in the resonator.

the result of time integration of FWM coupled-mode equations for input pump power of 1 mW, 5 mW, and 10 mW, respectively. In these simulation the input power of signal and idler is 4 μW and 0, respectively. It is observed that as the input pump power is increased from 1 mW to 5 mW, there is an increase in the pump energy stored in the resonator and also the output idler power. However, as the input pump power is further increased to 10 mW, the output idler power is decreased. This is the result of the degradation of the Q of the resonator because of the increased nonlinear loss and also nonlinear frequency mismatch. Therefore, we expect that there would be an optimum pump power for wavelength conversion in Si microresonators.

Using the same time integration of FWM coupled-mode equations, we derive WCE for the input pump power P_{in}^{p}= 4 mW (corresponding to $\approx$ 0.2 pJ pump energy in the resonator or 0.1 W circulating pump power) versus pump-signal frequency difference. The results are shown in Fig. 41 for different values of GVD. In these simulations, we assume that both the signal and pump waves are in resonance with the resonator and any frequency mismatch caused by GVD of the resonator results in the detuning of idler frequency from its corresponding resonance mode. It is seen that the conversion efficiency is considerably decreased as the pump-signal wavelength difference is increased. This is because of the increase in frequency mismatch (see Eq. 79) and the decrease in the enhancement of the idler wave in the resonator. The dashed blue curve shows the conversion efficiency in the presence of QPM as is discussed in the next section.

Now we study the effect of input pump power on WCE. Figure 42(a) shows the WCE for a 40μm diameter ring resonator with a GVD of D=2000 ps/nm.km vs. input pump power. WCE is calculated for the signal-pump frequency difference of 5, 10, 15, 20, and 25 FSRs of the resonator (FSR is $\approx$ 4.5nm). In this simulations, free-carrier lifetime is 1 ns. It is observed that WCE is saturated at pump power of approximately 5mW. The reason for this behaviour is that for τ_{rec}= 1ns, Q of the resonator degrades to approximately 10^5 for a few milliwatts of input pump power, as observed in Fig. 39(a). Further increase in the pump power increases the nonlinear loss and reduces the enhancement in the resonator. Also, we observe that as the pump-signal frequency difference increases, WCE drops significantly.

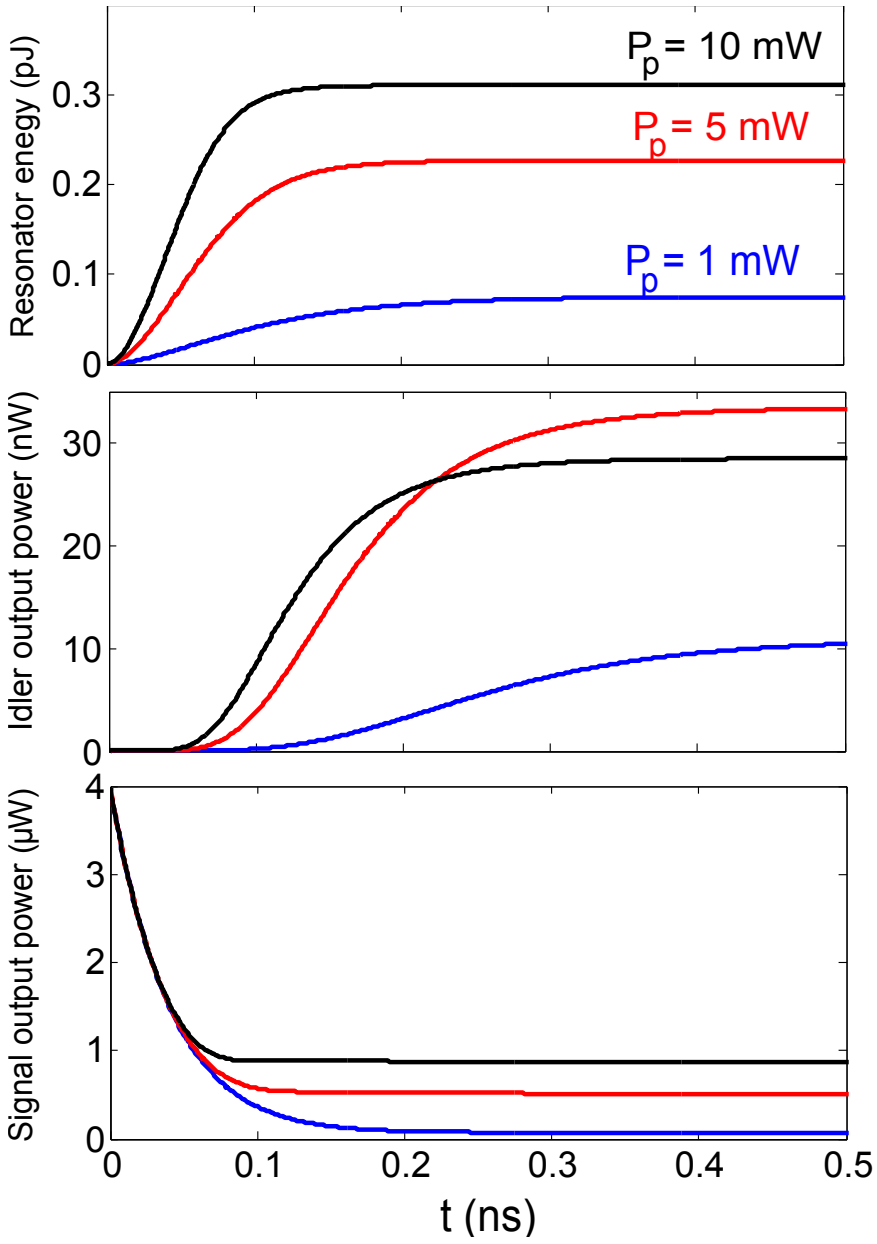

Figure 40: Evolution of pump enegry in the resonator and signal and idler output power in a 40μm diamter resonator with D=2000 ps/nm.km. Blue, red, and black curves show the result of time integration of FWM coupled-mode equations for input pump power of 1 mW, 5 mW, and 10 mW, respectively. In these simulation the input power of signal and idler are 4μW and 0, respectively.

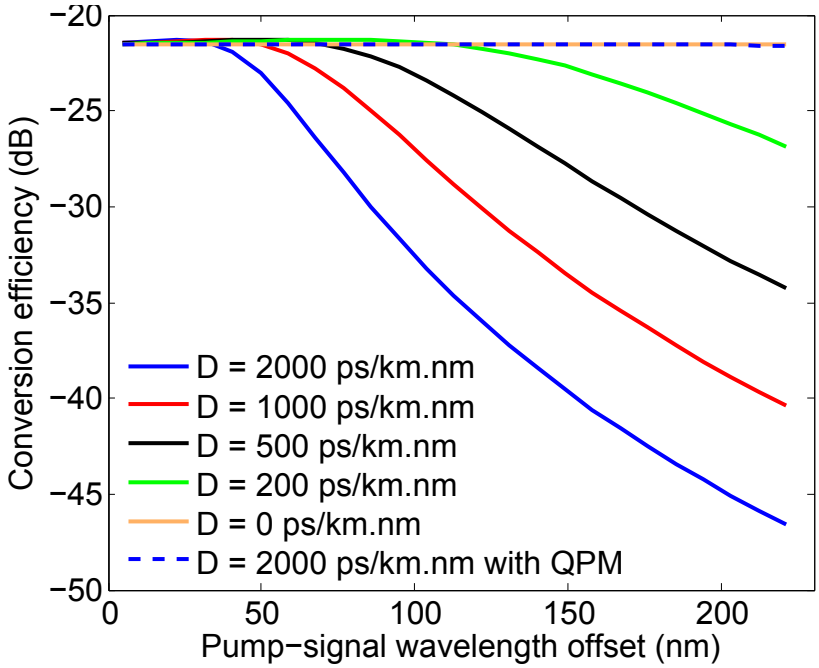

Figure 41: WCE versus pump-signal frequency difference for different values of GVD. In these simulations P_{in}^{p} = 4 mW. The dashed line shows the conversion efficiency for D = 2000 ps/nm.km with QPM.

The effect of free-carrier lifetime on WCE is also studied and the results are shown in Fig. 42(b). In this simulations, GVD of the resonator is D=2000 ps/nm.km and the pump-signal frequency difference is equal to one FSR (≈4.5 nm). As expected, by reducing free-carrier recombination lifetime the density of free carriers and consequently the nonlinear loss is reduced, resulting the increase of WCR. By reducing free-carrier lifetime from 1 ns to 10 ps, WCE can be increased by one order of magnitude. We explain in the next section that at τ_{rec} <10 ps, nonlinear frequency mismatch is a major obstacle in achieving higher WCEs. We introduce the theory of QPM in optical resonators to alleviate the challenge of frequency mismatch (both linear and nonlinear) to achieve higher conversion efficiencies.

5.5 Theory of Quasi-Phase Matching in Optical Resonators

From the very early days of nonlinear optics, satisfying the phase-matching condition in parametric nonlinear processes such as FWM, two-wave mixing, second-harmonic generation, and third-harmonic generation has been a major challenge. Quasi-phase matching

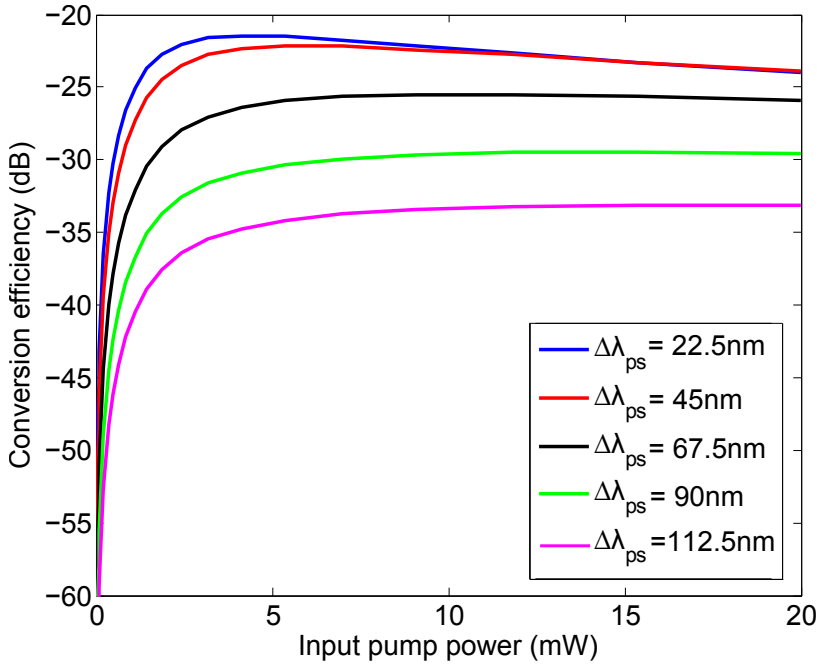

(a)

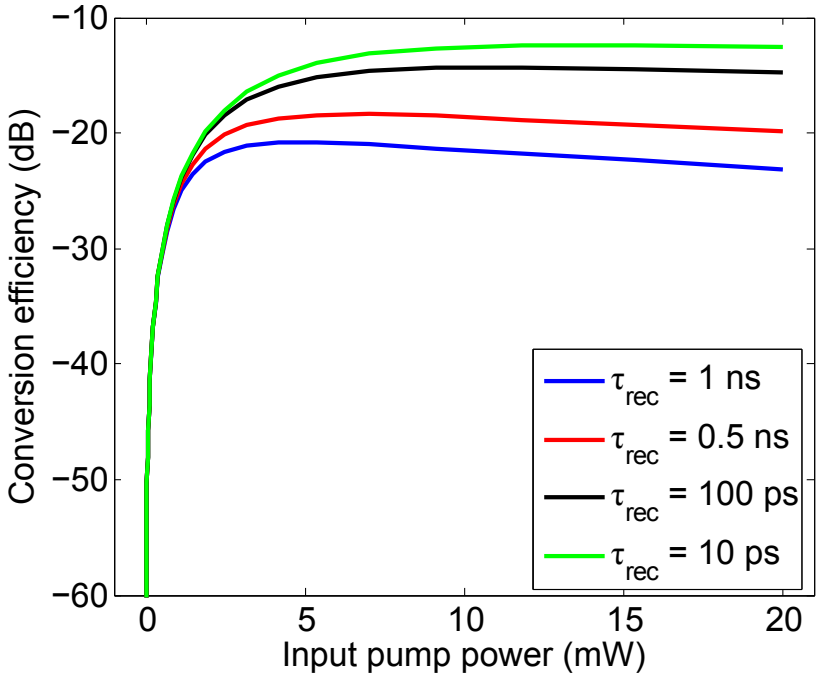

(b)

Figure 42: (a) shows the WCE for a ring resonator with a GVD of D=2000 ps/nm.km vs. input pump power. (b) shows the WCE for a ring resonator with a GVD of D=2000 ps/nm.km vs. input pump power for the pump-signal frequency difference of one FSR ($\approx$ 4.5 nm). WCE is calculated for different values of free-carrier lifetime.

(QPM) was introduced in early 1960s to alleviate this challenge [67]-[68]. In this methodology, the phase of interacting waves is corrected for at periodic locations in the direction of propagation. Usually this is achieved through the inversion of the nonlinear coefficient through changing the orientation of the material (for example in $LiNbO_3$). This method has not yet been demonstrated in Si waveguides because the sign of the $\chi^{(3)}$ coefficient does not change sign upon inversion of the crystal orientation. However, it is still possible to correct for the phases of interacting waves using phase-shifters.

Figure 43(a) shows the schematic representation of a QPM solution in Si waveguides. Here, the phases of the interacting waves are corrected using phase-shifters (Φ), periodically placed along the propagation direction. The period is a multiple (n) of the correlation length of FWM defined by

$$L_c = \frac{1}{\pi}\Delta k, \tag{81}$$

where Δk is defined in Eq. (72). Correlation length is the length within which the propagating idler wave and the $\chi^{(3)}$ polarization wave at the idler frequency become out of phase (accumulate π phase difference). In other words, after propagating the correlation length, the idler wave will combine destructively with the idler generated through the FWM. In this QPM scheme, phase-shifter (Φ) should apply the right amount of phase to compensate for the out-of-phase propagation of the idler wave that is caused by the dispersion of the waveguide. This approach can very nicely be adapted in resonators as shown in Fig. 43(b). By making a loop of one period of the waveguide shown in Fig. 43(a) a resonator can be formed with a phase-shifter in its round-trip. The waves traveling through the resonator see the phase-shifter once in every round-trip and therefore, their phases are adjusted according to the FWM phase-matching condition.

In another picture, the phase-shifter will change the resonance condition of the resonator in such a way that the resonance frequencies of the modes associated with the interacting waves satisfy the phase-matching condition of (77). This is achieved by sacrificing the momentum conservation condition, as the wave-vectors of the interacting waves are no longer given by the resonance condition of a simple TWR (i.e., $k_\nu L_R = 2\pi m_\nu$). This manifests itself through η in Eq. (59) that is no longer unity.

In order to quantify the performance of this QPM approach we consider a simple scenario. We assume that phase-shifter (Φ) introduces a phase-shift of ϕ_{v0} for pump, signal, and idler modes. Thus, the round-trip phase of the resonator is given by

$$\phi_v(\rho) = \begin{cases} k_v\rho & 0 \le \rho < L_R/2 \\ k_v\rho + \phi_{v0} & L_R/2 \le \rho < L_R \end{cases} \tag{82}$$

where $v = p,s,i$ and k_v is the propagation constant and L_R is the resonator length. The resonance condition requires $\phi_v(L_R) = 2\pi m_v$ and therefore we arrive at

$$k_v = \frac{2\pi m_v - \phi_{v0}}{L_R}. \tag{83}$$

Replacing k_v from Eq. (83) in (82), and using the result for the resonator round-trip phase, η_{pspi} in Eq. (59) is found to be

$$\eta_{pspi} = sinc(\frac{\Delta\phi_0}{2}) = sinc(\frac{\Delta k L_R}{2}) \tag{84}$$

where $\Delta\phi_0 = 2\phi_{p0} - \phi_{s0} - \phi_{i0}$ and Δk is given by Eq. (72). In the absence of the nonlinear contribution to the phase matching condition, η is given by

$$\eta_{pspi} = sinc(\frac{\beta_2(\Delta\omega)^2 L_R}{2}) \tag{85}$$

where β_2 is the second-order GVD of the resonator and $\Delta\omega$ is the frequency difference of the pump and signal/idler waves. Eqs (84) and (85) show that the FWM gain will be degraded by the value of η_{pspi} as a result of QPM.

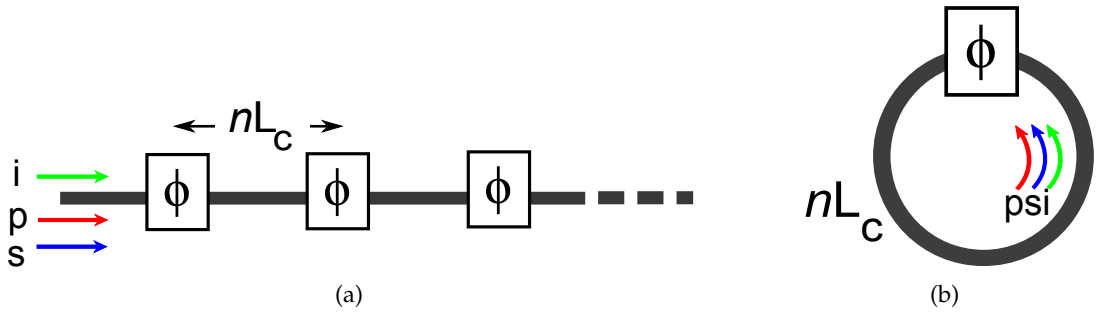

Figure 43: (a) and (b) show the schematic representation of the proposed QPM in Si waveguides and resonators, respectively. Here, L_c is the FWM correlation length.

Here, we numerically solve for the WCE by considering the QPM scenario introduced in this section. Figure 44 shows the WCE with QPM for GVD of D=2000 ps/nm.km,

τ_{rec}=1 ns for different microring resonator radii. In these simulations, $P_p^{in} = 4$ mW for r= 20μm and the input pump power is adjusted for other microring radii such that the circulating power is the same for all resonator cases. Since the input pump power is not too high, we have only considered the QPM for the linear contribution to the phase-matching condition. It is observed that for almost 200 nm pump-signal frequency offset (wavelength conversion over 400 nm) there is less than 3 dB loss in WCE for all microring radii studied. This observation shows that the performance of the QPM does not degrade for wavelength conversion at least over 400 nm. Also, looking at the performance of FWM without QPM in Fig. 42(a) (compare solid line with the dashed line), we observe that there is almost 25 dB improvement using QPM for wavelength conversion over 400 nm. Another feature observed in Fig. 44 is that WCE drops considerably for wavelength conversion over 400 nm in large TWRs. We even observe that for r=80μm, the first null of the *sinc* function in Eq. (85) is reached at around 400 nm of pump-signal wavelength offset.

As explained in Section 5.4, the nonlinear frequency mismatch in Si resonators in the limiting factor in wavelength conversion efficiency. Here, we numerically study the performance of the proposed QPM for compensating the nonlinear frequency mismatch. Figure 45 shows WCE for a microring resonator of radius 20 μm, GVD of D=2000 ps/nm.km, wavelength conversion over 90 nm, and for different values of free carrier recombination lifetimes (τ_{rec}) of 1 ns, 0.1 ns, and 10 ps. The solid and dashed curves show WCE with and without QPM. It is observed that for τ_{rec} of 1 ns and 0.1 ns there is not much improvement of WCE using QPM. This is because at these values of τ_{rec}, the limiting factor is the nonlinear loss. However, as the value of τ_{rec} is reduced to 10 ps, nonlinear frequency mismatch becomes the limiting factor, and the effect of QPM is significant on wavelength conversion. It is observed that for an input pump power of 100 mW there is 17 dB improvement in WCE using the proposed QPM. These simulations show the possibility of positive WCE in Si for the first time.

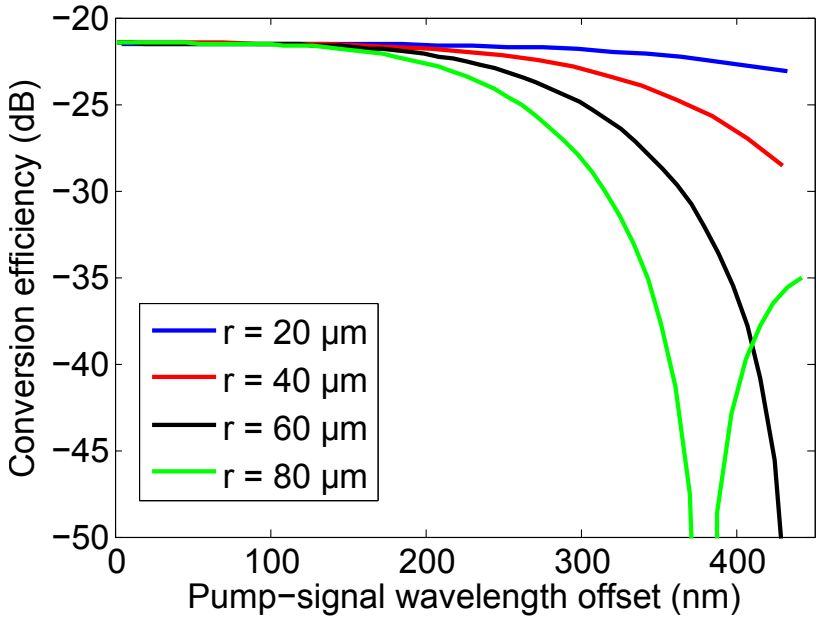

Figure 44: WCE with QPM for GVD of D=2000 ps/nm.km, τ_{rec}=1 ns for different microring resonator radii. In these simulations, $P_p^{in} = 4$ mW for r= 20μm and the amount of input pump power for other microring radii is adjusted such that the circulating power in the resonator is the same for all studied cases.

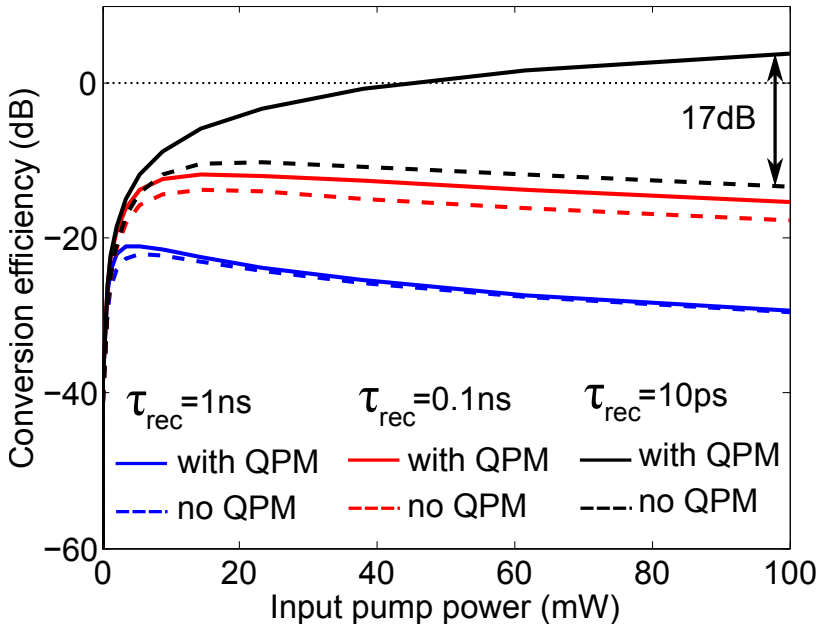

Figure 45: WCE for a microring resonator of radius 20 μm, GVD of D=2000 ps/nm.km, wavelength conversion over 90 nm. Blue, red and black curves show simulation results for free-carrier recombination lifetimes (τ_{rec}) of 1 ns, 0.1 ns, and 10 ps, respectively. The solid and dashed curves show WCE with and without QPM.

5.5.1 Implementation of QPM in Silicon Microresonators

In previous section, we observed the improvements in FWM nonlinear process using QPM. Now, the question is that what is the practical means for the implementation of the proposed QPM idea. We can think of the phase-sifter in Fig. 43(a) as a simple tunable resonator that is coupled to the original resonator as shown in Fig. 46. This device has to be carefully designed to guarantee that the appropriate phases are applied to the interacting waves.

Another device that can be used for QPM is the two-point coupled-resonator structure that is presented in Chapter 6 (also shown in Fig. 47(b)). It is shown that through the tuning of the coupling strength between the two resonators in this device, the frequency spacing of the resonance modes can be adjusted. In order to understand the performance of this device in the context of QPM presented in this section, we unloop the bottom resonator and the resulting device is shown in Fig. 47(a). This device is a simple tunable phase-shifter that is used in different applications, specially in optical signal processing. Basically, by tuning the upper arm of the Mach-Zehnder (MZ) interferometer in the coupled region of this device we can tune the phase induced by the resonator. By looping the bus waveguide the device shown in Fig. 47(b) is formed. This device is studied in Chap. 6 in detail.

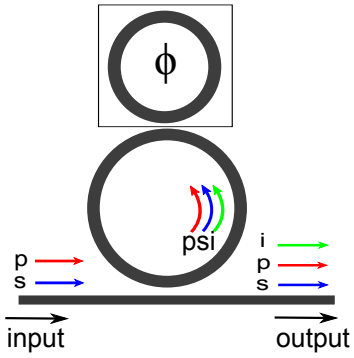

Figure 46: Schematic of a QPMed microring resonator with a microring phase-shifter.

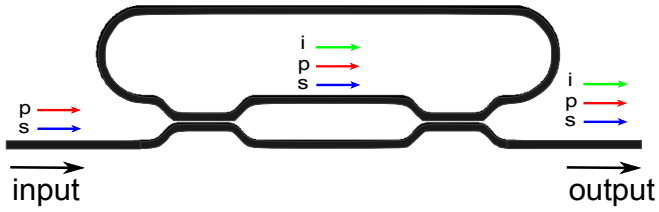

(a)

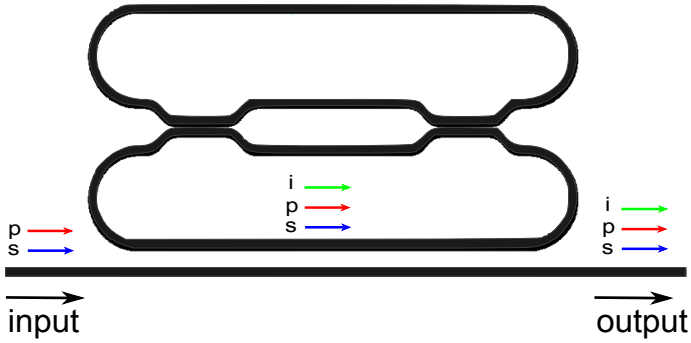

(b)

Figure 47: (a) is the schematic of a tunable phase-shifter used for QPM of the pump/signal/idler waves. (b) is the schematic of a resonator device with a tunable phase-shifter (as the one shown in (a)) in its round-trip. This device can be considered as a coupled-resonator with a Mach-Zehnder interferometer coupling the two devices.

CHAPTER VI

TUNING OF RESONANCE-SPACING IN MICRORESONATORS

In Chapter 5, we discussed the application of microresonators for nonlinear optics processes. The exact matching of the resonance frequencies with the frequencies of the interacting waves is essential for an efficient FWM in Si microresonator. In this chapter, we implement a resonator device in which the frequency spacing of its adjacent resonance modes can be tuned dynamically using the microheaters developed in Chapter 3. We demonstrate this device for a FWM application and show the possibility of fine-tuning of the frequency mismatch condition explained in detail in Chap. 5.

6.1 Introduction

Up to this date, most reconfigurable devices are envisioned for linear optical signal processing applications (e.g., filtering), where just one resonance mode is of interest. However, for many nonlinear optics and sensing applications, more than one wave with different frequencies may interact. To maximize the interaction of optical waves at different frequencies inside the resonator, it is essential to engineer the resonance condition at different free-spectral-ranges (FSRs), to allow the simultaneous resonance for all interacting waves. However, one of the challenges of resonance-based devices is the fixed resonance frequency spacing (or FSR) of their adjacent resonance modes which cannot be easily tuned. In many nonlinear and sensing applications, the resonance spacing is required to be trimmed after fabrication or to be dynamically tuned for higher performance [58]. The tuning of FSR has been demonstrated before in fiber-based devices [69, 70]; however, there has not been any work on the tuning of the frequency spacing of adjacent resonant modes in an integrated platform. Here, we propose and experimentally demonstrate a traveling-wave resonator (TWR) structure in Si photonics platform, in which the spacing of adjacent resonance modes can be tuned dynamically. To the best of our knowledge, this

is the first demonstrating of frequency-spacing tuning in an integrated platform.

6.2 Device Proposal and Simulation Results

The FSR of TWRs is given by λ^2 / Ln_g, where λ is the resonance wavelength, L is the optical length of resonator, and n_g is the group index sensed by the traveling wave. Since in conventional microring, microdisk, or racetrack TWRs, n_g cannot be tuned in a wide range, FSR of these resonators is almost fixed. This very fundamental property of resonators calls for an indirect approach for the tuning of the spacing of adjacent resonant modes. In this work, we exploit the mode-splitting properties of a strongly coupled TWR device to achieve dynamic tuning of the spacing of resonant modes.

Figure 48(a) shows the structure of two identical TWRs coupled together through a general reflection-less directional coupler (DC) with power coupling coefficient κ^2. Based on the coupled-mode theory [49], it is expected that the resonance frequency of the individual resonators to split into even and odd coupled modes (or supermodes) upon coupling. The mode with lower (higher) resonance frequency is denoted as even (odd) throughout this work. This splitting can be comparable to the FSR of resonators for high enough level of coupling. Figures 48(b) and 48(c) show the two coupled-resonator structures of our interest in which coupling is achieved using one and two symmetric DCs, respectively. The power coupling coefficient of all DCs in both structures are κ^2. The structures in Figures 48(b) and 48(c) are called single-point-coupled and two-point-coupled resonator structures, respectively. Figure 48(d) shows the amount of resonance-frequency splitting normalized to the FSR of each single resonator versus the power coupling coefficient of DCs (i.e., κ^2). Appendix A.1 contains the details of the derivation of resonance condition for both devices. These simulations are performed for two identical silicon-on-insulator (SOI) coupled racetrack resonators composed of waveguides with effective refractive index and group index of 2.5 and 4.25, respectively.

It is observed that for the single-point-coupled (48(b)) and two-point-coupled (48(c)) resonator structures, frequency splitting of up to half of an FSR and one whole FSR are achieved, respectively. To elucidate more, the transmission spectra of these coupled-resonator

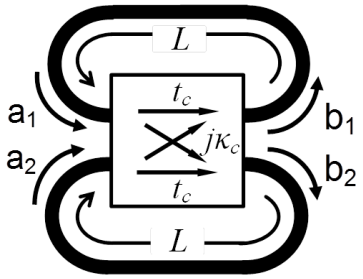

(a)

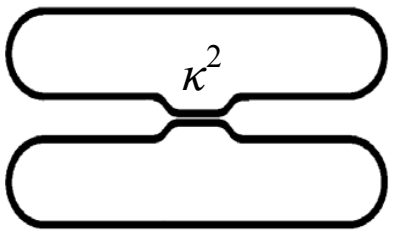

(b)

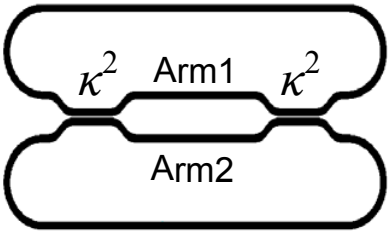

(c)

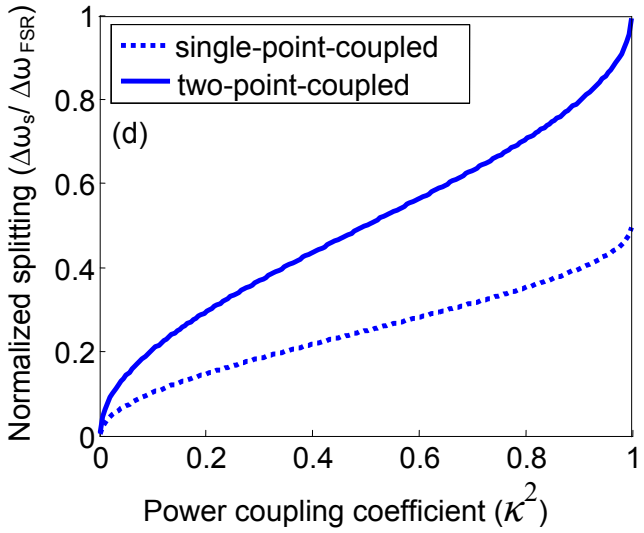

(d)

Figure 48: (a) Structure of two identical TWRs coupled together through a general coupler. (b) and (c) show the structures of two TWRs coupled together through one and two symmetric DCs, respectively. (d) The normalized frequency splitting of the structures shown in (b) and (c) vs. power coupling coefficient.

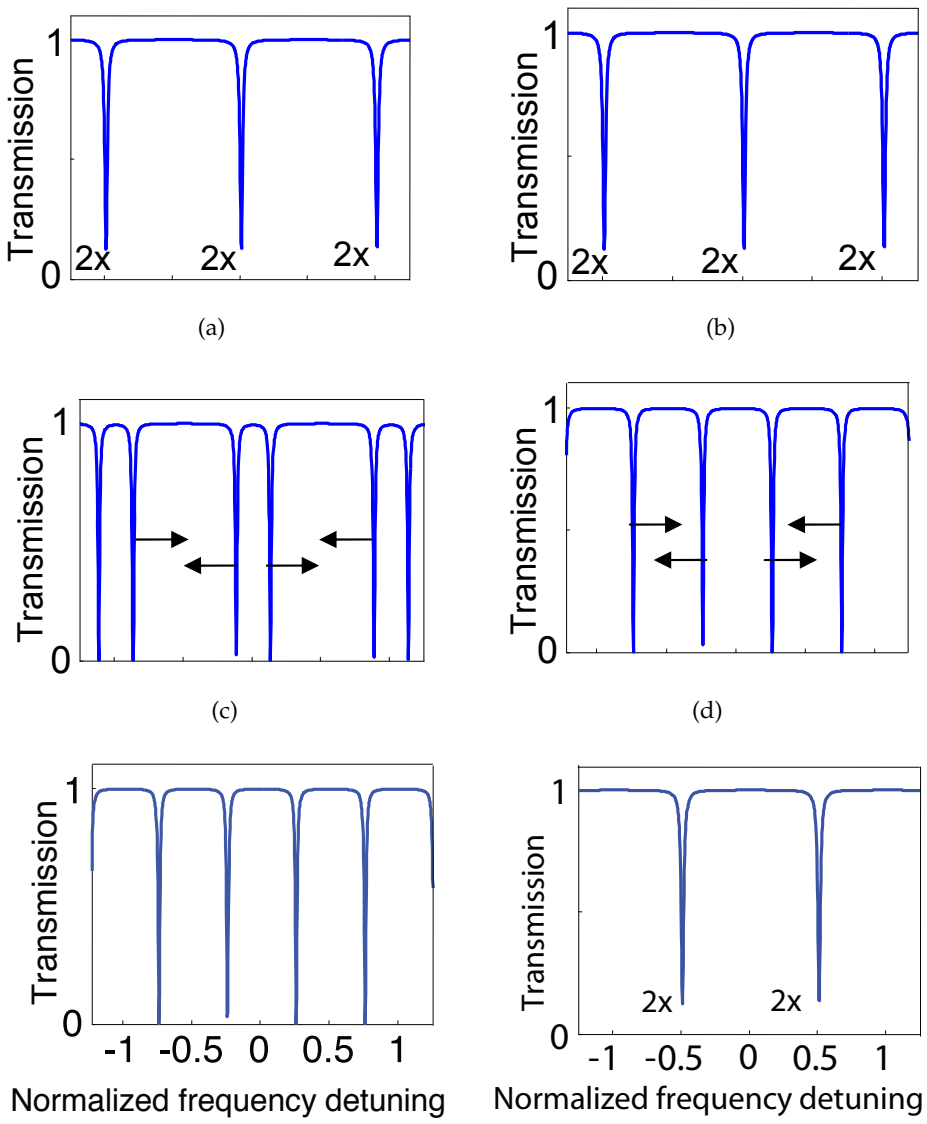

Figure 49: (a) ,(b), and (c) show the transmission spectra of a single-point-coupled resonator for $\kappa^2 = 0$, $\kappa^2 = 0.5$, and $\kappa^2 = 1$, respectively; coupled to an external bus waveguide. (d), (e), and (f) show the transmission spectra of a two-point-coupled resonator for $\kappa^2 = 0$, $\kappa^2 = 0.5$, and $\kappa^2 = 1$, respectively. The length of each resonator is 245 μm with an intrinsic Q is 10^5.

structures coupled to external bus waveguides are calculated and the results are depicted in Figures 49(a)-49(f). The transmissions are calculated using a similar transfer-matrix approach as in Ref. [71], with the transfer-matrix parameters of the single-point-coupled and two-point-coupled couplers derived in appendix A.1 (Eqs. 94 and 95). In these simulations an intrinsic Q of 10^5 is assumed for the SOI racetrack resonators with effective refractive index and group index of 2.5 and 4.25, respectively; corresponding to waveguides with a width of 480 nm and thickness of 230 nm buried under SiO_2 cladding. The length of each single resonator is considered to be 245 μm and the lower resonator is coupled to an external bus waveguide with a power coupling coefficient of $\kappa_{ex}^2 = 0.09$. The horizontal axes in Figs. 49(a)-49(f) is frequency detuning with respect to one of the modes of the uncoupled resonator (near $\lambda_o = 1.55\mu m$) normalized to the FSR of the uncoupled resonator. Figures 49(a) (49(d)), 49(b) (49(e)), and 49(c) (49(f)) show the spectra for the single-point-coupled (two-point-coupled) resonator structures for power coupling coefficients of $\kappa^2 = 0$, $\kappa^2 = 0.5$, and $\kappa^2 = 1$, respectively. The "2×" sign next to the drops in the transmission spectra indicates the presence of two degenerate modes at that particular frequency. It is observed that as the coupling coefficient increases from zero, the initially degenerate modes split and reach their maximum splitting for $\kappa^2 = 1$. For the single-point-coupled structure with $\kappa^2 = 1$, in each round-trip, electromagnetic field from one resonator completely couples to the second resonator with the addition of a phase shift of $\pi/2$ [49] and after traveling the second resonator, it couples back into the first resonator with an additional phase of $\pi/2$. As a result, the coupled-resonator device is equivalent to one resonator with twice the length of each single resonator with a total phase of π introduced in its roundtrip-phase. This is observed in Figure 49(c) where the FSR of the coupled-resonator is half the FSR of each single resonator (Fig. 49(a)) and the resonances are shifted by half of an FSR because of the additional π phase. For the two-point-coupled structure the interference between the two arms of the balanced MZI formed between the resonators, determines the effective mutual coupling between them. For example, at $\kappa^2 = 0.5$, the MZI has complete power coupling between the two resonators with the addition of a $\pi/2$ phase on the field amplitudes (excluding the propagation phase term). Hence, this structure acts exactly the

same as the single-point-coupled structure with $\kappa^2 = 1$; and as result, transmission spectra in Figures 49(d) and 49(e) are the same. However, in the two-point-coupled structure, for $\kappa^2 = 1$, the MZI has zero power coupling between the two resonators; hence, the two resonators are decoupled with an addition of a total phase of π introduced in the roundtrip-phase of each resonator as a result of the MZI phase (excluding propagation phase term in the straight part of the MZI). As a result of this additional phase, the modes of the coupled-resonator structure are shifted by half of an FSR compared to the uncoupled case of $\kappa^2 = 0$. Therefore, by looking at the evolution of modes in Figures 49(d) to 49(f), it is observed that as κ^2 is increased, even and odd supermodes travel half of an FSR in opposite directions and a net splitting of one whole FSR is observed in this structure. The arrows in Figs. 49(c) and 49(e) show the direction of the shift in the resonance modes as coupling coefficients in coupling points are increased.

The two-point-coupled resonator structure not only exhibits twice as much frequency splitting compared to the single-point-coupled structure, but also has an advantage from an engineering point-of-view. The Mach-Zehnder interferometer can be utilized to tune the resonator coupling strength by tuning the phase difference between the two arms of the interferometer. Figure 50 shows the normalized frequency-splitting as a function of phase difference between the arms of interferometer denoted by Arm1 and Arm2 in Fig. 48(c), respectively. Since any phase change in the interferometer arms changes the resonance frequency of the corresponding resonator, the two resonators will no longer be degenerate. To investigate only the effect of the change in the mutual coupling between the resonators, in this study, the resonance frequencies of resonators are kept unchanged by adding a compensating phase term to the round-trip phase of each resonator. This phase is equal to the phase added to the MZI arm of the same resonator with an opposite sign. The power coupling coefficient, κ^2, used in each simulation is indicated next to the corresponding curve. It is observed that the maximum splitting occurs for zero-phase difference and as phase difference increases to π, coupling and therefore splitting reduces to zero. Hence, mode splitting can be tuned to reach the desired value through this mechanism.

One important characteristic of the proposed coupled-resonator device is that the amount

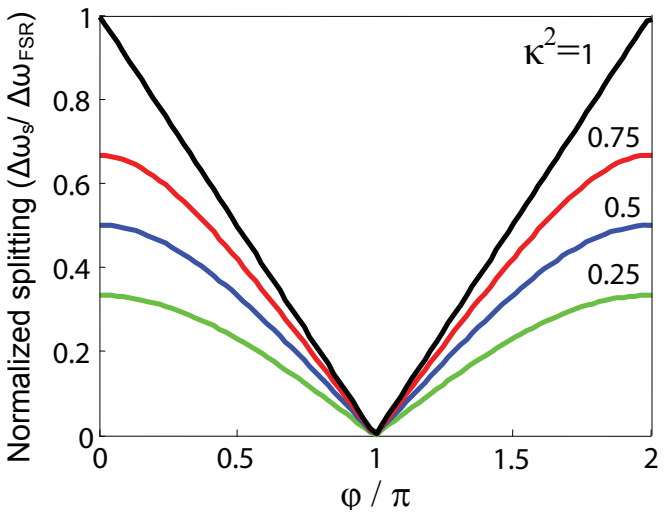

Figure 50: Normalized frequency splitting versus the phase difference between the two arms of the interferometer coupling the two resonators in the two-point-coupled structure shown in Fig. 48(c). Numbers over the curves indicate the value of κ^2. In these simulations we change the phase difference between the two arms of the Mach-Zehnder resonator (Arm1 and Arm2 in Fig. 48(c)). All other parameters in these simulations are the same as those in the caption of Fig. 49(a).

of field enhancements in the two individual resonators changes with κ^2; and consequently, the effective length of the device changes. For example, if the mutual coupling between the two resonators changes from one to zero, the effective length of the device changes from $2L_{res}$ to L_{res}, where L_{res} is the length of each resonator. Hence, within each resonator roundtrip, the mode experiences different levels of loss as the effective coupling between the two resonators changes. However, as the coupling to the bus waveguide is fixed within each roundtrip, different levels of extinction are observed at the resonance for different coupling strengths between the resonators. This is indicative of different levels of field enhancement in the device (e.g.: maximum enhancement is achieved at zero extinction or critical coupling condition). As field enhancement is one of the more important measures in many sensing and nonlinear optics applications, the effect of the resonator mutual coupling on the field enhancement is studied in section 4 in detail.

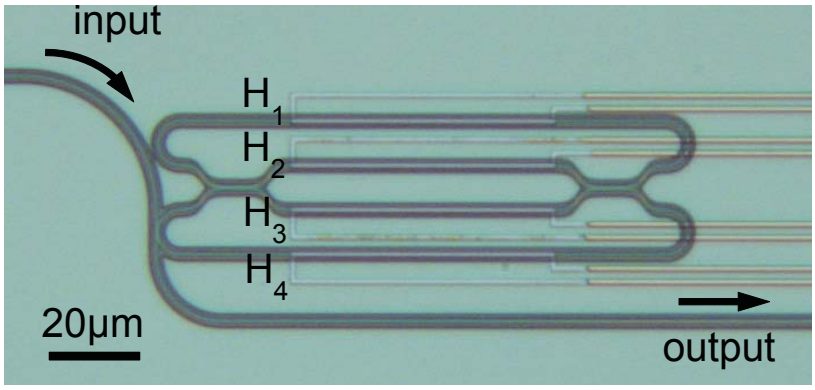

Figure 51: Optical micrograph of the two-point-coupled resonator structure fabricated on SOI with integrated microheaters. H1, H2, H3, and H4 show the microheaters fabricated on top of the structure for thermal tuning.

6.3 Fabrication and Experimental Results

To experimentally demonstrate the proposed idea, the coupled-resonator device with two-point-coupling is fabricated on an SOI wafer with silicon slab thickness of 230 nm, and a 1 μm thick buried oxide (BOX) layer (Fig. 51). Microheaters are integrated on the MZI to tune the coupling between the resonators. The width of the waveguides throughout the device is 480 nm to assure single-mode operation. The length of each resonator is 245 μm (including MZI length) and each arm of the Mach-Zehnder interferometer is 60 μm long. The DCs are identical and the gap and length of the parallel coupling region is 150 nm and 7.5 μm, respectively. The details of fabrication are explained in Section 3.2. Figure 51 shows the optical micrograph of the photonic device with integrated microheaters. Separate heaters are allocated to different parts of the device for independent control over coupling and resonance wavelength.

The transmission is measured by coupling light into and out of the device using tapered fibers in a standard optical characterization test setup. The TE-polarized light is incident on the device from a swept-wavelength tunable laser and the output of the device is coupled into a photodetector and the data is transferred to the PC using a data-acquisition (DAQ) card. Figure 52(a) shows the transmission spectrum of the device shown in Fig. 51. It is observed that two sets of modes with similar FSR of about 2.3 nm are present in the spectrum. This FSR corresponds to the FSR of each single resonator (which is 2.3 nm).

Also, the spacing between two adjacent modes from different sets corresponds to the mode splitting of the otherwise degenerate modes of the resonators. Because of the high level of coupling, modes of the two resonators are strongly split by approximately 0.86 nm. From this amount of splitting, power coupling coefficient of each DC between the two resonators is calculated to be $\kappa^2 = 0.42$, assuming the two couplers are identical. Intrinsic Q of the modes of the coupled-resonator structure is also measured to be 70,000.

By heating the upper interferometer arm through heater H2 (Fig. 51), coupling between the two resonators can be tuned. Figure 52(b) depicts the normalized transmission spectra of the two coupled resonance modes in the vicinity of $\lambda = 1.601\ \mu m$ for three different levels of power dissipation in heater H2. The number next to each spectrum is the power dissipation in the microheater. Similar tuning results are obtained for other FSRs in Fig. 52(a). Horizontal axis in Fig. 52(a) shows the wavelength detuning from the center of the coupled modes (or supermodes). It is observed that as the phase mismatch between the arms of the interferometer is increased (through applying heat), coupling between the resonators and consequently the mode spacing between the coupled modes is decreased. In addition to the change in the resonator coupling strengths, resonance wavelength of the upper resonator is red-shifted while heating the upper interferometer arm. This causes the center of the two coupled resonant modes (even and odd supermodes) to be red-shifted as their spacing is reduced. Here, this red-shift is compensated by introducing an appropriate wavelength offset to the experimental data, so that the centers of coupled-modes in each transmission spectrum match. In practice, by simultaneous tuning of all fabricated heaters, center wavelength of two resonators can remain unchanged while their mutual coupling is tuned. Figure 53 shows the change in resonance wavelength spacing of the even and odd coupled-modes for the structure in Fig. 51 for different power dissipations in heater H2. It is observed that 0.4 nm change in wavelength spacing between coupled modes is achieved by dissipating 27 mW in H2. This amount of change is equivalent to 20% of the FSR of the uncoupled resonators.

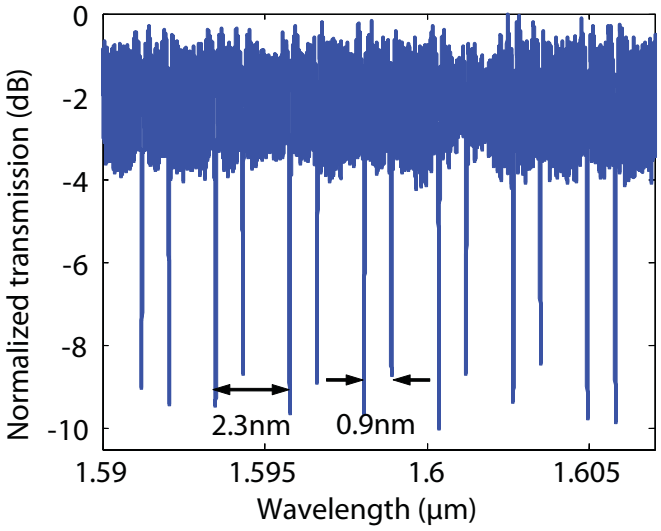

(a)

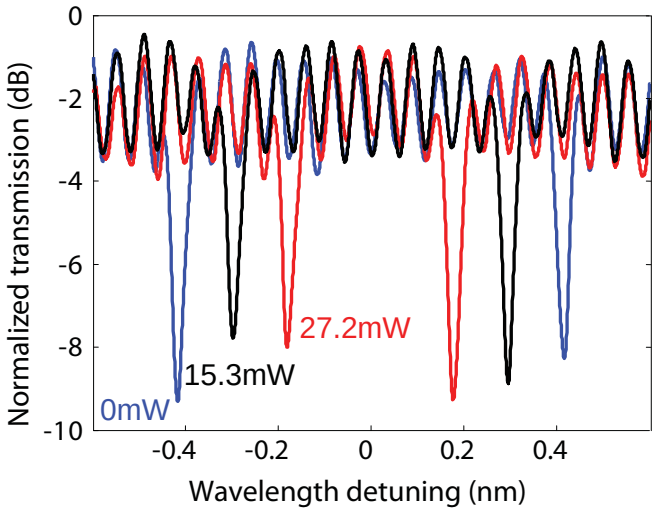

(b)

Figure 52: (a) Normalized transmission spectrum of the coupled resonator structure shown in Fig. 51 (b) Normalized transmission spectra of the two coupled modes near $\lambda = 1.601\mu$m for different power dissipations in heater H2 (Fig. 51). Horizontal axis is wavelength detuning with respect to the center of the two coupled modes. A wavelength offset is added to the data to compensate for the red-shift in the resonance wavelengths of the modes in the coupled-resonator structure.

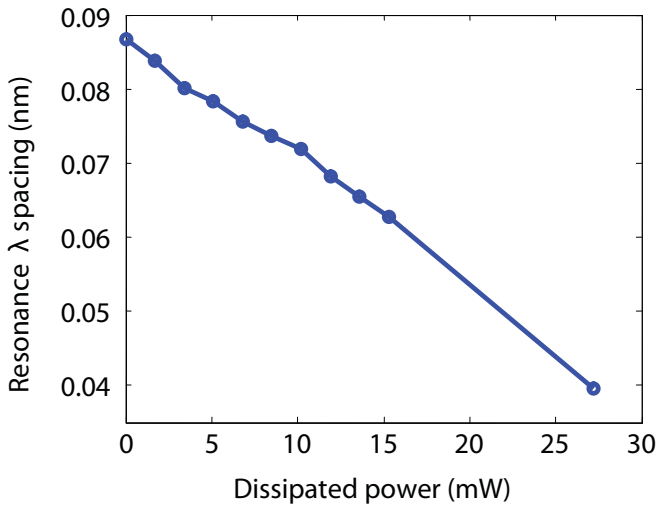

Figure 53: Resonance wavelength spacing versus power dissipation in heater H2 for the structure shown in Fig. 51.

6.4 Discussion

The results shown in Section 3 clearly show that the spacing of the adjacent modes of the resonator-based device can be tuned by a relatively large amount by using a single heater. The fact that the splitting between adjacent modes in Fig. 51 can change from 0.86 nm (zero power dissipation) to 0.4 nm (equal to 20% of an FSR) with only 27 mW heating power dissipation in H2, proves that the resonator-based device in Fig. 51 can be used for a large set of signal conditions in applications like nonlinear optics in which signals with different wavelengths interact. By tuning the mode spacing, we can achieve resonance condition and simultaneous field enhancement for the involved signals. The amount of field-enhancement is an important characteristic which determines the device performance and needs to be addressed for any proposed device. As our proposed resonator structure is composed of an interferometer in addition to resonators, its field-enhancement characteristic is expected to be different compared to a simple resonator. Using a similar transfer-matrix approach as in Ref. [71], field-enhancement of the even and odd supermodes in the two resonators of the two-point-coupled structure (Fig. 48(c)) are calculated as a function of phase difference between the two arms of the interferometer, and the results are shown in Fig. 54. In these simulations, the total lengths of both

resonators are 245 μm; the lengths of the interferometer arms are 60 μm; the power coupling coefficients of DCs between the two resonators are $\kappa^2 = 0.7$; and the power coupling coefficient for the coupling of the bus waveguide to the lower resonator is (close to the critical coupling condition for an intrinsic Q of 10^5). The intensity enhancements shown in Fig. 54 are denoted by a and defined by the ratio of the intensity of the field of each resonant mode inside the resonator to the intensity of the field at the input waveguide. Subscripts 1 and 2 determine the fields in the bottom resonator (R1) and the top resonator (R2), respectively. Also, the modes with lower and higher frequency are called even and odd mode, respectively. Figure 54 shows that as the MZI phase difference increases, the amount of enhancement of the even (odd) mode in R1 increases (decreases) until $\kappa^2 = 0.8$. As κ^2 further increases, R2 becomes decoupled from R1; the field in R2 drops to zero; and the enhancement of both even and odd modes increases in R1. The reason for this high increase in the field-enhancement is because of the decrease in the effective length of the coupled-resonator system as the resonators are decoupled. This decrease in the effective length results in the decrease of the mode-volume of the structure, which directly translates into a higher field enhancement. In simulations, as Φ approaches π, even and odd modes gradually overlap and become numerically indistinguishable. In Fig. 54, the dashed lines connect the last simulation point for which even and odd modes were distinguishable (i.e., $\kappa^2 = 0.95$) to the limiting case of zero coupling (i.e., $\Phi = \pi$), where the two modes completely overlap. It is observed that in each resonator (R1 and R2) both even and odd modes exhibit field enhancement simultaneously. This confirms that waves in resonance with these modes exhibit enhanced nonlinear interaction. However, this enhancement varies as the resonance frequency spacing is tuned and this has to be taken into account for any application.

6.5 Tuning of Frequency Mismatch for Four-Wave Mixing Application

In this chapter, we demonstrated the possibility of tuning of the frequency spacing of the resonance modes of a coupled-resonator device. This capability has a unique and valuable application in fine-tuning of the resonance frequencies for a four-wave mixing

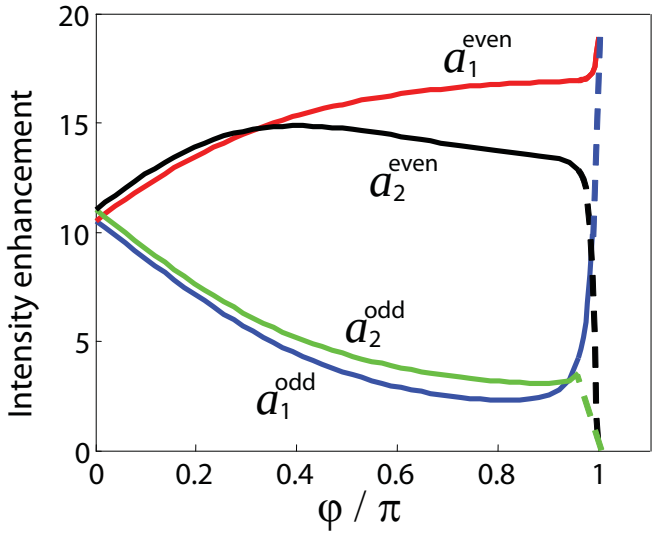

Figure 54: Intensity enhancement of even and odd supermodes in R1 (bottom resonator) and R2 (top resonator) as a function of the phase difference between the interferometer arms in Fig. 48(c). Dashed parts of each curve connects the last simulation data-point for which the odd and even modes could be resolved, to the final value at π phase-shift (uncoupled case).

(FWM) process in microresonators. FWM is a parametric nonlinear process which in its degenerate configuration, two identical pump photons and one signal and one idler photons interact together [1]. In order to implement this process in a TWR, three resonance modes that are equally spaced in frequency are needed (i.e., $\omega_{p0} - \omega_{s0} = \omega_{i0} - \omega_{p0}$ or $2\omega_{p0} - \omega_{s0} - \omega_{i0} = 0$). This requires a zero group-velocity dispersion in the TWR, which is achieved through the precise engineering of the TWR dimensions [2]. Using the coupled-resonator device proposed in this chapter, we are able to dynamically tune the resonance frequency of the TWR to meet the dispersion condition. Frequency mismatch was defined in Chap. 5 as

$$\Delta\Omega = 2\omega_{p0} - \omega_{s0} + \omega_{i0} \tag{86}$$

where ω_{s0}, ω_{p0}, and ω_{i0} are the resonance frequencies of three resonance modes of the TWR employed in the degenerate FWM process. Ideally, we would like to tune the frequency mismatch to zero, which we show is achievable through the two-point coupled-resonator

[1] This process is explained in Chap. 5 in detail.
[2] As discussed in Chap. 5, the TWR should be engineered to have an anomalous dispersion.

demonstrated in this chapter.

Figure 55(a) shows the optical micrograph of the coupled-resonator device with integrated microheaters used for tuning of the frequency mismatch. The total length of the coupled-resonator is approximately 318 μm, power coupling coefficient of the couplers between the resonators is slightly higher than 0.5 at 1.55 μm, and the length of the MZ in the coupling region is 5 μm. Figure 55(b) shows the normalized transmission spectrum of this device without microheaters used. The spacing of the resonance modes is around 1.8 nm at 1.55 μm. We calculated the frequency mismatch for the three consecutive resonance modes and the results are shown in Fig. 56(a) by the blue circles. It is observed that the frequency mismatch changes sign alternatively and its value reduces at 1.53 μm. The dispersive nature of the frequency mismatch is because of the wavelength dependence of the couplers used to couple the resonators. Basically, when the coupling ratio of both couplers is 50% (or the total coupling of the resonators is 100%), frequency detuning is zero. In our design, this can be achieved by heating the MZ interferometer in the coupling region to adjust the coupling to 100%.

By heating resonators and the MZ interferometer, we can tune the frequency mismatch in this resonator. The red and black circles in Fig. 56(a) show the frequency mismatch for two different configurations of the microheaters. The red circles show that by slightly heating H2 and H4 (exact amounts shown in Table 55(a)), it is possible to fine tune the frequency mismatch close to the zero line. Also, through more heating, the zero frequency mismatch is shifted by 20 nm to 1.55 μm as shown by the black circles. This amount of change in the zero-frequency-mismatch point is practically significant as it enables using this device for a wide range of pump wavelengths. Figure 56(b) shows the amount of power dissipation in each microheater for different tuning configurations. The color of each row matches with the color of the circles shown in Fig. 56(a). One of the advantages of this device over a simple TWR with engineered dispersion is that here only one set of modes satisfy the zero frequency mismatch. This eliminates the cross-talk to adjacent channels that is usually observed in FWM-assisted wavelength conversion in fiber optics systems caused by zero frequency mismatch in a wide wavelength range.

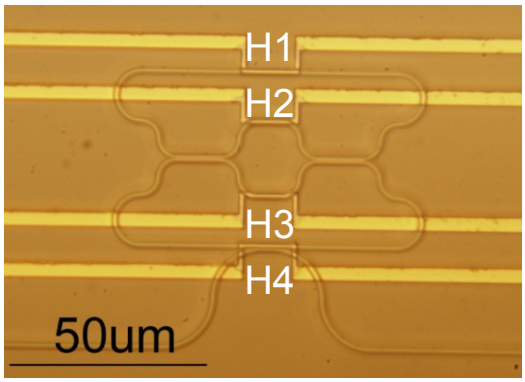

(a)

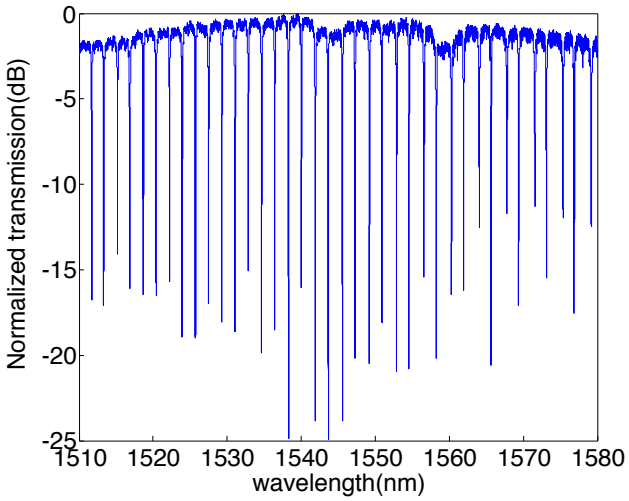

(b)

Figure 55: (a) Optical micrograph of the two-point coupled-resonator device with integrated microheaters for tuning of the frequency mismatch. (b) Normalized transmission spectrum of the device shown in (a) without heating of microheaters.

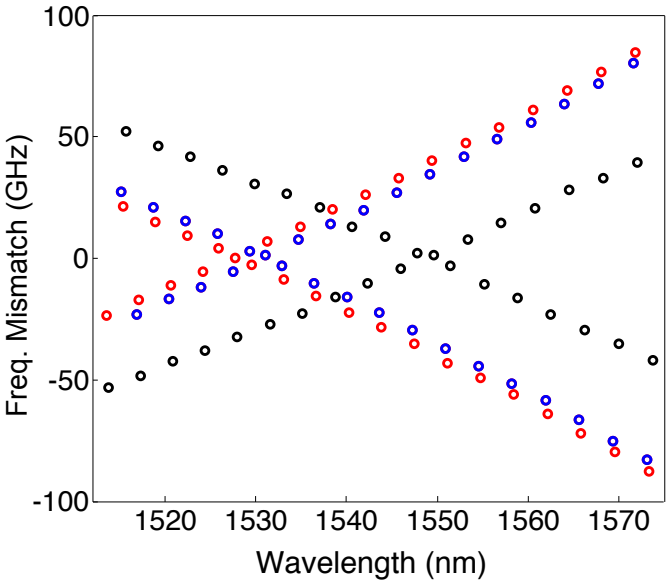

(a)

H1(mW)	H2(mW)	H3(mW)	H4(mW)	Total
0	0	0	0	0
0	3	0	3	6
6.8	3	6.8	0	16.6

(b)

Figure 56: (a) Frequency mismatch of the coupled-resonator device shown in 55(a) for different tuning configurations. Power dissipation in each miroheater is summarized in the table shown in (b). (b) Tabulates the amount of power dissipation in each microheater for each tuning configurations. The color of each row matches with the color of the circles shown in (a).

CHAPTER VII

COUPLED-RESONATORS FOR NONLINEAR OPTICS APPLICATION

7.1 Introduction

In Chapter 5 we theoretically demonstrated the possibility of nonlinear processes such as FWM in Si resonators with pump powers in the order of a milliwatt, thanks to the high level of field-enhancement achievable in these devices. This low-power operation makes these devices great candidates for numerous chip-scale nonlinear processes such as, wavelength conversion, signal regeneration, and optical parametric oscillation. These processes have numerous applications in fiber optics systems and optical interconnects. However, a simple traveling-wave resonator (TWR) has a fundamental design issue for nonlinear optics applications. This issue rises from the fact that both field-enhancement and free-spectral range (FSR) of the resonator are inversely proportional to the resonator length. Thus, field-enhancement is forced by the length of the resonator which is designed based on the required FSR in the system. This results in considerable reduction of field-enhancement at small FSR values.

Considering a wavelength conversion process in a DWDM system, the spacing between the signal and converted (idler) channels can range from a few nanometers to tens of nanometers. This requires resonators with FSRs in the order of a few nanometers. Therefore, it is not possible to use ultrasmall microdisk resonators with high field-enhancement properties because of their large FSR (more than 50 nm). This design issue results in considerable increase in the pump power requirement.

In this chapter, we propose a novel TWR based on coupled resonators that allow to tackle this FSR-enhancement design challenge in a FWM process [1]. By over-coupling [2]

[1] While this device is demonstrated for degenerate FWM, the same design methodology can be applied for numerous nonlinear optics processes

[2] The coupling strength should be high enough that the supermodes of the coupled-resonator device are split more than the linewidth of the resonances.

three TWRs, three supermodes are created for which the spacing of the modes directly depends on the coupling strength between the resonators. This allows us to determine the spacing between the resonance modes (in resonance with the interacting waves) independent of the length of the resonator [3]. For example, by changing the gap between these resonators, the coupling strength and the resulting resonance splitting is determined independent of the resonator length. We will theoretically and experimentally show in this chapter that this device can potentially improve wavelength conversion efficiency by orders of magnitude over a simple TWR.

The proposed coupled-resonator device can also enable the tunability of wavelength in a FWM process. This can be achieved by tuning the resonance of the individual resonator frequencies that in turn changes the splitting of the supermodes of the device. This tunability bridges between waveguides that have a very large operating bandwidth with simple resonators with very small resonance linewidths. Thus, with the addition of a tuning mechanism it is possible to benefit from the high field enhancement of resonators and at the same time be able to tune the device for a wide range of signal/pump/idler wavelength configurations.

7.2 Coupled-Resonators for Four-Wave-Mixing: Proposal and Numerical Modeling

Here, we propose a coupled-resonator device for a degenerate FWM [4] process in Si that is great practical interest. To implement this process in a resonator, three resonance modes that are uniformly spaced in frequency are needed. Figure (57) shows the schematic of a ring resonator for degenerate FWM with the possible pump/signal/idler frequency combinations. In the absence of dispersion, modes with azimuthal mode orders $m - N$, m, and $m + N$ can be used for signal(idler), pump, and idler(signal) waves, respectively. Considering a wavelength conversion process, idler photon is generated through the interaction of two pump and one signal photons. Equation (66) represents the temporal

[3] It should be noted that by using three microresonators, mode-volume is increased by a factor of three and the field-enhancement is reduced by a factor of three.

[4] In the degenerated FWM, two identical pump photons and one signal and one idler photons interact.

evolution of this idler wave in a resonator. The last term on the RHS of this equation is the contribution from the FWM gain. This term is proportional to $A_p^2 A_s$, where $|A_p|^2$ and $|A_s|^2$ are the energies of the pump and signal waves in the resonator, which are proportional to the field-enhancement factor in the resonator (see Eq. 27). Idler power coupled at the output waveguide is also proportional to $|A_i|^2$. Therefore, idler power at the output is proportional to the fourth power of the field-enhancement factor in the resonator. For a simple TWR, field intensity enhancement is given by Eq. (27), which at critical coupling is simplified to

$$FE_v = \frac{1}{\pi}\frac{Q_T \lambda_0}{n_g L_r} \tag{87}$$

where Q_T is the total Q of the resonator, n_g is the group velocity of the traveling wave, L_r is the length of the resonator, and λ_0 is the free-space wavelength of the mode. It is clearly seen that field intensity enhancement is inversely proportional to the resonator length. Therefore, in a simple TWR, wavelength conversion decreases with the fourth power of the resonator length (i.e., L_r^{-4}). Now, the question is that is there any way to avoid this enhancement-FSR interdependence that is causing a big loss in the nonlinear gain (for fixed input power). In this chapter, we introduce a novel design methodology in TWRs that enables the engineering of resonance modes to avoid this design issue.

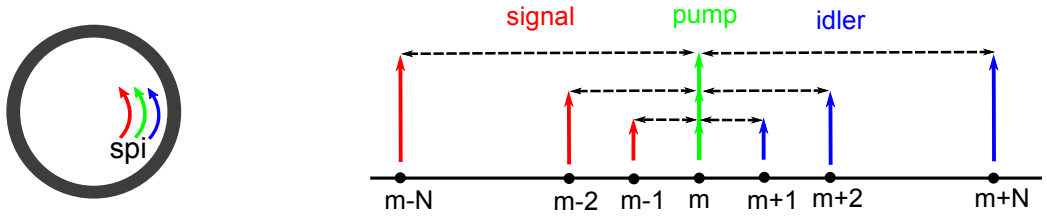

Figure 57: Figure on the left shows the schematic of a microring resonator used for a degenerate FWM process. Figure on the right shows different pump/signal/idler frequency configurations that are possible for a degenerate FWM process based on the modes of the resonator with a fixed FSR.

One approach to engineer the resonance modes of a TWR is through exploiting the supermodes of a coupled-resonator structure. If the strength of the coupling is high enough, the supermodes of the coupled structure split and the amount of splitting is determined by the mutual strength of between the resonators. The same methodology was also used in Chap. 6 to tune the spacing of resonance modes. This method provides a practical

approach for the engineering of resonance modes. Specifically for a degenerate FWM application, three resonance modes can be created by coupling three TWR as shown in Fig. 58(a). By adjusting the coupling strength between the resonators, the desired amount of spacing between these modes is achieved (See Fig. 58(b)). This allows us to use small microresonators to have high light enhancement and at the same time be able to design the spacing of the modes independent of the size of microresonators. The significance of this idea is more pronounced considering recent achievements in high-Q ultrasmall microresonators such as microdisks [7].

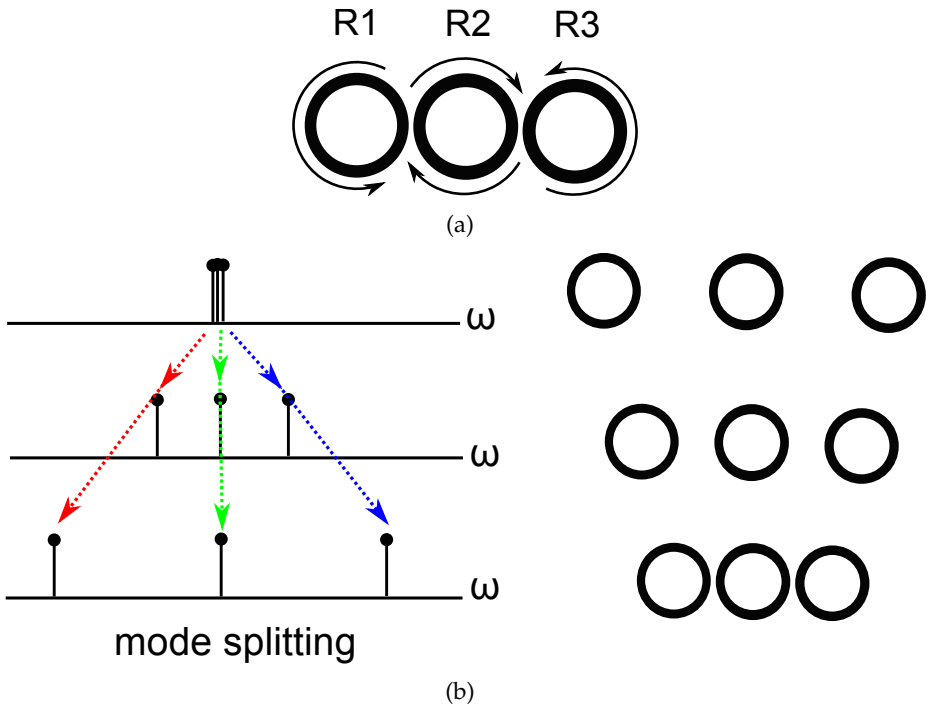

Figure 58: (a) shows the schematic of a coupled resonator structure composed of three microring resonators for degenerate FWM. (b) schematically shows the characteristic of mode splitting in the device shown in (a) when the coupling between the resonators is increased. The coupled microrings on the right represent that by reducing the gap between resonators, coupling and mode splitting can be increased.

One important issue to investigate in this resonator is the light enhancement in all of the resonators. This is important because for an efficient nonlinear process all of the interacting waves should be simultaneously enhanced inside the material. It is expected that because of the supermode nature of the three split modes, light is enhanced for all these modes

in all three resonators. We study this by simulating wave propagation inside a coupled-resonator structure composed of small microdisks with a diameter of 5 μm. Figure 59(a) shows the schematic of this device in which a bus waveguide is coupled to the bottom resonator. Here, we consider effective and group indices of 2.5 and 4.25, respectively. We also consider an intrinsic Q of 100,000 for the resonator and adjust the coupling between the bus waveguide and coupled-resonator to satisfy critical-coupling condition for the mode in the middle (i.e., pump mode). Figure 59(b) shows the normalized transmission spectrum of this device for one group of supermodes near 1.57 μm for different coupled strengths between the resonators (coupling between resonators is the same in each device). It is observed that while the mode in the middle is critically coupled, the two side modes are not. This is because of different light-enhancement properties of these modes in this coupled-resonator device. Figures 60(a), 60(b), and 60(c) show the normalized intensity of the field inside R1, R2, and R3 resonators, respectively. It is observed that different modes at different wavelengths have different enhancement factors. This dispersive effect in enhancement factor is stronger for smaller coupling values and is eliminated for 100% coupling between the resonators. At the maximum coupling value, the coupled-resonator structure acts as a simple TWR with a length three times that of a single resonator. Regardless of this dispersive effect in the enhancement, simultaneous enhancement of all the three modes is observed in all of the resonators. This is enough evidence for an efficient nonlinear optics process in such resonator.

7.2.1 Tunability of Wavelength in Resonator-Enhanced FWM

One of the challenges of moving to resonators from waveguides is the very narrowband nature of resonance modes. This inhibits the use of resonators for wideband applications and in cases where the exact wavelength of the waves is not known before the design of the device (e.g., Raman sensing). Using the three-element coupled-mode resonator proposed in the previous section we theoretically demonstrate the possibility of tuning of the signal and idler modes symmetrically with respect to the pump mode.

In the three-element coupled-resonator device shown in Fig. 58(a), the splitting of the

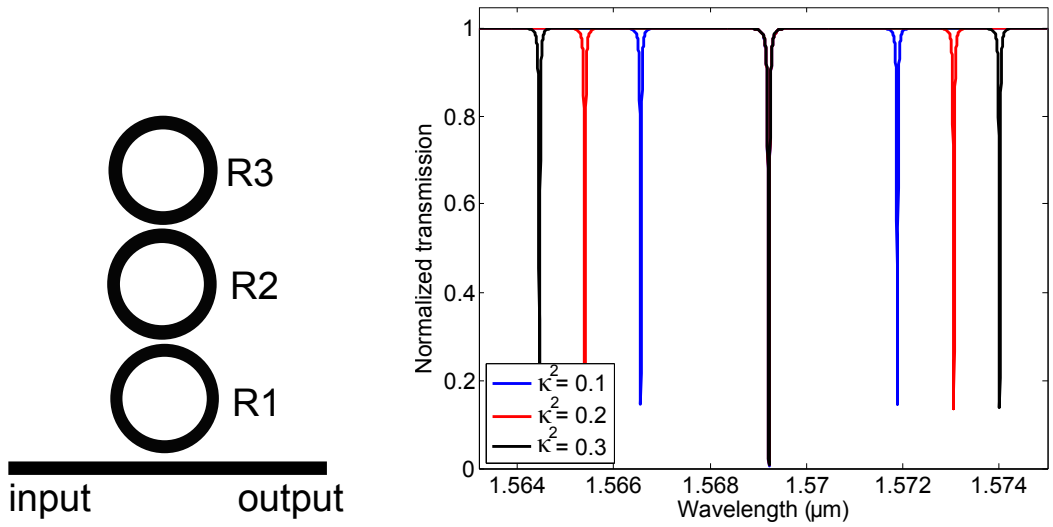

(a) (b)

Figure 59: (a) The structure of a coupled-resonator consisting of three identical microrings coupled to a bus waveguide. (b) Transmission spectrum the device shown in (a) composed of 5 μm diameter microdisks for different values of resonator coupling coefficients. Coupling to the input waveguide is chosen such that the mode in the middle (pump wavelength) is critically coupled.

three supermodes can be tuned by either tuning the coupling ratio between the resonators or through the detuning of the resonance frequency of individual resonators with respect to each other. The tuning of the coupling can be achieved by coupling the resonators using a MZ interferometer (as shown in Chap. 6). Considering the practical size of a MZ interferometer, the resulting device becomes large and does not serve its purpose for light enhancement. Thus, a more practical way to achieve the tuning of the mode splitting in this device, is through the detuning of the resonance frequency of individual resonators. Here, we assume that this tuning is achieved through the thermo-optic effect in a silicon-based coupled-resonator in which the temperature of the top resonator is increased by ΔT, the temperature of the bottom resonator is decreased by the same amount, and the middle resonator is kept fixed. Other tuning scenarios can also be applied.

Figure 61(a) shows the transmission spectrum of the proposed coupled-resonator structure when the top and bottom resonators are detuned in opposite signs with respect to the middle resonator. We considered 5 μm diameter microdisk resonators with an intrinsic Q of 100,000 with mutual coupling coefficient of $\kappa^2 = 0.3$. Blue, red, and black curves

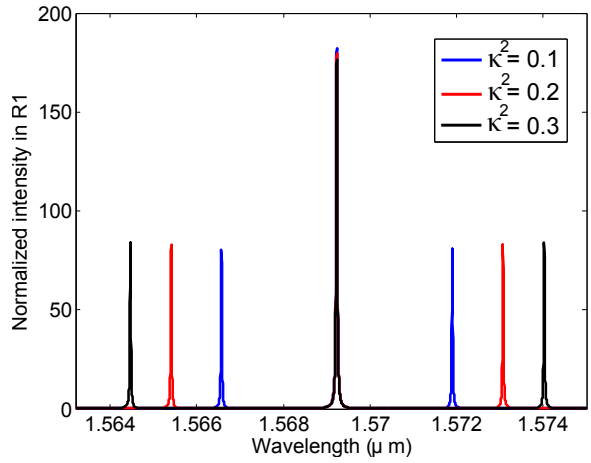

(a)

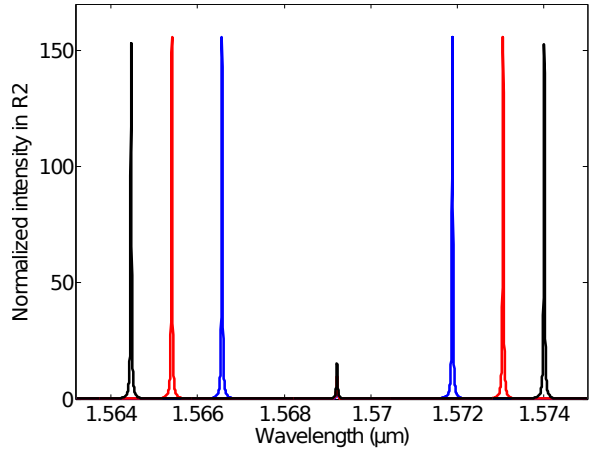

(b)

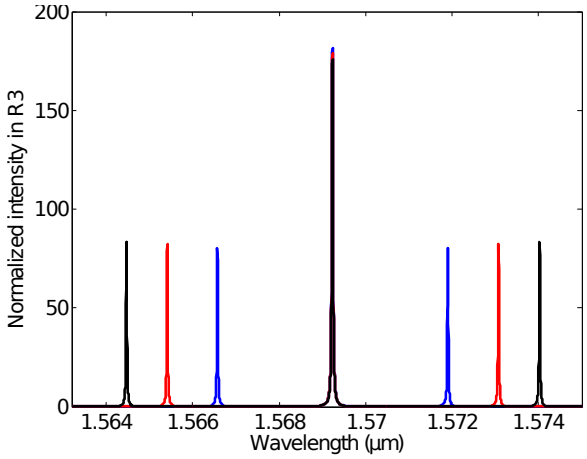

(c)

Figure 60: (a), (b), and (c) show the normalized intensity of the field inside the bottom (R1), middle (R2), and top (R3) resonator in a three-element coupled resonator device. Device parameters are the same as those defined in the caption of Fig. 59(b).

show the transmission spectrum for the temperature change (ΔT) of 0, 50, and 100 degrees, respectively. It is observed that the splitting of modes is increased as a result of this tuning. Figure 61(b) shows the change in wavelength splitting versus temperature change (i.e., ΔT in the top resonator, 0 in the middle resonator, and $-\Delta T$ in the bottom resonator). The wavelength spacing is defined as the splitting between the pump and signal modes, $|\lambda_p - \lambda_s|$, where λ_p and λ_s represent the modes associated with the pump and signal waves, respectively. It is observed that the wavelength spacing can be tuned from 4.5 nm to almost 8 nm. This amount of tuning of the wavelength spacing is relatively large considering the spacing of two adjacent DWDM channel which is 0.8 nm.

It is also important to analyze the field enhancement in this device as the wavelength spacing is tuned through the proposed approach. As explained in the previous section, wavelength conversion efficiency is proportional to $|A_p|^2.|A_s|.|A_i|$ where, $|A_p|$, $|A_s|$, and $|A_i|$ are the field amplitudes of pump, signal, and idler normalized to the resonator energy. Figure 62 depicts the value of $|IE_p|^2.|IE_s|.|IE_i|$ in each resonator, where $|IE_v|$ is the intensity enhancement in the corresponding resonator. It is observed that the intensity enhancement changes considerably with the tuning of the wavelength spacing; however, the total amount of conversion efficiency drops by almost a factor of 10 while the wavelength spacing is tuned from 4.5 nm to 8 nm.

7.3 Experimental Results

In this section, the details of the fabrication and characterization of the coupled-resonator devices proposed in the previous section are explained. Here, we have incorporated nano-tapers with polymer spot-size converters to increase the coupling efficiency to the structure for actual FWM characterization. Wavelength conversion efficiency is characterized in these devices and the experimental results are compared to the theoretical modelings. We also elaborate on the physics of the phase-matching condition in these devices that is required for a FWM process.

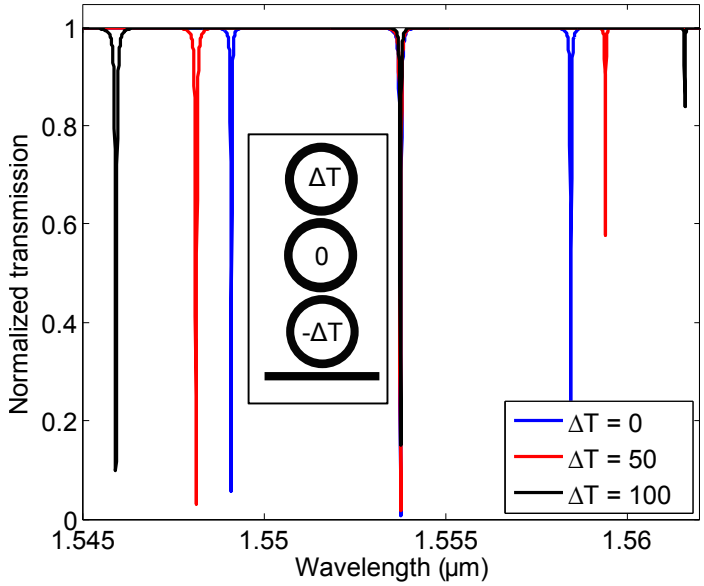

(a)

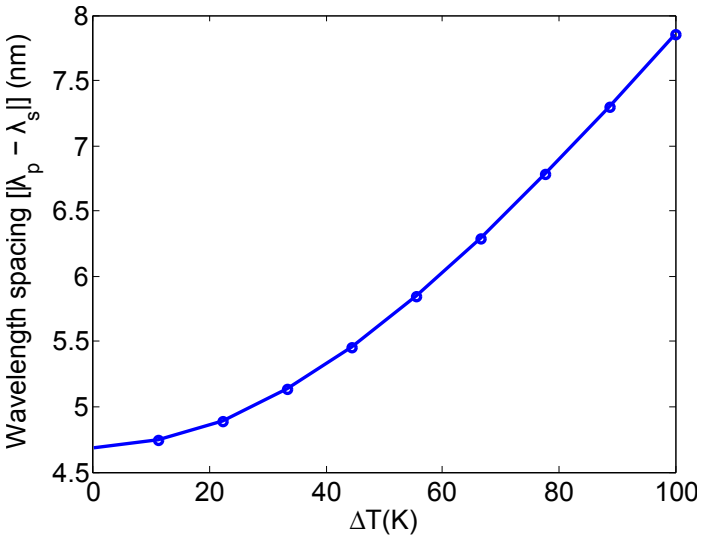

(b)

Figure 61: (a) shows the transmission spectrum of the three-element coupled-resonator as its wavelength spacing is tuned by detuning the resonance wavelength of the top and bottom resonators in opposite signs with respect to the middle resonator. In this tuning scheme, the temperature of the top resonator is increased by ΔT, the temperature of the bottom resonator is decreased by the same amount, and the middle resonator is kept fixed (as shown in the inset). Other device parameters are the same as those defined in the caption of Fig. 59(b). (b) The amount of tuning in the wavelength spacing versus the temperature change in tuning scheme described in (a). Wavelength spacing is defined as the splitting of the pump and signal modes, $|\lambda_p - \lambda_s|$.

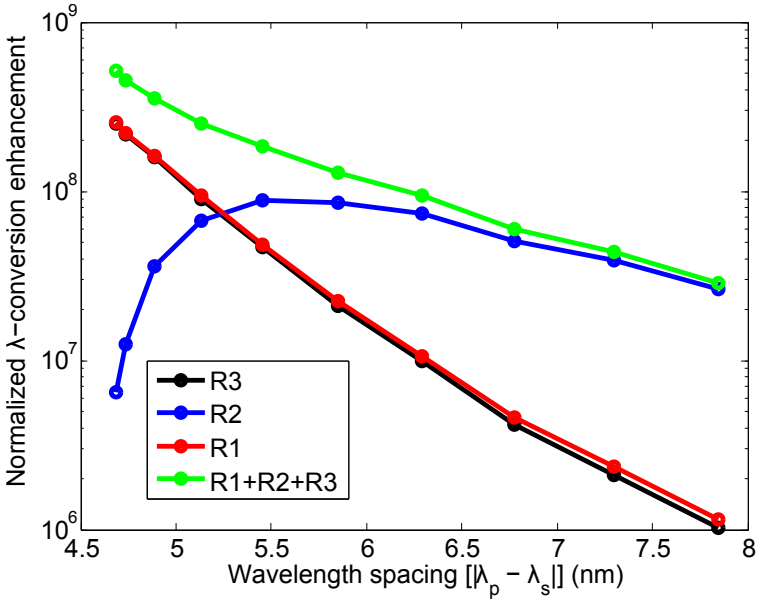

Figure 62: Normalized wavelength-conversion enhancement in the three-element coupled-resonator device versus the wavelength spacing of the pump and signal modes. Here, wavelength-conversion enhancement of each resonator is defined as $|IE_p|^2.|IE_s|.|IE_i|$, where $|IE_\nu|$ is the intensity enhancement in the corresponding resonator. Red, blue, and black curves show the normalized FWM gain in the bottom (R1), middle (R2), and top (R3) resonators, respectively. Green curve shows the combined normalized FWM gain in all the resonators.

7.3.1 Fabrication

We fabricated two types of coupled-resonator devices for FWM, one based on ultra-compact microdisks (Figs. 63(a) and 63(b)) and one based on compact racetrack resonators (Figs. 64(a) and 64(b)). These devices are fabricated on SOI wafers with Si thickness of 235 nm and buried oxide (BOX) thickness of 1 μm[5]. Photonic devices are defined using HSQ electron-beam resist with JEOL 9300 and subsequently etched using inductively-coupled plasma (ICP) with Cl_2 chemistry. Devices are then spun-coated with 600 nm Flowable oxide (FOx-16). FOx is removed from the edges of the nanotaper waveguides using SU8 photoresist mask. The edges of the nanotaper should not be covered with any cladding material until the final step, in which SU8 mode-size converter waveguides are fabricated over them. Then 400 nm plasma-enhanced CVD (PECVD) SiO_2 is deposited on the remaining FOx using a shadow mask. Microheaters and contact pads are defined using ZEP-520A electron-beam resist. 5 nm Ti adhesion layer, 100 nm NiCr (microheater), and 150 nm Au (contacts and pads) are subsequently deposited using electron-beam evaporation and the microheater/contacts are defined using a lift-off process. Au is then selectively wet-etched using Transcene GE-8148 Au-etchant from the top of devices to increase the electrical resistance of the microheaters. At last, SU8 spot-size converter waveguides are patterned using electron-beam lithography.

Figure 63(a) shows the optical micrograph of the fabricated coupled-microdisk device with integrated microheaters (Fig. 63(b) shows the SEM of the photonics of this device before cladding deposition). Here, the outer and inner diameters of the microdisk are 4 μm and 2 μm, respectively. The width of the input waveguide is designed to be 320 nm for phase-matching to the first radial-order mode of the microdisk. The same device that is designed using racetrack resonators is shown in Figs. 64(a) and 64(b). Here, the diameter of the curved part of the racetrack is 6 μm and the straight part is 5.5 μm. The gap between the resonators is 100 nm and the gap between the input bus waveguide to the adjacent resonator is 125 nm. This gap size provides critical coupling to the coupled-resonator

[5]This BOX thickness results in very lossy TM-like modes, and as a result only TE-like polarization is present at the output of the chip. This eliminates the need for a polarizer at the output, which simplifies the test setup.

device.

Figure 65(a) shows the SEM cross-section of the 3 $\mu m \times 3 \mu m$ SU8 spot-size converter waveguide. This waveguide size has an effective mode-diameter of 2.5 μm, which almost exactly matches with the mode diameter of the tapered fiber used in our experimental setup. Figure 65(b) shows the SEM of the 50 nm wide Si nanotaper. The tapering in this device is linear.

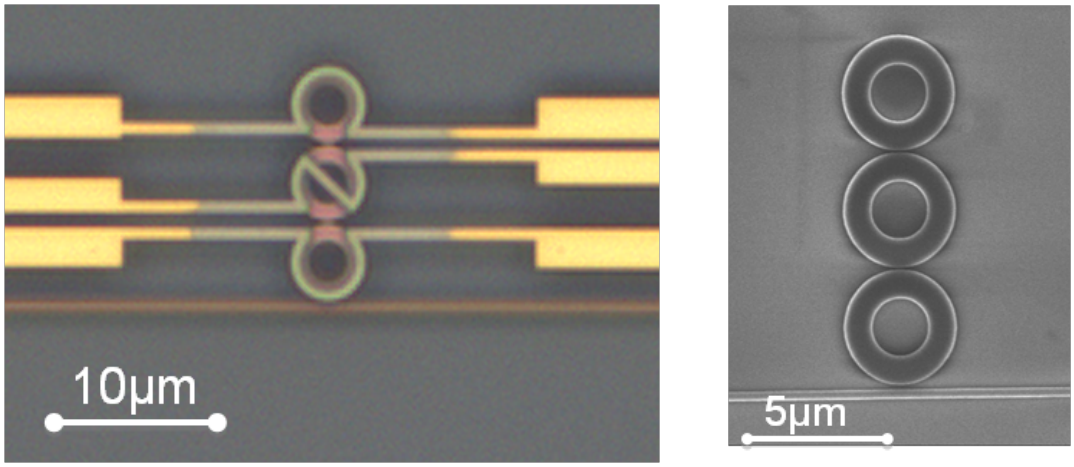

(a) (b)

Figure 63: (a) and (b) are the optical micrograph and the SEM of the fabricated coupled-microdisk device with integrated microheaters, respectively. The outer and inner diameters of the microdisk are 4 μm and 2 μm, respectively. The width of the input waveguide is designed to be 320 nm.

7.3.2 Characterization

Figure 66 shows the experimental setup used for the characterization of FWM process in the coupled-resonator device proposed in this chapter. Here, two CW lasers are used for the pump and signal. Pump laser is amplified using an EDFA and then passed through a tunable band-pass filter to reject the amplified spontaneous emission (ASE) of the amplifier. Pump and signal are combined using a 3dB coupler and coupled to the device. Three polarization controllers are used to adjust the polarization of both pump and signal sources to the TE polarization before coupling to the Si chip. 1% input power is coupled to a power-meter before coupling to the chip. Tapered fibers are used to couple light into and out of the chip. The optical output is detected using either a photo-detector or an optical spectrum

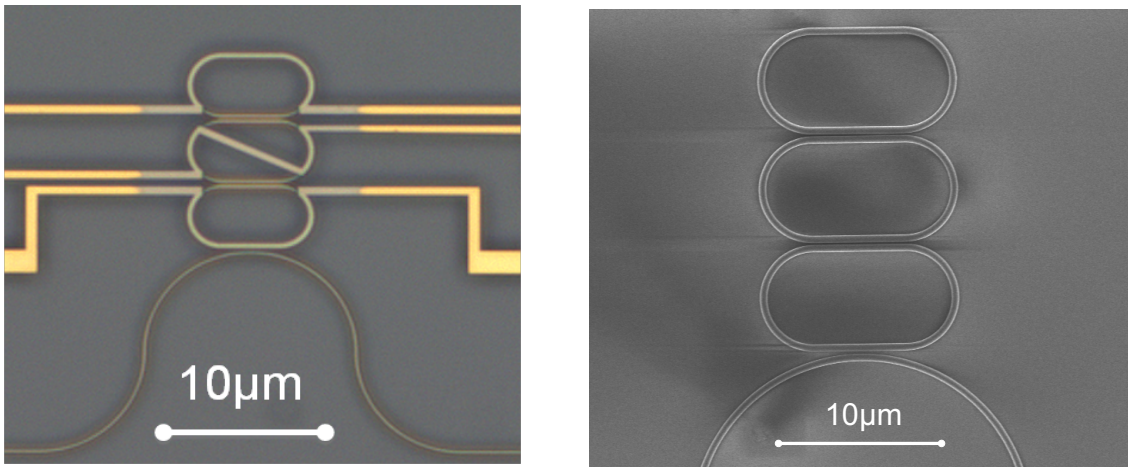

(a) (b)

Figure 64: (a) and (b) are the optical micrograph and the SEM of the fabricated coupled-racetrack device with integrated microheaters, respectively. The diameter of the curved part of the racetrack is 6 μm and the straight part is 5.5 μm.

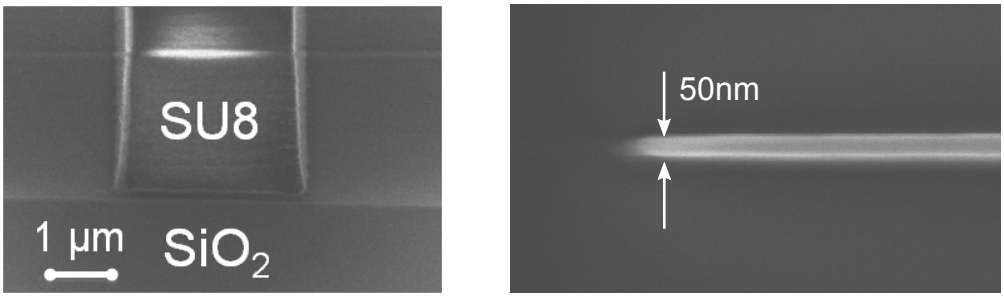

(a) (b)

Figure 65: (a) SEM cross-section of the 3 $\mu m \times 3 \mu m$ SU8 spot-size convertor waveguide. (b) SEM of the 50 nm wide Si nanotaper.

analyzer (OSA) based on the type of characterization (photo-detector for characterizing the transmission spectrum, and OSA for characterizing the output spectrum).

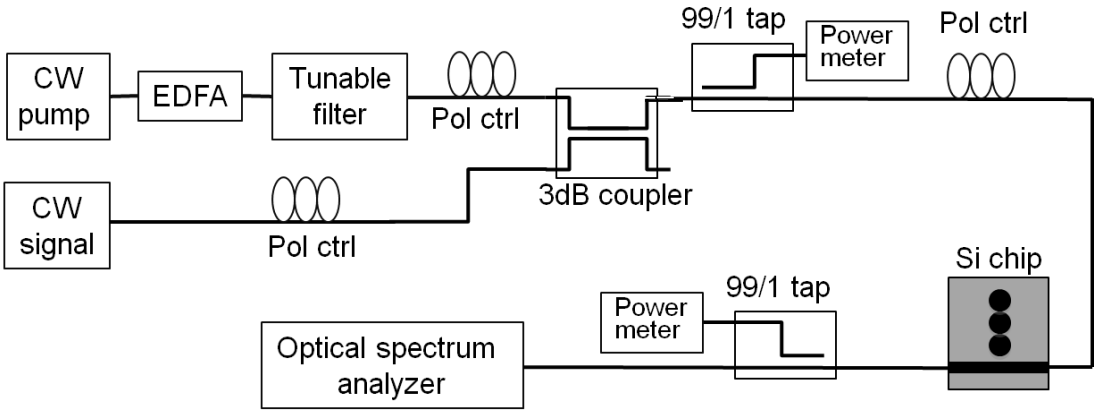

Figure 66: Experimental setup for FWM characterization of the coupled-resonator device.

Using the power-meters in the characterization setup the total insertion loss of the silicon chip is measured to be almost 10dB. First, the transmission spectrum of the fabricated devices are characterized and the results are shown in Figs. 67(a) and 67(b) for the coupled-microdisk device and in 68 for the coupled-racetrack resonator. The transmission spectrum in Fig. 67(a) shows a very large FSR around 52.5 nm for the coupled-microdisk. Figure 67(b) shows the three split modes of the coupled-microdisk device observed in each FSR in Fig. 67(a) near 1.548 μm. A mode splitting of around 0.8 nm is observed in this device. This transmission spectrum shows the possibility of achieving three split modes for a degenerate FWM experiment.

Figure 68 shows the transmission spectrum of the coupled-racetrack resonator shown in Fig. 64(a). A mode splitting in the order of 4 nm is observed in this device because of the strongly coupled racetracks using long coupling lengths (5.5 μm). It is observed that the modes of this device are critically-coupled, which considerably reduces FWM pump power requirement as a result of large field-enhancement. In the rest of this work, we use the coupled-racetrack device for FWM characterization as its large mode splitting enables us to considerably reject the ASE noise at the idler mode with the optical BPF in the setup. In our measurement setup, ASE noise should be small enough for us to be

able to measure the weak idler wave at the output. In future, we will integrate high-order coupled-resonator filters with high out-of-band rejection on the same Si chip as ASE filters for the characterization of the coupled-microdisk shown in Fig. 63(a).

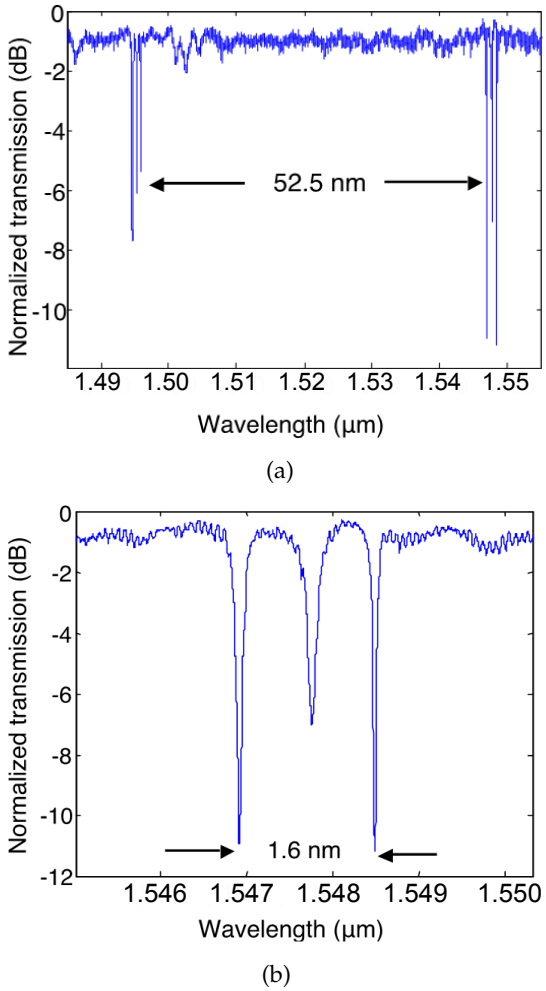

Figure 67: (a) Normalized transmission spectrum of the coupled-microdisk device shown in Fig. 63(a). (b) Normalized transmission spectrum of the same device as in (a) zoomed on the three split supermodes of the coupled-microdisk near 1.548 μm.

In order to use the coupled-racetrack device for FWM, the resonance frequency mismatch should be close to zero (See Eq. (77)). One of the purposes of the integrated micro-heaters is for the adjustment of this frequency mismatch. Because of material dispersion and the variations in the resonance frequency of the resonators in the coupled-resonator device, frequency mismatch might be far from zero. The coupled-racetrack resonator in Fig. 68 has a frequency mismatch of around 3 GHz which is much smaller than the

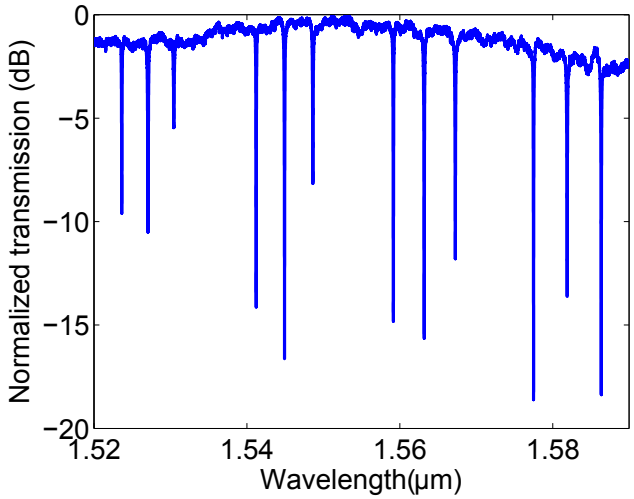

Figure 68: Normalized transmission spectrum of the coupled-racetrack device shown in Fig. 64(a).

FWHM of its modes ($\approx$ 20GHz corresponding to a Q_T=10,000). Thus, there is no need for fine tuning of the resonance frequency of individual resonators to satisfy FWM resonance condition. By tuning the pump and signal lasers to resonance modes at 1.545 μm and 1.541 μm and increasing the pump power in the bus waveguide to 2.5 mW, wavelength conversion is observed in the idler mode at 1.549 μm. The spectrum of the output of the device is shown in Fig. 69(b). The power of the idler at the output of the waveguide is 2.5 μW. By detuning the signal wavelength by 200 pm from the resonance mode it is observed that the converted idler disappears from the output spectrum (see Fig. 69(a)). This indicates that FWM observed takes place inside the resonator and not the waveguide.

By changing the pump power, the power at the converted idler is measured and plotted in Fig. 70(a) in red circles. Using the coupled-mode equations derived in Chap. 7, we calculated the expected converted idler power in the coupled-racetrack device with exact parameters as those in the tested device and the result is shown in Fig. 70(a) in blue curve. A relatively good agreement is observed between the experimental and simulation results. The maximum conversion efficiency for 2.5 mW pump power is measured to be -40dB. By increasing the pump power coupled into the device, we should be able to measure the idler power up to the saturation point forced by the nonlinear losses in the device.

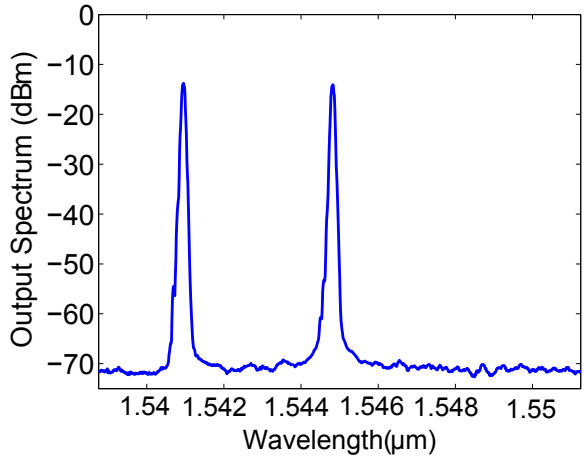

(a)

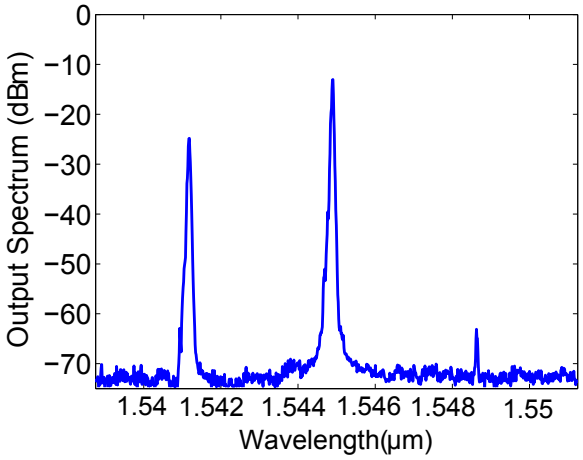

(b)

Figure 69: (a) Optical spectrum of the output of the device when the pump and signal lasers are tuned to resonance modes at 1.545 μm and 1.541 μm and for 2.5 mW of pump power. (b) Optical spectrum of the output of the device as in (a) when signal laser is 200 pm blue-shifted from the resonance mode. The parameters of the tested device are the same as those in the caption of Fig. 64(a).

We also study the effect of frequency mismatch on the idler power by heating the middle racetrack. Figure 70(b) shows the experimental result of the idler power versus the frequency mismatch in the coupled-racetrack resonator. It is observed that the output power is dropped by roughly 8 dB when the frequency mismatch is increased to 20 GHz. The high noise-floor in the experimental measurement setup did not allow us to measure the idler power beyond this amount of frequency mismatch.

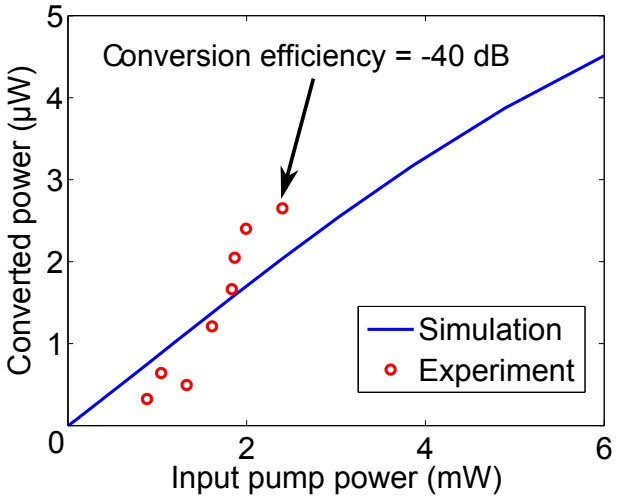

(a)

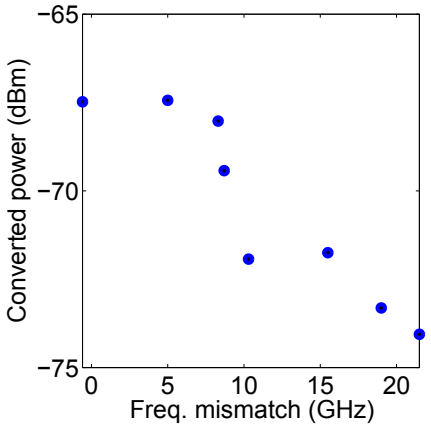

(b)

Figure 70: (a) Converted idler power at the output of the Si chip versus input pump power. Red circles and blue curve show the experimental and theoretical results, respectively. (b) Converted idler power versus frequency mismatch, which is tuned using the middle microheater. The parameters of the tested device are the same as those in the caption of Fig. 64(a).

We also tested the possibility of tuning of the mode-splitting in the proposed device

for the possibility of the tunability of wavelength conversion. The red curve in Fig. 62 shows the transmission spectrum of the coupled-racetrack device (shown in Fig. 67(a)) when 12 mW, 2 mW, and 4.5 mW power is dissipated in the top, middle, and bottom microheaters, respectively. It is observed that the mode splitting is increased from 3.7 nm in the original device (blue curve in Fig. 62) to 4.47 nm through this tuning. We also fine tuned microheater currents to adjust the frequency mismatch close to zero. Unfortunately, the top microheater burned out at this high power dissipation and we could not finish the nonlinear experiment for this device. In future, by increasing the thickness of the NiCr microheater we reduce the chance of electromigration and heater burnout. It should be noted that demonstrated tuning of the splitting (i.e., 0.8 nm) is equal to the spacing of two adjacent DWDM channels, which makes this device very practical for wavelength conversion application in DWDM systems.

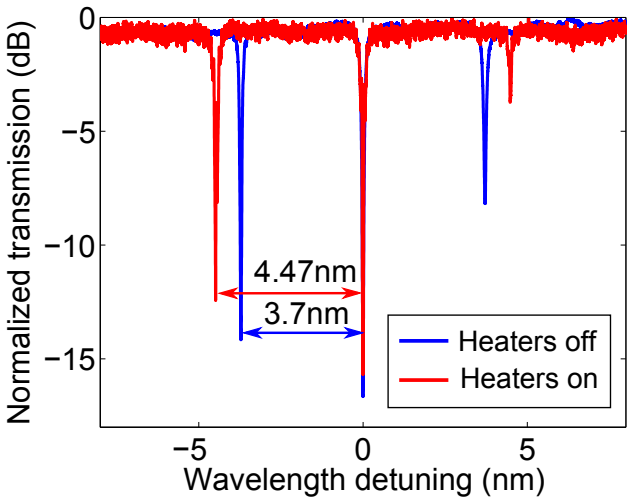

Figure 71: Normalized transmission spectrum of the coupled-racetrack device as-fabricated (blue curve) and for the case where the microheaters are used to tune the resonance mode splitting (red curve).

7.4 Discussion on Phase-Matching condition in the Coupled-Resonator Device

As explained thoroughly in Chap. 7, phase-matching condition is required for FWM. This condition changes to the zero frequency mismatch condition (in the absence of nonlinear contributions to phase matching condition) in a simple TWR (See Eq. (77)). Here, we

discuss how this zero frequency mismatch is modified in the coupled-resonator device proposed in this chapter. Here, we introduce a picture of the resonance effect in this device similar to that explained in Section 5.5. Figure 72(a) shows the schematic of the couple-resonator device where the two top resonators are considered as a phase-shifter ($\Phi(\omega)$) for the bottom resonator (R1). This picture is very similar to the quasi-phase-matching theory we introduced in Section 5.5. Therefore, we can assume any tuning of the phase-shifter ($\Phi(\omega)$) resonators is used to adjust the phase to satisfy the zero frequency-mismatch in the device. Figure 72(b) schematically shows the propagation of wave in R1 that undergoes a phase-shift of $\Phi(\omega)$ every round-trip. This the phase-shifter corrects for any dispersion or other effects that results in a non-zero frequency mismatch. This picture is analogous to the QPM used in wavegudies to satisfy the phase-matching condition. Using the same formulation as in Section 5.5 it is possible to show that nonlinear gain γ is reduced by $sinc(\frac{\beta_2(\Delta\omega)^2 L_R}{2})$ as a result of this QPM approach. Here, β_2 is the second-order GVD of the resonator, $\Delta\omega$ is the frequency difference of the pump and signal/idler waves, and L_R is the total length of the resonator.

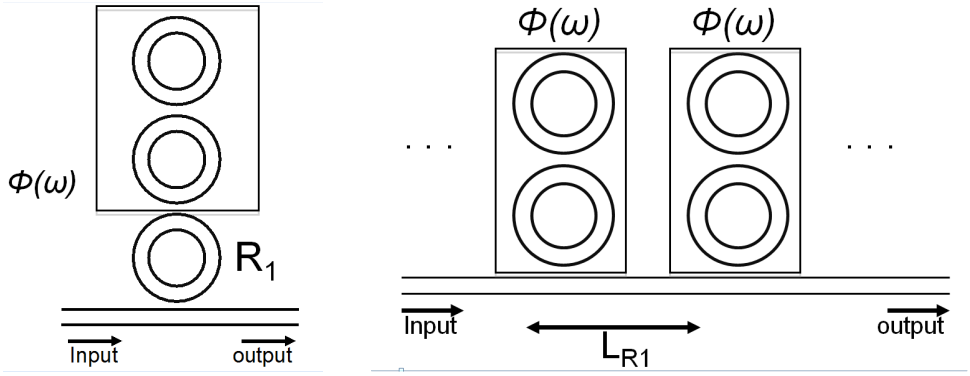

Figure 72: (a) Schematic of the couple-resonator device where the two top resonators are considered as a phase-shifter ($\Phi(\omega)$) for the bottom resonator (R1). (b) Schematically shows the propagation of wave in R1 that undergoes a phase-shift $\Phi(\omega)$ every round-trip. This picture is analogous to the QPM used in waveguides to satisfy the phase-matching condition.

7.5 Conclusion

In this chapter, we theoretically and experimentally demonstrated a three-element coupled-resonator device for FWM application. Using the three split supermodes of this device, we performed wavelength conversion. Unlike simple TWRs that do not allow the independent design of FSR and field-enhancement, this device allows us to benefit from the high field-enhancement of compact resonators independent of the wavelength of the interacting waves in the nonlinear process. By integrating microheaters on individual resonators we were able to fine-tune the frequency mismatch in this device to maximize wavelength conversion efficiency. We also showed that it is possible to tune the amount of splitting in this device by one DWDM channel spacing. This enables us to use a single resonator device for various wavelength conditions of the pump/signal/idler waves.

CHAPTER VIII

INTERFEROMETERICALLY COUPLED RESONATOR FOR FOUR-WAVE MIXING APPLICATION

8.1 Introduction

Optical microresonators are of great practical interest for on-chip nonlinear optics as they enhance the lightwave and lower the pump power requirement. The higher the finesse of the resonator, the higher the field enhancement. Finesse is linearly proportional to the Q of the resonator and inversely proportional to its mode-volume V_{eff}. There bas been a lot of efforts in improving the finesse or Q/V_{eff} of different types of resonators in the past [72, 72, 5]. Microtoroid resonators in silica with Qs in the order of 10^8 have been demonstrated [72]. Microdisks [5] and photonic crystal resonators [73] with Qs in the order of 10^6 have been experimentally demonstrated in Si. Microring and racetrack resonators which are the most widely used type of resonators for integrated optics applications have Qs in excess of 10^5. Figure 73 shows the relation between the bandwidth and intrinsic Q of resonator mode assuming that the resonator is critically coupled to an external bus waveguide [1]. The insets show the SEM of a few monolithic microresonators with the arrow pointing to the typical intrinsic Q of each resonator.

The typical 3 dB bandwidth of the resonant modes of the resonators shown in Fig. 73 is between 2 MHz to 2 GHz. However, the bandwidth of the signal in a typical optical communication system is more than 10 GHz and can go up to 100 GHz (shown on the horizontal axis of Fig. 73). The difference between the bandwidth imposed by critical-coupling condition (necessary to maximize field enhancement and reducing pump power requirement) and signal bandwidth results in a design tradeoff between bandwidth and field-enhancement. This is because resonators should be over-coupled to accommodate the

[1] The maximum field-enhancement is achieved when the resonator is critically coupled to the external bus waveguide. At this coupling regime, coupling and intrinsic Q of the resonator are equal ($Q_i = Q_c$). Therefore, the total Q of there resonator is $Q_T = Q_i/2$.

large signal bandwidth and this results in the loss of enhancement of pump wave, which is usually continuous-wave (CW) for on-chip applications. In this work, we propose and experimentally demonstrate a novel device that allows achieving the optimal bandwidth condition for the interacting waves in a FWM nonlinear process (i.e., pump, signal and idler). We show that this device will lift the bandwidth-enhancement trade-off that is present in conventional optical resonators [74], [75].

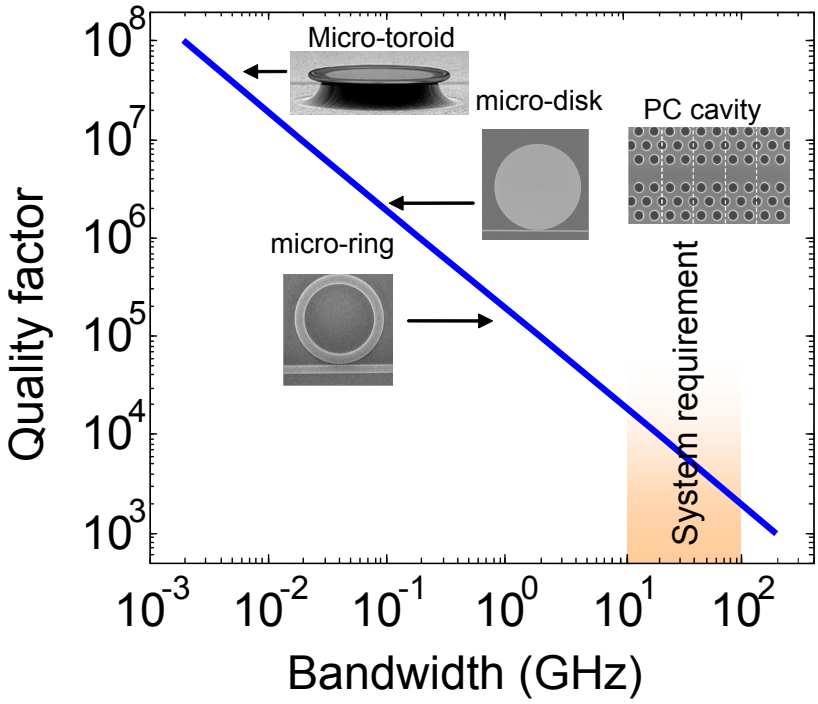

Figure 73: Relation between the intrinsic Q of resonator and the bandwidth of its modes considering critical coupling of the resonator. Insets show the SEM images of different monolithic resonators that are used for different sensing and signal processing applications. The arrows point at the typical intrinsic Q of the resonator.

8.2 Interferometrically Coupled Resonator: Proposal and Numerical Modeling

In Si, most of the nonlinear optics applications are through FWM as this process is wide-band and is relatively strong in Si. Assume we use a simple microring resonator as shown in Fig. 74(a) for wavelength conversion through FWM. Here, pump and signal waves couple to the resonator and the idler wave is generated with the information in signal transferred to idler. For a practical on-chip device a CW pump is used as it is less bulky and less expensive. Therefore, the bandwidth of the pump wave is at most in the order a few

to tens of MHz. However, signal and idler have a bandwidth in the order of a tens of GHz. This is schematically shown in Fig. 74(b). The bandwidth of a critically coupled microring resonator is in the order of 4 GHz (considering intrinsic Q of 10^5), which is sufficiently wide for the pump wave [2]. However, this bandwidth is not sufficient for signal/idler waves and in order to accommodate these waves, resonator bandwidth should be increased through over-coupling to the external bus waveguide. This over-coupling results in the loss of the enhancement of pump wave, which in turn increases the pump power requirement.

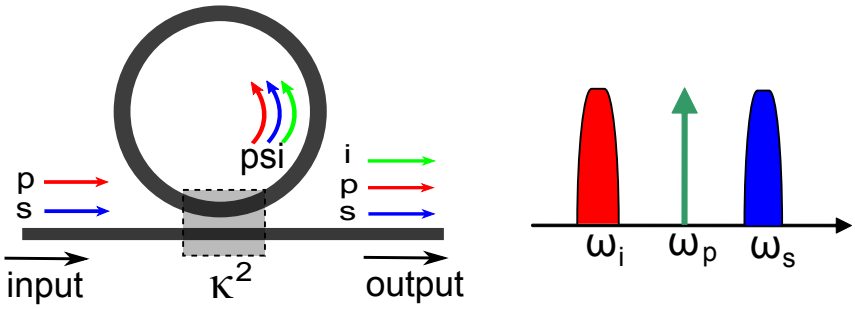

Figure 74: (a) shows the schematic of a microring resonator coupled to an external bus waveguide and is used for FWM-based wavelength conversion. (b) shows the diagram representing the bandwidths of the pump, signal, and idler. Here, pump is assumed to be CW and signal/idler have a much higher bandwidth in the order of a few tens of GHz.

In order to achieve different bandwidths at different FSRs of the resonator we propose to use an interferometric coupling (or two-point coupling) scheme as show in Fig. 75(a). The Mach-Zehnder (MZ) interferometer formed by L_{M1} and L_{M2} modulates the coupling strength in wavelength and therefore, provides the means of achieving frequency-dependent coupling. It can be easily shown that the effective coupling of this coupling scheme is given by

$$\kappa_{eff}^2 = 4\kappa^2 cos^2[\frac{(\beta L_M)_2 - (\beta L_M)_1}{2}] \tag{88}$$

where κ^2 is the power coupling coefficient at each single coupling point between the resonator and bus waveguide, and $(\beta L_M)_i$ is the propagation phase at the interferometer

[2] In fact, it is desirable to have a lower bandwidth (or higher Q) to have higher field enhancement. For example for the microtoroid shown in Fig. 73 the bandwidth is 4 MHz.

arm i. Figure 75(b) shows the transmission spectrum of a 20 μm diameter microring resonator with the intrinsic Q of 60×10^3 coupled to a bus waveguide using the interferometric scheme (power coupling coefficient at each single point is $\kappa^2 = 0.094$). It is seen that the extinction ratio at the output varies for different FSRs. The top curve in Fig. 75(b) shows κ^2_{eff} for this structure. It is clearly seen that the effective external coupling to the resonator is modulated in wavelength. In these simulations we assumed a microring and waveguide effective and group indices of 2.35 and 4.25, respectively. The MZ length difference is $L_{M2} - L_{M1} = 0.375\pi d$ where d is the diameter of the resonator.

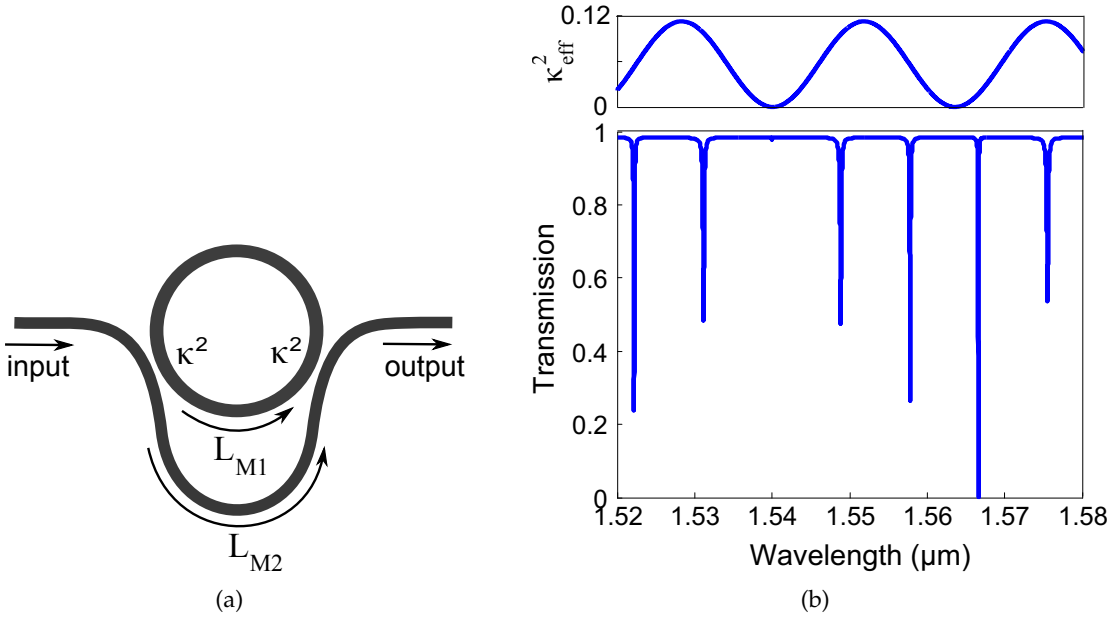

Figure 75: (a) shows the structure of the interferometric coupling scheme for a microring resonator. The interferometer is formed between L_{M1} and L_{M2} arms. (b) Transmission spectrum of the device shown in (a). Here, microring diameter is d =20 μm with the intrinsic Q of 60×10^3, $L_{M2} - L_{M1} = 0.375\pi d$, and $\kappa^2 = 0.094$. The top figure shows the effective coupling power to the resonator, κ^2_{eff}.

In a FWM application, the bandwidths of the signal and idler are usually equal. Thus, we design the interferometric coupling region such that the coupling strength is equal at every other FSR of the resonator. This requires that $L_{M2} - L_{M1} = L_{res}/2$, which for $L_{M1} = L_{res}/2$ results in $L_{M1} = 3L_{res}/2$. Blue curve in Fig. 76(a) shows the transmission spectrum of such interferometrically coupled resonator with a diameter of 20 μm, intrinsic Q of 2×10^5, designed for signal/idler bandwidth of 20 GHz. Here, the coupling coefficient

at each single coupling points is determined to satisfy critical coupling condition at for the pump wave. Figure 76(b) shows the effective coupling coefficient to this device. We have also simulated the transmission spectrum of the single-point coupled resonator that is designed to accommodate signal/idler bandwidth of 20 GHz. It is seen that the critical coupling condition of the pump wave is no longer met. Figures 76(c) and 76(d) show the zoomed version of the transmission spectra of these two devices at the pump and signal/idler wavelengths, respectively.

In order to compare the performance of the simple coupling scheme to the interferometric scheme, field intensity is simulated in these devices and the results are depicted in Fig. 77(a). Here, the intensity of the circulating field in the resonator is normalized to the intensity of the incoming wave. Figures 77(b) and 77(c) show normalized field intensity at the pump and signal/idler wavelengths. It is observed that the intensity of pump wave is almost three times higher in the interferometrically coupled resonator, compared to that of the single-point coupled resonator.

In the wavelength conversion process considered here, idler photon is generated through the interaction of two pump and one signal photons. Equation (66) represents the temporal evolution of this idler wave in a resonator. The last term on the RHS of this equation is the contribution from the FWM gain. This term is proportional to $A_p^2 A_s$, where $|A_p|^2$ and $|A_s|^2$ are the energies of the pump and signal waves in the resonator, which are proportional to the field-enhancement factor in the resonator (see Eq. 27). Idler power coupled at the output waveguide is also proportional to $|A_i|^2$. Therefore, idler gain is proportional to the product of the field-enhancement factor of the pump, signal, and idler waves through

$$\eta_{WC} \propto |IE_p|^2.|IE_s|.|IE_i| \tag{89}$$

where $|IE_\nu|$ is the field intensity enhancement in the resonator ($\nu = p,s$). Using this simple relation for wavelength conversion efficiency, we find that the η_{WC} is 8 times higher in the interferometric coupled resonator compared to the simple coupling structure.

The proposed structure allows us to lift the tradeoff between bandwidth and field-enhancement that is faced in conventional devices. In other words, we are no longer

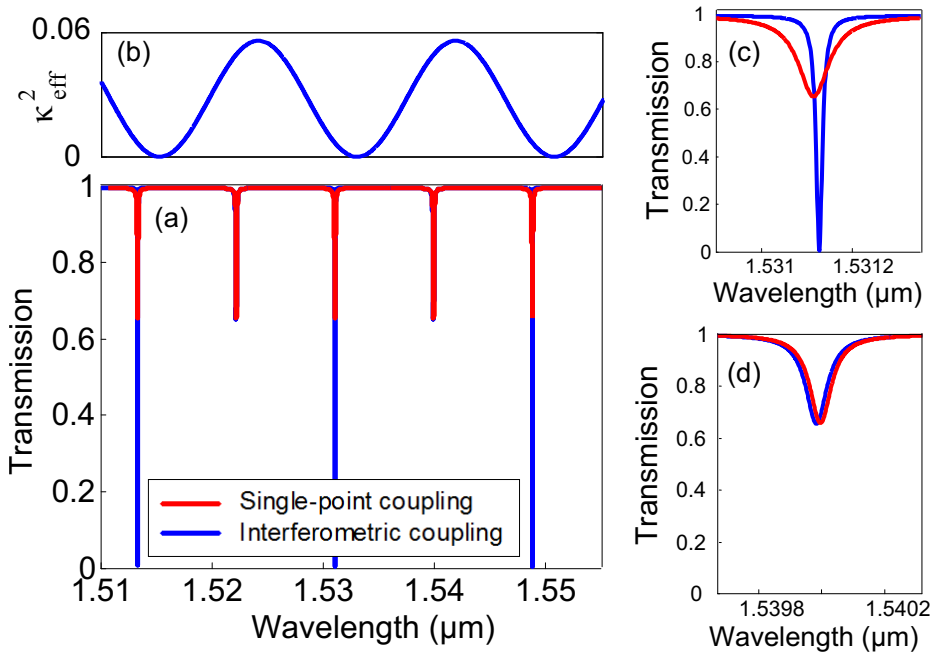

Figure 76: (a) Transmission spectrum of the interferometrically coupled resonator (blue curve) and a simple single-point coupled resonator (red curve) used for a FWM application. The diameter of the resonator is 20 μm with an intrinsic Q of 2×10^5 and the design is for signal/idler bandwidth of 20 GHz. (b) shows the effective coupling coefficient to the resonator. (c) and (d) show the transmission spectrum of the resonator as shown in (a) at one pump and one signal/idler wavelengths, respectively.

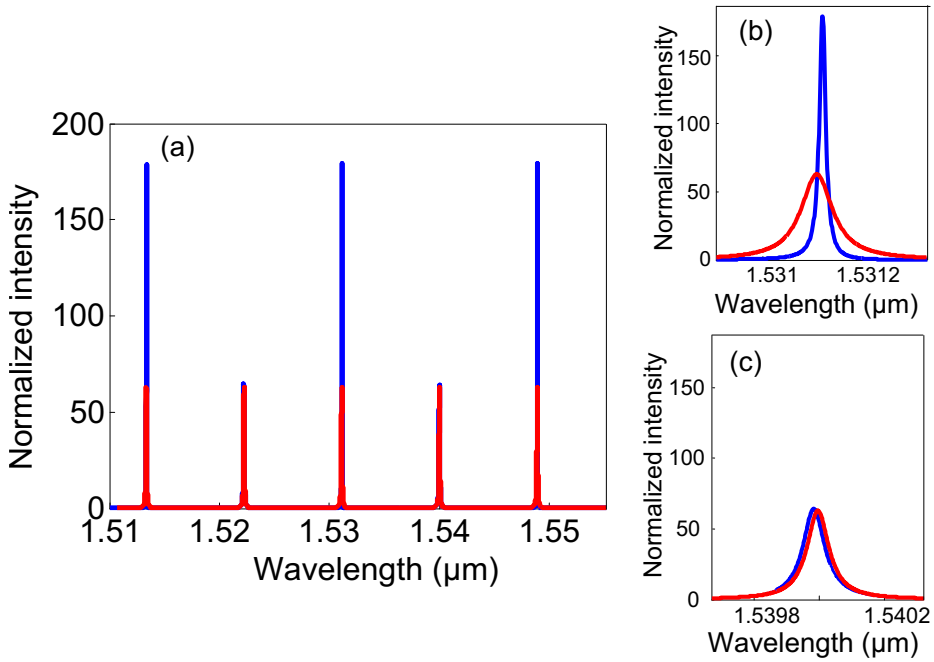

Figure 77: (a) Normalized field intensity in the interferometrically coupled resonator (blue curve) and a simple single-point coupled resonator (red curve) used for a FWM application. Device parameters are the same as those in Fig. 76. (b) and (c) show the the normalized field intensity in the resonator as shown in (a) at one pump and one signal/idler wavelengths, respectively.

doomed to work along the Q-bandwidth line shown in Fig. 73. We simulated the improvement in wavelength conversion efficiency achieved through the optimal design of the interferometric coupling scheme compared to the single point coupling scheme based on Eq. (89). The relative wavelength conversion efficiency in the interferometrically coupled resonator (η_{ICR}) to that of the single-point coupled resonator (η_0) is plotted in Fig. 78 in dB (i.e., $10log(\frac{\eta_{ICR}}{\eta_0})$). It is seen that 3 to 4 orders of magnitude enhancement can be achieved using the proposed coupling scheme in high-Q resonators with $Q > 10^6$.

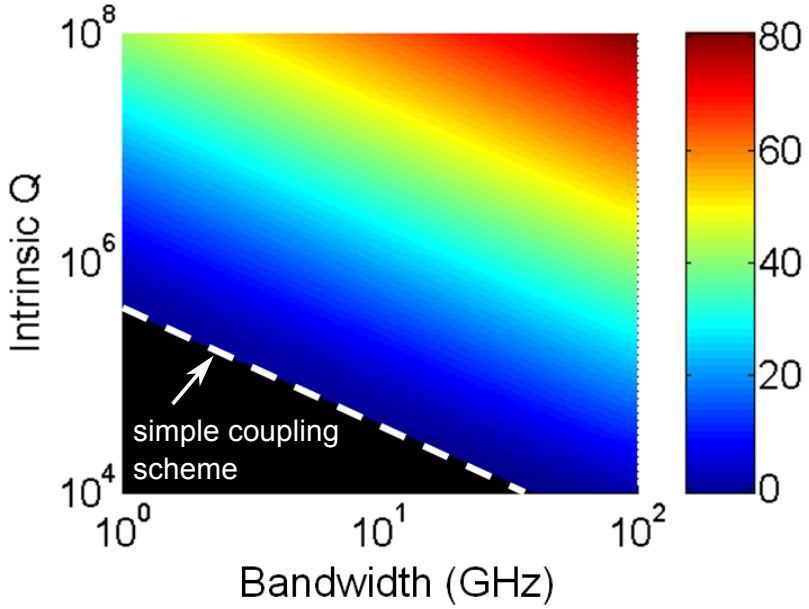

Figure 78: The relative wavelength conversion efficiency of the interferometrically coupled resonator, $10log(\frac{\eta_{ICR}}{\eta_0})$, for different intrinsic Qs and different signal bandwidth. η_0 is the wavelength conversion efficiency of a single-point coupled resonator.

8.3 Experimental Results

We fabricated he device proposed in the previous section on an SOI wafer with a Si thickness of 220 nm and a buried oxide (BOX) layer thickness of 1 μm and we measured its linear transmission response. Here, we used a 40 μm diameter microring resonator with a width of 480 nm. The input waveguide also has a width of 480 nm. The outer arm of the interferometer has a length of $L_{M1} = 3L_{res}/2 = 3\pi d/2$, where $d = 40\ \mu m$ is the diameter of the resonator. This waveguide width results in a slightly multimode operation of the waveguide, which did not pose any problem in our experiments. The details of the

fabrication is found in Section 3.2. The pattern is written on ZEP electron-beam resist using electron-beam lithography and etched in Si by inductive-coupled-plasma (ICP) using a combination of Cl_2 and HBr gases. Figure 79(a) shows the SEM of the fabricated device. After this step, 1 μm SiO_2 is deposited using PECVD and micro-heater patterns are defined by a lift-off process. Microheaters are composed of 50nm thick Ni and contact pads are covered with 50nm Au for better electrical contact. The overall resistance of the heater and its pads is 190 Ω. Figure 79(b) shows the optical micrograph of the final device with integrated microheaters.

The reason for integrating microheaters is to assure that the critical coupling condition is well satisfied for the pump wavelength. The critical coupling condition in our device is satisfied through the destructive interference of the two arms of the interferometer. This interference is highly sensitive to the dispersion of the interferometer arms. At the same time, because of the high sensitivity of Si waveguide dispersion to variations of waveguide width, slight change in the waveguide width (caused by the finite accuracy of the fabrication process) results in a large shift in the waveguide dispersion. The capability of fine tuning the phase of the lower arm of the interferometer allows us to tune the coupling for critical coupling operation.

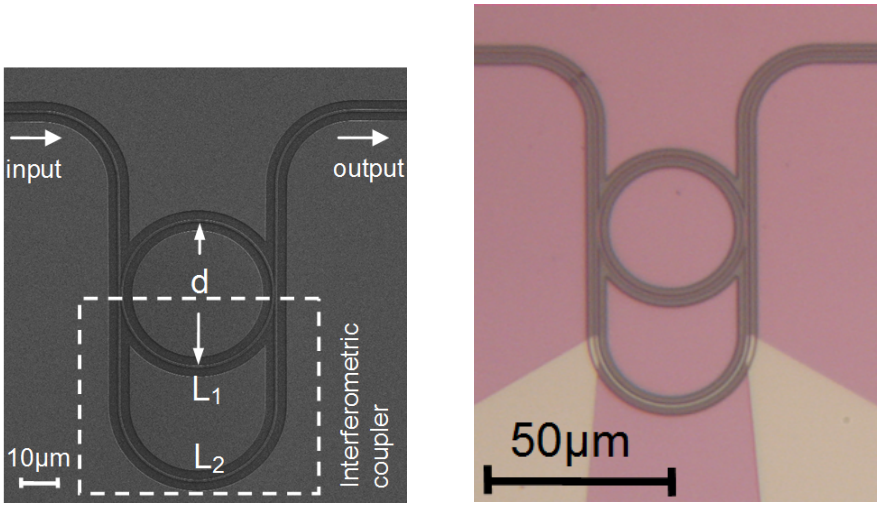

(a) (b)

Figure 79: (a) SEM image of the interferometrically coupled resonator on an SOI platform with a diameter of 40 μm designed for a FWM application. (b) Optical micrograph of the device in (a) after the integration of metallic microheaters on the lower interferometer arm.

We then measured the transmission spectrum of this device by coupling light into and out of the device using tapered fibers. By using a polarization-controller, TE polarized light is coupled to the device. Figure 80(a) shows the transmission spectrum of this device when there is no signal applied to the microheater. The modulation of the extinction at the resonance modes of the device is observed. It is observed that because of the waveguide dispersion mismatch between the arms of the interferometer, the extinction at the high-Q modes varies in different FSRs. By applying a DC electric signal to the microheater we can change the extinction to achieve critical coupling (i.e., zero output power). Figures 80(b) and 80(c) show the transmission spectrum of the same resonator for different heating powers in the microheater for the high-Q and low-Q modes, respectively. It is observed that by dissipating 1.2 mW power in the microheater, the output transmission drop at high-Q mode is further reduced by 6dB (measurement is limited to the noise level of the experimental setup). It is also observed in Fig. 80(c) that while tuning to the critical coupling, the low-Q mode is not significantly changed.

8.4 Conclusion

In this chapter, we proposed a new coupling scheme in microresonators that enables the optimum coupling strength for different modes that interact in the resonator through a nonlinear process. This coupling scheme that is proposed for the first time for a nonlinear application, lifts the bandwidth-enhancement tradeoff that is encountered in the simple coupling scheme. We particularly considered and designed this device for FWM application in Si. We theoretically showed that by using this device, up to 4 to 5 orders of magnitude enhancement in the wavelength conversion efficiency in high-Q resonators with $Q > 10^6$ can be achieved compared to a simple coupling method [3]. We have also experimentally demonstrated the proposed device on an SOI platform. The transmission spectrum of the device shows the modulation of the coupling to the resonator. By incorporating a microheater on one arm of the interferometric coupler, we were able to fine tune

[3]Here, we ignored the effects of two-photon absorption, free-carrier absorption, nonlinear contribution to phase-matching condition, on the efficiency of wavelength conversion

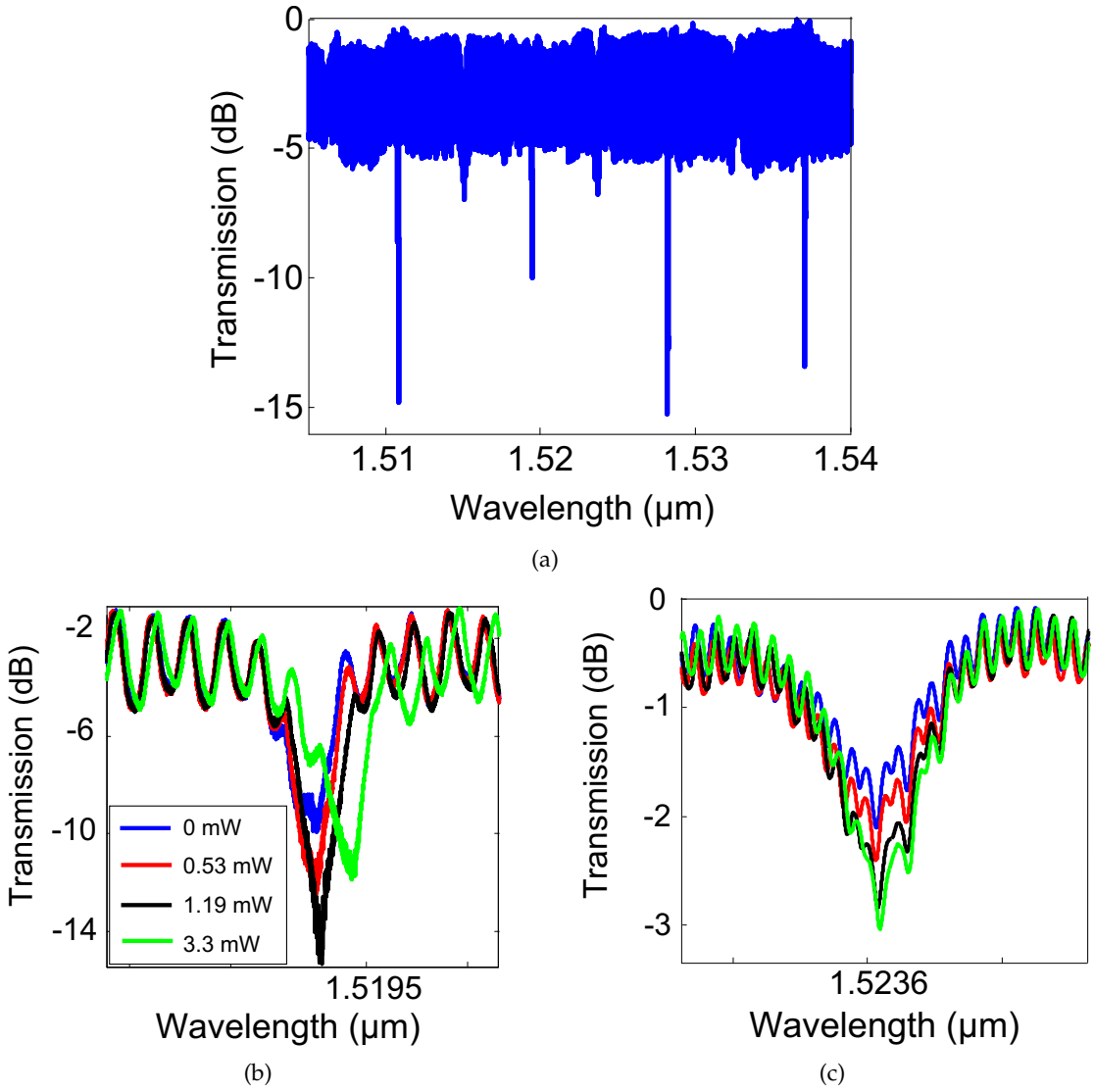

Figure 80: (a) Transmission spectrum of the device shown in 79(b) for the TE polarization, when there is no signal applied to the microheater. (b) and (c) show the transmission spectrum of the device in 79(b) for the high-Q and low-Q modes, respectively; for different heating powers in the microheater.

the coupling to achieve critical coupling at the pump wavelength. This device can be used for wavelength conversion in WDM fiber optic networks.

CHAPTER IX

CONCLUSION

9.1 Summary of Achievements

Silicon photonics for different optical signal processing applications is one of the fastest growing fields in the realm of optics and electrical engineering. The main motivation behind this race is the bandwidth and speed limitations of electronics. In this Ph.D. thesis, two of the technological and design challenges in this field are addressed: 1) A new microheater architecture is proposed and experimentally demonstrated with one order of magnitude faster reconfiguration time without the loss of other performance metrics. 2) A series of novel tunable resonator-based devices are proposed and experimentally demonstrated for nonlinear optics applications that lift many of the design trade-offs of the conventional traveling-wave resonators (TWRs).

Device reconfiguration through local heating is one of the more widely used methods in silicon photonics because of the strong thermooptic effect in this material. Before this work, several microheater architectures had been proposed and optimized to improved one of the device performance metrics such as, power consumption or speed. In this work, we proposed a new microheater architecture and reconfiguration scheme to considerably improve the device performance both in terms speed and power consumption simultaneously. The design tradeoff originates from the fact that on a simple SOI platform, lower thermal resistance for high-speed operation results in higher power consumption. In this work, we theoretically studied the physics of heat diffusion in this platform in detail. Although the thermal time constant is subject to slow heat diffusion through the BOX layer, very small heat propagation delays are obtainable by placing the heaters on Si or any other high thermal conductive material. Here, we directly integrated the microheater on the Si layer and achieved sub-100-ns heat-propagation delay. Using a pre-emphasis circuit, we were able to reconfigure the photonics device sub-100-ns. This method allows

us to improve the reconfiguration time by one order of magnitude without sacrificing the power consumption.

In order to further lower the power consumption, we used a resonator-based reconfiguration design. Almost every reconfiguration needed for the targeted optical signal processing functionalities are achievable using resonator-based phase-shifters and switches. In this work, we leveraged the ultrasmall microdisk resonators developed in the Photonics Research Group at Georgia Tech to implement tunable microresonators. The ultrasmall mode-volume of these devices considerably reduces the power consumption for phase-shift and switching applications. We achieved 2.4 nm/mW resonance wavelength shift in a 4 μm diameter microdisk that enables phase-shifters with power consumption in the order of the best devices optimized for low-power operation to this date using complicated fabrication processes in Si. This low-power operation allows us to integrate hundreds of these tunable elements on a the same chip with power budget in the order of one watt.

The other major focus of this Ph.D. work was the design of novel reconfigurable photonic devices for nonlinear optics applications in Si. Here, we targeted the practical challenges of the small bandwidth of resonance modes when moving from waveguide-based to resonator-based devices. The high field-enhancement inside optical resonators considerably reduces the pump power requirement, which is very important for chip-scale applications. Usually in a simple TWR, which has been widely used in Si photonics recently, there are two practical challenges: 1) fixed free-spectral range (FSR) and 2) Uniform bandwidth of the resonance modes. In this work, we addressed these two challenges through novel device ideas.

The fixed FSR (or basically the frequency spacing between resonance modes) of TWRs requires precise design and implementation of the FSR for a nonlinear process. Otherwise, some of the interacting waves might fall out of the resonance of the device. Moreover, a resonator with a fixed FSR can only be used when the frequencies of the interacting waves are known for the design of the device. This considerably limits the deployment of TWRs for a wide range of nonlinear optics applications. In this work, we proposed a new device concept based on coupled resonators, in which we exploit the supermodes of the

coupled structure to engineer resonance modes. By tuning either the resonance frequency of individual resonances or the mutual coupling of the resonators, we were able to control the splitting of supermodes and consequently the spacing between the modes.

In this work, we proposed two different coupled resonator devices with the capability of post-fabrication tuning of the frequency spacing of their modes. The first device demonstrated is a two-element coupled resonator, in which the coupling between the resonators in achieved through a Mach-Zehnder interferometer (MZI). By tuning this MZI, mutual resonator coupling and therefore, the frequency spacing of the resonance modes is tuned. We were able to achieve 0.4 nm tuning of the resonance wavelength spacing, equivalent to 20% of the FSR. This is the first demonstration of the tuning of resonance spacing in an integrated platform. We have also shown that through this tuning mechanism it is possible to fine tune the resonance frequencies to maximize the four-wave mixing (FWM) in this structure. One of the unique applications of this device is in Raman sensing, where the Raman spectrum of different analytes is different and a single resonator cannot be used to accommodate all analytes. This device enables keeping the pump wavelength fixed while scanning another resonance mode to capture the Raman scattering from the analyte.

Another resonator device consisting of three coupled resonators was proposed and experimentally demonstrated specifically for FWM application. By coupling three resonators, three separate supermodes are creating that enable degenerate FWM in a very compact structure. Through this device, we were able to control the frequency spacing of the resonances only through the mutual coupling strength of the resonators and not their length. This new device concept allows us to use ultrasmall resonators (with FSR ¿ 50 nm) for a wide range of pump/signal/idler conditions. We experimentally demonstrated wavelength conversion through FWM in this device. Moreover, we were able to tune the frequency difference of the pump mode with that of the signal/idler mode for future implementation of tunable wavelength conversion in a resonator.

In this Ph.D. work, we also demonstrated an interferometric coupling scheme for optimum design of the bandwidth of individual resonance modes for a nonlinear optical process in a resonator. In order to fully exploit the field-enhancement capability of a

resonator, the bandwidths of the resonance modes associated with each wave (i.e., pump, signal, and idler) should match with the actual bandwidth of the corresponding wave. A simple coupling scheme (i.e., coupling bus waveguide to the resonator at one point) is not capable of addressing this design issue. The proposed device enhances the efficiency of the nonlinear process by orders of magnitude when using high-Q resonators.

To fully understand the physics of the nonlinear process in the proposed resonator devices, we implemented a nonlinear temporal coupled-mode theory in TWRs. Using this coupled-mode theory, we analyzed the performance of FWM in Si microresonators. We also developed a quasi-phase-matching theory in TWRs and applied it to the proposed devices in this work. This theoretical analysis shows the possibility of achieving optical parametric oscillation in Si for the first time through the three-element coupled-resonator device proposed in this work.

9.2 Future Directions

Here is a list of future directions that are valuable along the continuation of this Ph.D. work:

9.2.1 Ultra-fast Thermal Reconfiguration

In chapter 4, we demonstrated sub-100-nanosecond reconfiguration of novel microheaters fabricated directly on small microdisks. There are several other projects to further study and improve the performance of these devices. Here is a list of possible projects in this area:

1: Improving the reconfiguration time by removing the thermal contact resistance between metallic microheaters and the microdisk through resistive heating of the Si layer.

2: Experimental analysis of the thermal cross-talk of the microheater-on-microdisk architecture for large-scale integration.

3: Implementing the ultrafast microdisk-based phase-shifters in high-order tunable filter architecture (See Figs. 81(a), 81(b), and 81(c)).

9.2.2 Nonlinear Optics in Si

In this work, novel resonator-based devices are demonstrated for FWM applications in Si. However, only wavelength conversion was demonstrated in the three-element coupled-resonator device. There are numerous nonlinear processes that can be implemented in the proposed devices and other devices based on the device concepts developed in this Ph.D. work. Here is a list of possible projects along this direction:

1: Demonstration of FWM in the two-point coupled-resonator shown in Chap. 6. This device enables very selective nonlinear interaction between the desired modes, which enables cross-talk-free wavelength conversion in fiber optics networks.

2: Tuning of the resonance-spacing of the proposed coupled-resonator by one whole FSR and applying it to a Raman sensing application.

3: Applying the device ideas proposed in this work to the mid-infrared wavelength range ($\lambda > 2.2\mu m$) where the two-photon absorption of Si vanishes. This will potentially enable interesting nonlinear processes on Si including optical parametric oscillation.

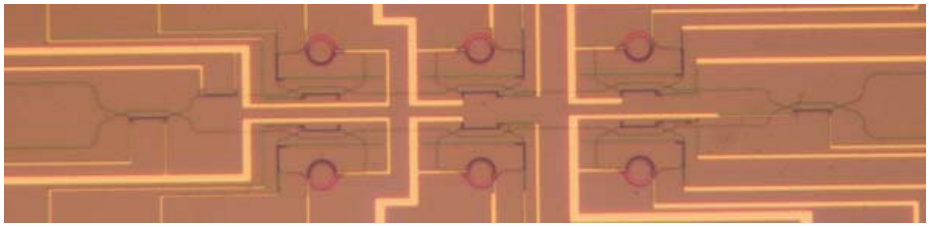

(a)

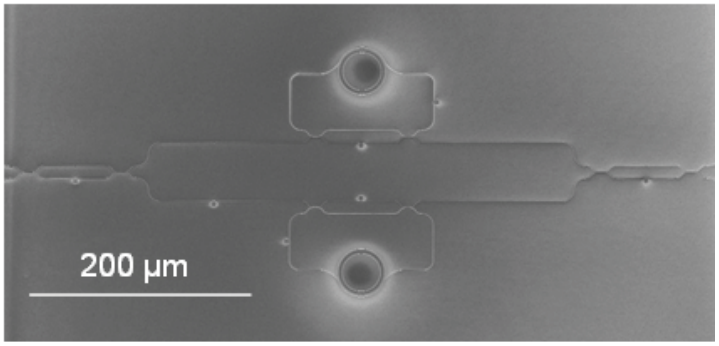

(b)

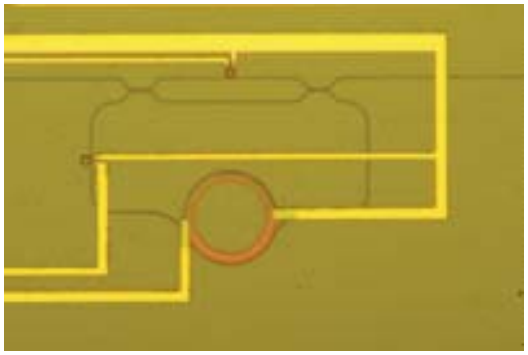

(c)

Figure 81: (a) Optical micrograph of a sixth order baseline filter. (b) SEM of a second-order tunable filter fabricated with small microdisk phase-shifters (c) Optical micrograph of one tunable all-pass phase-shifter with microheaters fabricated on microdisks.

APPENDIX A

RESONANCE CONDITION OF COUPLED-RESONATOR DEVICES

A.1 Introduction

Here, we derive the resonance condition of the device shown in Fig. 48(a) using the transfer-matrix method [71]. If we assume that the vectors $\bar{a} = [a_2\ a_1]^T$ and $\bar{b} = [b_2\ b_1]^T$ in Fig. 48(a) represent the wave amplitudes entering and exiting the DC, respectively; we have

$$\bar{b} = \mathbf{T}\bar{a} = \begin{bmatrix} t_c & j\kappa_c \\ j\kappa_c^* & t_c^* \end{bmatrix} \tag{90}$$

where $\mathbf{T}$ is the transfer matrix of a general DC coupling the two resonators in which θ_c is the propagation phase, and t_c and κ_c are the amplitude through and cross-coupling coefficients, respectively. Also, through the feedback path from $\bar{b}$ to $\bar{a}$ we have

$$\bar{a} = \exp(-j\beta L)\bar{b}, \tag{91}$$

where L is the length of each resonator and β is the propagation constant of resonators. By combining Eqs. 90 and 91 we have

$$|\mathbf{T} - \exp(j\beta L)\mathbf{I}| = 0, \tag{92}$$

and by substituting for $\mathbf{T}$ from Eq. 90 in Eq. 92, the following eigenvalue equation for the resonance frequency of the coupled-resonator device is derived:

$$\exp(j2\phi) + 2\Re\{t_c\}\exp(j\phi) + 1 = 0, \tag{93}$$

Here, $\phi = \theta_c + \beta L$ and $\Re$ represents the real part of the argument in the parentheses. It should be noted that since very strong coupling between resonators is considered, first-order coupled-mode-theory could not be used here [49].

Figures 48(b) and 48(c) show the two coupled-resonator structures of our interest in which coupling is achieved using one and two symmetric DCs, respectively. The power through and coupling coefficients of all DCs in both structures are denoted by t^2 and κ^2, respectively. For the coupler in the single-point-coupled resonator (Fig. 48(b)), we have

$$\begin{cases} t_c = t \\ \kappa_c = \kappa \\ \theta_c = 0 \end{cases} \tag{94}$$

and for the MZI coupler in the two-point-coupled resonator (Fig. 48(c)), we have,

$$\begin{cases} t_c = t^2 \exp(-j\Delta\phi_{MZ}/2) - \kappa^2 \exp(j\Delta\phi_{MZ}/2) \\ \kappa_c = 2\kappa t \cos(\Delta\phi_{MZ}/2) \\ \theta_c = \phi_{MZ}^{ave} \end{cases} \tag{95}$$

where, $\Delta\phi_{MZ} = \phi_{MZ}^1 - \phi_{MZ}^2$ and $\phi_{MZ}^{ave} = (\phi_{MZ}^1 + \phi_{MZ}^2)/2$; where, ϕ_{MZ}^1 and ϕ_{MZ}^2 are the propagation phase terms in Arm1 and Arm2 of the Mach-Zehnder, respectively. By substituting Eqs. 94 and 95 into Eq. 92 and by solving the eigenvalue equation, resonance frequencies of the coupled-resonator structures and consequently, their resonance splitting are calculated and shown in Fig. 48(d).

APPENDIX B

MATERIAL DISPERSION

For the calculation of GVD in Chapter 5, we use the following dispersion properties of Si from Ref. [63]:

$$\begin{aligned} n_{Si}^2 = 1 &+ 10.66842933\lambda^2/[\lambda^2 - (0.3015116485)^2] \\ &+ 0.003043475\lambda^2/[\lambda^2 - (1.13475115)^2] \\ &+ 1.54133408\lambda^2/[\lambda^2 - (1104.0)^2] \end{aligned} \tag{96}$$

APPENDIX C

PUBLICATIONS

Journal publications:

[1] **A. H. Atabaki**, A. A. Eftekhar, E. Shah Hosseini, S. Yegnanarayanan and A. Adibi, "Ultra-Compact, Low-Power and Fast Thermal Reconfiguration for Large-Scale Silicon Photonics, submitted to Nature Photonics.

[2] **A. H. Atabaki**, A. A. Eftekhar, E. Shah Hosseini, S. Yegnanarayanan and A. Adibi, " Optimization of Metallic Microheater for High-speed Reconfigurable Silicon Photonics" submitted for publication.

[3] **A. H. Atabaki**, B. Momeni, A. A. Eftekhar, E. Shah Hosseini, S. Yegnanarayanan and A. Adibi, "Tuning of resonance-spacing in a traveling-wave resonator device," Opt. Express 18(9), 2010.

[4] E. Shah Hosseini, S. Yegnanarayanan, **A. Atabaki** , M. Soltani, and A. Adibi, "Systematic design and fabrication of high-Q pulley-coupled planar silicon nitride microdisk resonators," Opt. Express 18(3), 2010.

[5] B. Momeni, M. Askari, E. Hosseini, **A. Atabaki**, and A. Adibi, "An on-chip silicon grating spectrometer using a photonic crystal reflector," Journal of Optics, 12(3), March 2010.

[6] Q. Li, M. Soltani, **A. Atabaki**, S. Yegnanarayanan, and A. Adibi, "Quantitative modeling of coupling-induced resonance frequency shift in microring resonators," Opt. Express 17(26), 2009.

[7] E. Shah Hosseini, S. Yegnanarayanan, **A. Atabaki**, M. Soltani, and A. Adibi, "High quality planar silicon nitride microdisk resonators for integrated photonics in the visible wavelength range," Opt. Express 17(17), 2009.

[8] **A. Atabaki**, E. Shah Hosseini, B. Momeni, and A. Adibi, "Enhancing the guiding bandwidth of photonic crystal waveguides on silicon-on-insulator," Opt. Lett. 33(22), 2008.

Conference Proceedings and Presentations:

[1] **A. H. Atabaki**, and A. Adibi, Ultra-Compact Coupled-Resonator Device for Four-Wave Mixing Applications, presented in Conference on Lasers and Electro-Optics (CLEO) 2011.

[2] **A. H. Atabaki**, A. A. Eftekhar, S. Yegnanarayanan, A. Adibi, Sub-100ns and low-loss reconfigurable silicon photonics, 23rd Annual Meeting of the IEEE Photonics Society, 2010.

[3] P. Alipour, A. A. Eftekhar, **A. H. Atabaki**, Q. Li, S. Yegnanarayanan, A. Adibi, Fully Reconfigurable Compact RF Photonic Filters Using High-Q Silicon Microdisk Resonators, 23rd Annual Meeting of the IEEE Photonics Society, 2010.

[4] P. Alipour, A. A. Eftekhar, **A. H. Atabaki**, Q. Li, S. Yegnanarayanan, C. K. Madsen, and A. Adibi, Fully

Reconfigurable Compact RF Photonic Filters Using High-Q Silicon Microdisk Resonators, in Optical Fiber Communication Conference, OSA Technical Digest (CD) (Optical Society of America, 2011), paper OThM5.

[5] **A. H. Atabaki**, Q. Li, S. Yegnanarayanan, and A. Adibi, "Demonstration of Frequency-Detuning Compensation in a Traveling-Wave Resonator for Efficient Four-Wave-Mixing," in Conference on Lasers and Electro-Optics/International Quantum Electronics Conference, OSA Technical Digest (CD) (Optical Society of America, 2010), paper CThR3.

[6] **A. H. Atabaki**, A. A. Eftekhar, S. Yegnanarayanan, and A. Adibi, "Novel Micro-Heater Structure for Low-Power and Fast Photonic Reconfiguration," in Conference on Lasers and Electro-Optics/International Quantum Electronics Conference, OSA Technical Digest (CD) (Optical Society of America, 2010), paper JThE44.

[7] P. Alipour, **A. H. Atabaki**, A. A. Eftekhar, and Ali Adibi, "Titania-Clad Microresonators on SOI With Athermal Performance," in Conference on Lasers and Electro-Optics/International Quantum Electronics Conference, OSA Technical Digest (CD) (Optical Society of America, 2010), paper CWP6.

[8] **A.H. Atabaki**, A.A. Eftekhar, S. Yegnanarayanan, and A. Adibi, "Sub-microsecond thermal reconfiguration of silicon photonic devices," 22nd Annual Meeting of the IEEE Lasers and Electro-Optics Society (LEOS), 2009.

[9] M. Soltani, S. Yegnanarayanan, Q. Li, **A. Atabaki**, A.A. Eftekhar, and A. Adibi, "Sustained GHz oscillations in ultra-high Q silicon microresonators," 22nd Annual Meeting of the IEEE Lasers and Electro-Optics Society (LEOS), 2009.

[10] **A. H. Atabaki**, A. A. Eftekhar, S. Yegnanarayanan, and A. Adibi, "Enhancing Thermal Reconfiguration Speed for Silicon Photonics Applications," in Integrated Photonics and Nanophotonics Research and Applications, OSA Technical Digest (CD) (Optical Society of America, 2009), paper IMC3.

[11] **A. H. Atabaki**, M. Soltani, S. Yegnanarayanan, A. A. Eftekhar, and A. Adibi, "Optimization of Metallic Micro-Heaters for Reconfigurable Silicon Photonics," in Conference on Lasers and Electro-Optics/International Quantum Electronics Conference, OSA Technical Digest (CD) (Optical Society of America, 2009), paper CThB4.

[12] **A. H. Atabaki**, S. Yegnanarayanan, and A. Adibi, "Resonance Spacing Tuning in Traveling-Wave Resonators," in Conference on Lasers and Electro-Optics/International Quantum Electronics Conference, OSA Technical Digest (CD) (Optical Society of America, 2009), paper CTuE3.

[13] **A.H. Atabaki**, Q. Li1, S. Yegnanarayanan, M. Chamanzar, E. Shah-Hosseini, A.A Eftekhar, M. Soltani, B. Momeni, and A. Adibi, "Interferometrically-coupled traveling-wave resonators for nonlinear optics applications," IEEE/LEOS Winter Topicals Meeting Series, 89, 2009.

[14] B. Momeni, E. Shah Hosseini, **A. Atabaki**, Q. Li, M. Soltani, and A. Adibi, "On-chip spectrometers for visible and infrared sensing applications," Photonics West 2009, San Jose, CA, 2009.

[15] **A.H. Atabaki**, S. Yegnanarayanan, B. Momeni, E. Shah-Hosseini, Q. Li, M. Soltani, A.A. Eftekhar, and A. Adibi, "Implementation of a coupling-tunable resonator for efficient high-bandwidth nonlinear silicon photonics applications," 21st Annual Meeting of the IEEE Lasers and Electro-Optics Society (LEOS), 2008.

[16] **A. H. Atabaki**, M. Soltani, Q. Li, S. Yegnanarayanan, and A. Adibi, "Modeling of Thermal Properties of Silicon-on-Insulator Traveling-Wave Resonators," in Frontiers in Optics, OSA Technical Digest (CD) (Optical

Society of America, 2008), paper FThK4.

[17] Q. Li, S. Yegnanarayanan, **A. Atabaki**, and A. Adibi, "Calculation and Correction of Coupling-Induced Resonance Frequency Shifts in Traveling-Wave Dielectric Resonators," in Integrated Photonics and Nanophotonics Research and Applications, (Optical Society of America, 2008), paper IWH3.

[18] **A.H. Atabaki**, E.S. Hosseini, B. Momeni, and A. Adibi, "Engineering of planar photonic crystal waveguides on silicon-on-insulator for larger guiding bandwidth," Photonics West 2008, San Jose, CA, 2008.

REFERENCES

[1] J. Foresi, B. Little, G. Steinmeyer, E. Thoen, S. Chu, H. Haus, E. Ippen, L. Kimerling, and W. Greene, "Si/SiO2 microring resonator optical add/drop filters," in "Proc. Conf. Lasers Electro-Optics, Baltimore, MD, postdeadline paper CPD22, May 1997," .

[2] M. Kuwata-Gonokami, R. Jordan, A. Dodabalapur, H. Katz, M. Schilling, R. Slusher, and S. Ozawa, "Polymer microdisk and microring lasers," semiconductors **2**, 3.

[3] B. Little, S. Chu, P. Absil, J. Hryniewicz, F. Johnson, F. Seiferth, D. Gill, V. Van, O. King, M. Trakalo *et al.*, "Very high-order microring resonator filters for WDM applications," IEEE Photonics Technology Letters **16**, 2263–2265 (2004).

[4] Y. Vlasov, M. O'Boyle, H. Hamann, and S. McNab, "Active control of slow light on a chip with photonic crystal waveguides," Nature **438**, 65–69 (2005).

[5] M. Soltani, S. Yegnanarayanan, and A. Adibi, "Ultra-high Q planar silicon microdisk resonators for chip-scale silicon photonics." Opt. Express **15**, 4694 (2007).

[6] M. Masanovic, V. Lal, J. Summers, J. Barton, E. Skogen, L. Rau, L. Coldren, and D. Blumenthal, "Widely tunable monolithically integrated all-optical wavelength converters in InP," Journal of Lightwave Technology **23**, 1350 (2005).

[7] M. Soltani, Q. Li, S. Yegnanarayanan, and A. Adibi, "Ultimate miniaturization of single and coupled resonator filters in silicon photonics," in "Conference on Lasers and Electro-Optics/International Quantum Electronics Conference," (Optical Society of America, 2009), p. CTuE7.

[8] T. Barwicz and H. Haus, "Three-dimensional analysis of scattering losses due to sidewall roughness in microphotonic waveguides," Lightwave Technology, Journal of **23**, 2719–2732 (2005).

[9] K. Lee, D. Lim, L. Kimerling, J. Shin, and F. Cerrina, "Fabrication of ultralow-loss Si/SiO_2 waveguides by roughness reduction," Optics Letters **26**, 1888–1890 (2001).

[10] J. Cardenas, C. Poitras, J. Robinson, K. Preston, L. Chen, and M. Lipson, "Low loss etchless silicon photonic waveguides," Opt. Express **17**, 4752–4757 (2009).

[11] M. Borselli, T. Johnson, and O. Painter, "Beyond the Rayleigh scattering limit in high-Q silicon microdisks: theory and experiment," Opt. Express **13**, 1515–1530 (2005).

[12] Q. Li, M. Soltani, S. Yegnanarayanan, and A. Adibi, "Design and demonstration of compact, wide bandwidth coupled-resonator filters on a siliconon-insulator platform," Opt. Express **17**, 2247–2254 (2009).

[13] Q. Xu, B. Schmidt, S. Pradhan, and M. Lipson, "Micrometre-scale silicon electro-optic modulator," Nature **435**, 325–327 (2005).

[14] W. Green, M. Rooks, L. Sekaric, and Y. Vlasov, "Ultra-compact, low RF power, 10 Gb/s silicon Mach-Zehnder modulator," WMJ **2945**, 2955 (2006).

[15] B. Lee, A. Biberman, N. Sherwood-Droz, C. Poitras, M. Lipson, and K. Bergman, "High-Speed 2 2 Switch for Multiwavelength Silicon-Photonic Networks–On-Chip," Journal of Lightwave Technology **27**, 14 (2009).

[16] L. Colace, G. Masini, G. Assanto, H. Luan, K. Wada, and L. Kimerling, "Efficient high-speed near-infrared Ge photodetectors integrated on Si substrates," Applied Physics Letters **76**, 1231 (2000).

[17] D. Ahn, C. Hong, J. Liu, W. Giziewicz, M. Beals, L. Kimerling, J. Michel, J. Chen, and F. K
"artner, "High performance, waveguide integrated Ge photodetectors," Appl. Phys. Lett **87**, 103501 (2005).

[18] M. Geng, L. Jia, L. Zhang, L. Yang, P. Chen, T. Wang, and Y. Liu, "Four-channel reconfigurable optical add-drop multiplexer based on photonic wire waveguide," OPTICS EXPRESS **17**, 5502–5516 (2009).

[19] E. Klein, D. Geuzebroek, H. Kelderman, G. Sengo, N. Baker, and A. Driessen, "Reconfigurable optical add-drop multiplexer using microring resonators," IEEE PHOTONICS TECHNOLOGY LETTERS **17**, 2358–2360 (2005).

[20] *http://www.luxtera.com/* (10 December 2010).

[21] *http://www.kotura.com/* (10 December 2010).

[22] Y. Han and B. Jalali, "Photonic time-stretched analog-to-digital converter: Fundamental concepts and practical considerations," Journal of Lightwave Technology **21**, 3085 (2003).

[23] K. Jackson, S. Newton, B. Moslehi, M. Tur, C. Cutler, J. Goodman, and H. Shaw, "Optical fiber delay-line signal processing," IEEE Transactions on Microwave Theory and Techniques **33**, 193–210 (1985).

[24] S. Yoo and R. Bellcore, "Wavelength conversion technologies for WDM network applications," Lightwave Technology, Journal of **14**, 955–966 (1996).

[25] J. Hansryd and P. Andrekson, "Broad-band continuous-wave-pumped fiber optical parametric amplifier with 49-dB gain and wavelength-conversion efficiency," IEEE Photonics Technology Letters **13**, 194–196 (2001).

[26] P. Absil, J. Hryniewicz, B. Little, P. Cho, R. Wilson, L. Joneckis, and P. Ho, "Wavelength conversion in GaAs micro-ring resonators," Optics Letters **25**, 554–556 (2000).

[27] M. Foster, A. Turner, R. Salem, M. Lipson, and A. Gaeta, "Broad-band continuous-wave parametric wavelength conversion in silicon nanowaveguides," Opt. Express **15**, 12949–12958 (2007).

[28] Q. Xu, V. Almeida, and M. Lipson, "Micrometer-scale all-optical wavelength converter on silicon," Optics letters **30**, 2733–2735 (2005).

[29] T. Durhuus, B. Mikkelsen, C. Joergensen, S. Lykke Danielsen, and K. Stubkjaer, "All-optical wavelength conversion by semiconductor optical amplifiers," IEEE/OSA Journal of Lightwave Technology **14**, 942–954 (1996).

[30] M. Chou, I. Brener, M. Fejer, E. Chaban, and S. Christman, "'1.5-m-band wavelength conversion based on cascaded second-order nonlinearity in LiNbO3 waveguides," IEEE Photon. Technol. Lett **11**, 653–655 (1999).

[31] Y. Chen, C. Chang, Y. Yang, I. Kuo *et al.*, "Mach-Zehnder fiber-grating-based fixed and reconfigurable multichannel optical add-drop multiplexers for DWDM networks," Optics Communications **169**, 245–262 (1999).

[32] M. Earnshaw, M. Cappuzzo, E. Chen, L. Gomez, A. Griffin, E. Laskowski, A. Wong-Foy, and J. Soole, "Planar lightwave circuit based reconfigurable optical add-drop multiplexer architectures and reusable subsystem module," IEEE Journal of Selected Topics in Quantum Electronics **11**, 313–322 (2005).

[33] X. Wang, J. A. Martinez, M. S. Nawrocka, and R. R. Panepucci, "Compact thermally tunable silicon wavelength switch: Modeling and characterization," IEEE PHOTONICS TECHNOLOGY LETTERS **20**, 936–938 (2008).

[34] H.-Y. Ng, M. R. Wang, D. Li, X. Wang, J. Martinez, R. R. Panepucci, and K. Pathak, "1x4 wavelength reconfigurable photonic switch using thermally tuned microring resonators fabricated on silicon substrate," IEEE PHOTONICS TECHNOLOGY LETTERS **19**, 704–706 (2007).

[35] I. Kiyat, A. Aydinli, and N. Dagli, "Low-power thermooptical tuning of SOI resonator switch," IEEE PHOTONICS TECHNOLOGY LETTERS **18**, 364–366 (2006).

[36] T. Chu, H. Yamada, S. Ishida, and Y. Arakawa, "Compact 1 x N thermo-optic switches based on silicon photonic wire waveguides," OPTICS EXPRESS **13**, 10109–10114 (2005).

[37] D. Geuzebroek, E. Klein, H. Kelderman, N. Baker, and A. Driessen, "Compact wavelength-selective switch for gigabit filtering in access networks," IEEE PHOTONICS TECHNOLOGY LETTERS **17**, 336–338 (2005).

[38] T. Goh, M. Yasu, K. Hattori, A. Himeno, M. Okuno, and Y. Ohmori, "Low loss and high extinction ratio strictly nonblocking 16 x 16 thermooptic matrix switch on 6-in wafer using silica-based planar lightwave circuit technology," JOURNAL OF LIGHTWAVE TECHNOLOGY **19**, 371–379 (2001).

[39] R. Jones, J. Doylend, P. Ebrahimi, S. Ayotte, O. Raday, and O. Cohen, "Silicon photonic tunable optical dispersion compensator," OPTICS EXPRESS **15**, 15836–15841 (2007).

[40] F. Horst, R. Germann, U. Bapst, D. Wiesmann, B. Offrein, and G. Bona, "Compact tunable FIR dispersion compensator in SiON technology," IEEE PHOTONICS TECHNOLOGY LETTERS **15**, 1570–1572 (2003).

[41] H. Lira, S. Manipatruni, and M. Lipson, "Broadband hitless silicon electro-optic switch for on-chip optical networks," Opt. Express **17**, 22271–22280 (2009).

[42] C. Li, L. Zhou, and A. Poon, "Silicon microring carrier-injection-based modulators/switches with tunable extinction ratios and OR-logic switching by using waveguide cross-coupling," Optics Express **15**, 5069–5076 (2007).

[43] J. Takayesu, M. Hochberg, T. Baehr-Jones, E. Chan, G. Wang, P. Sullivan, Y. Liao, J. Davies, L. Dalton, A. Scherer *et al.*, "A Hybrid Electrooptic Microring Resonator-Based 1×4 *times*1 ROADM for Wafer Scale Optical Interconnects," J. Lightwave Technol **27**, 440–448 (2009).

[44] M. S. Rasras, D. M. Gill, S. S. Patel, K.-Y. Tu, Y.-K. Chen, A. E. White, A. T. S. Pomerene, D. N. Carothers, M. J. Grove, D. K. Sparacin, J. Michel, M. A. Beals, and L. C. Kimerling, "Demonstration of a fourth-order pole-zero optical filter integrated using CMOS processes," JOURNAL OF LIGHTWAVE TECHNOLOGY **25**, 87–92 (2007).

[45] R. Soref and B. Bennett, "Electrooptical effects in silicon," IEEE Journal of Quantum Electronics **23**, 123–129 (1987).

[46] R. Soref, "The past, present, and future of silicon photonics," IEEE J. Sel. Top. Quantum Electron **12**, 1678–1687 (2006).

[47] D. Marcuse, *Theory of dielectric optical waveguides* (1974).

[48] E. Hosseini, S. Yegnanarayanan, A. Atabaki, M. Soltani, and A. Adibi, "Systematic design and fabrication of high-Q single-mode pulley-coupled planar silicon nitride microdisk resonators at visible wavelengths," Opt. Express **18**, 2127–2136 (2010).

[49] H. Haus, *Waves and fields in optoelectronics* (Prentice-Hall, 1984).

[50] U. Fischer, T. Zinke, B. Schuppert, and K. Petermann, "Singlemode optical switches based on SOI waveguides with largecross-section," Electronics Letters **30**, 406–408 (1994).

[51] F. Kreith and M. Bohn, *Principles of heat transfer* (Harper & Row New York, 1986).

[52] D. Cahill, W. Ford, K. Goodson, G. Mahan, A. Majumdar, H. Maris, R. Merlin, and S. Phillpot, "Nanoscale thermal transport," Journal of Applied Physics **93**, 793 (2003).

[53] R. Amatya, C. W. Holzwarth, H. I. Smith, and R. J. Ram, "Precision Tunable Silicon Compatible Microring Filters," IEEE PHOTONICS TECHNOLOGY LETTERS **20**, 1739–1741 (2008).

[54] M. Harjanne, M. Kapulainen, T. Aalto, and P. Heimala, "Sub-mu s switching time in silicon-on-insulator Mach-Zehnder thermooptic switch," IEEE PHOTONICS TECHNOLOGY LETTERS **16**, 2039–2041 (2004).

[55] M. Geis, S. Spector, R. Williamson, and T. Lyszczarz, "Submicrosecond submilliwatt silicon-on-insulator thermooptic switch," IEEE PHOTONICS TECHNOLOGY LETTERS **16**, 2514–2516 (2004).

[56] O. Boyraz and B. Jalali, "Demonstration of a silicon raman laser," Optics Express **12**, 5269–5273 (2004).

[57] H. Rong, R. Jones, A. Liu, O. Cohen, D. Hak, A. Fang, and M. Paniccia, "A continuous-wave raman silicon laser," Nature **433**, 725–728 (2005).

[58] A. Turner, M. Foster, A. Gaeta, and M. Lipson, "Ultra-low power parametric frequency conversion in a silicon microring resonator," Opt. Express **16**, 4881–4887 (2008).

[59] R. Salem, M. Foster, A. Turner, D. Geraghty, M. Lipson, and A. Gaeta, "Signal regeneration using low-power four-wave mixing on silicon chip," Nature Photonics **2**, 35–38 (2007).

[60] Q. Lin, O. Painter, and G. Agrawal, "Nonlinear optical phenomena in silicon waveguides: modeling and applications," Optics Express **15**, 16604–16644 (2007).

[61] M. Dinu, F. Quochi, and H. Garcia, "Third-order nonlinearities in silicon at telecom wavelengths," Applied physics letters **82**, 2954–2956 (2003).

[62] G. Agrawal, *Nonlinear Fiber Optics* (Academic, San Diego, California, 1995).

[63] M. Weber, *Handbook of optical materials* (CRC, 2003).

[64] T. Johnson, M. Borselli, and O. Painter, "Self-induced optical modulation of the transmission through a high-Q silicon microdisk resonator," Optics Express **14**, 817–831 (2006).

[65] R. Salem, M. Foster, A. Turner, D. Geraghty, M. Lipson, and A. Gaeta, "Signal regeneration using low-power four-wave mixing on silicon chip," Nature Photonics **2**, 35–38 (2007).

[66] A. Turner-Foster, M. Foster, J. Levy, C. Poitras, R. Salem, A. Gaeta, and M. Lipson, "Ultrashort free-carrier lifetime in low-loss silicon nanowaveguides," Optics Express **18**, 3582–3591 (2010).

[67] J. Armstrong, N. Bloembergen, J. Ducuing, and P. Pershan, "Interactions between light waves in a nonlinear dielectric," Physical Review **127**, 1918 (1962).

[68] P. Franken and J. Ward, "Optical harmonics and nonlinear phenomena," Reviews of Modern Physics **35**, 23 (1963).

[69] Y.-G. Han, X. Dong, J. H. Lee, and S. B. Lee, "Wavelength-spacing-tunable multichannel filter incorporating a sampled chirped fiber Bragg grating based on a symmetrical chirp-tuning technique without center wavelength shift," OPTICS LETTERS **31**, 3571–3573 (2006).

[70] J. Magne, P. Giaccari, S. Larochelle, J. Azana, and L. Chen, "All-fiber comb filter with tunable free spectral range," OPTICS LETTERS **30**, 2062–2064 (2005).

[71] J. Poon, J. Scheuer, S. Mookherjea, G. Paloczi, Y. Huang, and A. Yariv, "Matrix analysis of microring coupled-resonator optical waveguides," OPTICS EXPRESS **12**, 90–103 (2004).

[72] D. Armani, T. Kippenberg, S. Spillane, and K. Vahala, "Ultra-high-Q toroid microcavity on a chip," Nature **421**, 925–928 (2003).

[73] Y. Akahane, T. Asano, B. Song, and S. Noda, "High-Q photonic nanocavity in a two-dimensional photonic crystal," Nature **425**, 944–947 (2003).

[74] A. Atabaki, S. Yegnanarayanan, B. Momeni, E. Shah-Hosseini, Q. Li, M. Soltani, A. Eftekhar, and A. Adibi, "Implementation of a coupling-tunable resonator for efficient high-bandwidth nonlinear silicon photonics applications," in "IEEE Lasers and Electro-Optics Society, 2008. LEOS 2008. 21st Annual Meeting of the," (IEEE), pp. 312–313.

[75] A. Atabaki, Q. Li, S. Yegnanarayanan, M. Chamanzar, E. Shah-Hosseini, A. Eftekhar, M. Soltani, B. Momeni, and A. Adibi, "Interferometrically-coupled traveling-wave resonators for nonlinear optics applications," in "IEEE/LEOS Winter Topicals Meeting Series, 2009," (IEEE), pp. 89–90.